https://lib.uliege.be https://matheo.uliege.be

Mémoire

Auteur : Vanhorebeek, Stef
Promoteur(s) : Fettweis, Xavier; 28016
Faculté : Faculté des Sciences
Diplôme : Master en océanographie, à finalité approfondie
Année académique : 2024-2025
URI/URL : http://hdl.handle.net/2268.2/22952

Avertissement à l'attention des usagers :

Tous les documents placés en accès ouvert sur le site le site MatheO sont protégés par le droit d'auteur. Conformément aux principes énoncés par la "Budapest Open Access Initiative"(BOAI, 2002), l'utilisateur du site peut lire, télécharger, copier, transmettre, imprimer, chercher ou faire un lien vers le texte intégral de ces documents, les disséquer pour les indexer, s'en servir de données pour un logiciel, ou s'en servir à toute autre fin légale (ou prévue par la réglementation relative au droit d'auteur). Toute utilisation du document à des fins commerciales est strictement interdite.

Par ailleurs, l'utilisateur s'engage à respecter les droits moraux de l'auteur, principalement le droit à l'intégrité de l'oeuvre et le droit de paternité et ce dans toute utilisation que l'utilisateur entreprend. Ainsi, à titre d'exemple, lorsqu'il reproduira un document par extrait ou dans son intégralité, l'utilisateur citera de manière complète les sources telles que mentionnées ci-dessus. Toute utilisation non explicitement autorisée ci-avant (telle que par exemple, la modification du document ou son résumé) nécessite l'autorisation préalable et expresse des auteurs ou de leurs ayants droit.

Climate change modelling in the Barents Sea-Novaya Zemlya region in winter and sensitivity to rapid sea ice loss (1981-2023)

Author: Stef Vanhorebeek

Academic year: 2024-2025

Supervisor: Prof. Dr. Xavier FETTWEIS

Co-supervisor: Associate Prof. Dr. Bayoumy MOHAMED

A master's thesis submitted in partial fulfillment of the requirements for the Master's degree in Oceanography

LIÈGE université

Summary

Within the Arctic, the Barents Sea and the Russian archipelago Novaya Zemlya have experienced significant sea ice decline and glacier loss, especially during winter, with a climate shift around 2000–2001. However, it remains unclear how the local climate has changed in this region since 1981 and how this is related to oceanic changes. This study therefore investigates the sensitivity of atmospheric conditions to variations in sea ice concentration and sea surface temperature. The local climate is reconstructed using the regional climate model MAR. The experiment is designed to assess the climate based on the actual evolution of sea ice decline and sea surface temperature rise, and how it would look using pre-shift climatological values for these variables. The model results, validated with station observations, show that MAR reproduces climate conditions well and indicate that sea ice near the northern Barents Sea coast of Novaya Zemlya has probably declined due to atmospheric changes, such as warmer air temperatures and stronger winds pushing ice offshore. In the southeastern Barents Sea, Atlantification likely played a more important role by reinforcing sea ice melt. For future research, coupling MAR to an ocean model is recommended to better capture ocean–atmosphere interactions.

Résumé

Dans l'Arctique, la mer de Barents et l'archipel russe de Novaya Zemlya ont connu un recul important de la glace de mer et une perte de glaciers, en particulier en hiver, avec un changement climatique autour de 2000-2001. Cependant, il reste difficile de déterminer comment le climat local a évolué dans cette région depuis 1981 et comment cette évolution est liée aux changements océaniques. Cette étude porte donc sur la sensibilité des conditions atmosphériques aux variations de la concentration de glace de mer et de la température de surface de la mer. Le climat local est reconstruit à l'aide du modèle climatique régional MAR. Le plan expérimental compare le climat actuel, marqué par le déclin de la glace et la hausse des températures de surface de mer, à une simulation basée sur les valeurs climatologiques préalables au changement. Les résultats, validés par des observations, montrent que MAR reproduit bien le climat et suggèrent que la diminution de la glace près de la côte nord de Novaya Zemlya résulte surtout de changements atmosphériques, comme des températures d'air plus chaudes et des vents renforcés poussant la glace au large. Dans le sud-est de la mer de Barents, l'Atlantification a probablement renforcé la fonte de la glace de mer. Pour de futures recherches, il est recommandé de coupler MAR à un modèle océanique afin de mieux représenter les interactions océan-atmosphère.

Acknowledgements

I could not have undertaken this journey without the support of my supervisors, Professor Xavier Fettweis and Associate Professor Bayoumy Mohamed and their research group. Their guidance in shaping the research question, feedback, and answers to my questions throughout the process greatly contributed to my understanding of the topic, methodology, and results.

I also thank Professor Marilaure Grégoire for connecting me with Professor Fettweis so that I had the opportunity to work on a subject I was very interested in. This led to the opportunity to assist Dr. Polina Verezemskaya with her work on the Black Sea, which deepened my understanding of model validation. I am very grateful to Polina for sharing her expertise in Python and model validation, which proved extremely valuable.

I sincerely thank my parents, my siblings, my partner's parents and, of course, my partner, Louis, for their support and belief in me throughout the pursuit of a second master's degree.

Finally, I would like to thank the entire oceanography team, both professors and fellow students, for making this master's program a truly enriching experience. Time to splice the mainbrace!

Contents

List of Figures

List of Tables

List of abbreviations

α_3	Skewness
α_4	Kurtosis
AI	Artificial intelligence
CERES	Clouds and the Earth's Radiant Energy System
CFRS	Climate Forecast System Reanalysis
DJF	December, January, February
ECMWF	European Centre for Medium-Range Weather Forecasts
ERA5	Fifth generation ECMWF atmospheric reanalysis
ESM	Earth system model
GCM	Global climate model
JJA	June, July, August
LHF	Latent heat flux
LWD	Longwave downward radiation
LWU	Longwave upward radiation
MAE	Mean absolute error
MAR	Modèle Atmosphérique Régional
NASA	National Aeronautics and Space Administration
NCEP	National Centers for Environmental Prediction
NESTOR	NESTing ORganization for the preparation of meteorological and surface fields
NOAA	National Oceanic and Atmospheric Administration
NSD	Normalized standard deviation
P1	Period 1: 1981-2001

P2	Period 2: 2002-2023
RCM	Regional climate model
RCP	Representative Concentration Pathway(s)
RMSD	Root mean square deviation
$Q_{\mathbf{net}}$	Net surface heat flux
SHF	Sensible heat flux
SIC	Sea ice concentration
SIE	Sea ice extent
SISVAT	Soil Ice Snow Vegetation Atmosphere Transfer scheme
SIT	Sea ice thickness
SLP	Sea level pressure
SMB	Surface mass balance
SST	Sea surface temperature
SWD	Shortwave downward radiation
SWU	Shortwave upward radiation
T2M	2-meter air temperature
U10	10-meter zonal wind speed
V10	10-meter meridional wind speed
WDSP	Wind speed
WE	Water equivalent

1 Introduction

Human-induced climate change is intensifying globally, although its effects are uneven (Lee et al., 2023). A region that is particularly vulnerable to global warming is the Arctic, which comprises the region at the highest latitudes north of 66.5°N (Serreze & Barry, 2014), centered around the north pole, as shown in Figure 1. Depending on the observational studies conducted, the Arctic has been found to warm nearly two to four times faster than the global average warming between 1979 and 2021, a phenomenon known as Arctic amplification (Comiso et al., 2008; Rantanen et al., 2022; Serreze & Barry, 2011). The Arctic is widely recognized as a key region in global climate change. It comprises most of the northern hemisphere's sea ice extent (SIE), reaching up to 15 million km^2 in late winter (Serreze & Barry, 2014). SIE is defined as the total area where the sea ice concentration (SIC) exceeds the threshold for the sea ice edge, which is typically set at 15 percent (National Snow and Ice Data Center, 2024). Compared to Antarctica, Arctic sea ice tends to be thicker due to the semi-enclosed geographical nature of the Arctic Ocean, while Antarctic sea ice tends to melt mostly each year again as it can drift away freely towards lower latitudes (Serreze & Meier, 2019).

Figure 1: Map of the Arctic. The red box shows the focus area of this study, including the Barents Sea and the archipelago of Novaya Zemlya (Britannica, 2024).

Surface cooling quickly results in sea ice formation due to stratification of the water column (Serreze & Barry, 2014). Sea ice acts as an insulating barrier separating the ocean from the atmosphere (McPhee, 2008). This has far-reaching consequences for air-ice-ocean interactions, i.e. exchanges of fluxes of mass, energy and momentum. Thus they play a crucial role in the Arctic's climate, resulting in changes in glacier mass, ecosystem structure and vegetation types, according to a comprehensive literature review offered by Taylor et al. (2018). Hence, sea ice not only hinders convective heat exchange but also increases the proportion of reflected shortwave radiation (McPhee, 2008). Sea ice is therefore of massive importance for global climate regulation (Comiso et al., 2008; Döscher et al., 2014; Serreze & Barry, 2014).

However, due to the disproportionately high warming in the Arctic, the Arctic sea ice has been severely reduced in recent decades (Serreze & Meier, 2019; Tepes et al., 2021). These SIC changes result in modified temperature gradients, resulting in highly non-linear changes in the regional heat distribution and changes in atmospheric circulation (Petoukhov & Semenov, 2010). Hence, turbulent latent and sensible heat surface fluxes are affected (Uhlíková et al., 2024). In regions where sea ice retreats, seasonal energy exchange varies more strongly, with increased heat storage in summer and intensified upward surface turbulent fluxes in winter (Boeke & Taylor, 2018; Cohen et al., 2020). Consequently, this causes an upward trend in air temperatures and increases humidity in the Arctic, leading to generally warmer conditions and more precipitation along with cloud cover (Boisvert & Stroeve, 2015; Bromwich et al., 2018), being most evident in nearby continents (Cohen et al., 2020).

The Arctic has evolved into a summer and an autumn that are almost sea ice-free and this change in sea ice seasonality affects the thermodynamic processes of sea ice, making it thinner and likely to become even thinner in the long term (Lebrun et al., 2019). This is because the ice has less time to grow during winter, due to weaker winter feedback processes, and melts more rapidly in summer, due to stronger summer feedback processes. For example, Serreze and Meier (2019) used Lagrangian tracking of individual ice parcels to show that multi-year ice, which is generally thicker (Maslanik et al., 2007), is disappearing - either through melting or transport out of the Arctic - at a proportionally higher rate than relatively thin first-year ice. This reduction in average ice age, particularly the complete loss of ice older than five years, intensifies the steepening trend of decreasing SIC (Lebrun et al., 2019).

Given the role of the Arctic as a heat sink in the global atmospheric thermodynamic system, changes in SIC and Arctic climate conditions could influence the efficiency of this heat exchange system (Deser et al., 2015). This, in turn, might lead to warming effects across the globe, especially impacting equatorial areas (Serreze & Barry, 2014). Various examples of changes in climate patterns on all continents caused by the reduction of Arctic SIC are listed in a review by Vihma (2014), demonstrating the importance of studying the Arctic climate more closely.

Several in-depth studies have been conducted on the surface mass balance (SMB) and climate of the Greenland Ice Sheet (GrIS) and its sensitivity to increasing sea surface temperatures (SST) and decreasing SIC (Ding et al., 2014; Noël et al., 2014; Stroeve et al., 2017). Although GrIS represents the largest ice mass in the northern hemisphere, studying other places with significant ice mass is crucial to understanding local climate conditions (Serreze & Barry, 2014). Especially the local climate conditions in the Russian Arctic remain less understood.

The main ice caps in the Russian Arctic are found in Novaya Zemlya and Severnaya Zemlya. The climate in these archipelagos is polar, with maximum temperatures not exceeding 10°C, and the land is classified as tundra by the Köppen-Geiger system, meaning that the temperature of the warmest month is above freezing (Peel et al., 2007). At the same time, the Barents Sea, west of Novaya Zemlya, appears to be the most changing oceanic Arctic since 1980 in terms of sea ice season reduction according to Parkinson (2014) and in terms of SIC shrinkage according to Uhlíková et al. (2024). This results in more evaporation and thus more energy import carried out by more frequent moist atmospheric river events, (Ma et al., 2024). Around Novaya Zemlya, these events are transported by easterly winds, which strengthen dry Foehn wind events on the leeward side of the mountains (Haacker et al., 2024), leading to an important loss of ice mass and therefore making Novaya Zemlya glaciers the most affected glaciers in the Russian High Arctic Island region (Jakob & Gourmelen, 2023). Hence, the climate in the Russian Arctic, especially Novaya Zemlya, is likely to be affected. A projection presented by Beck et al. (2018) seems to support this hypothesis, indicating that by the end of the twenty-first century, the south of Novaya Zemlya is expected to transition from a polar to a cold climate under RCP8.5. For these reasons, we will examine the changes observed in the Barents Sea and in Novaya Zemlya in more detail, as this seems to be a suitable area for studying the effects of a reduction in SIC on the local climate.

The following parts have been divided into a description of the changes observed in the Barents

Sea with the main drivers behind these trends, as described by the literature, the changes observed at Novaya Zemlya, the differences between models and ultimately the objectives studied in this thesis.

1.1 Rapid SIC decrease in the Barents Sea

The Barents Sea region experiences large seasonal contrasts, with rapidly declining partly ice-covered winters and springs on the one hand, and increasing open-water summers and autumns on the other hand, making it one of the most climate-affected polar regions (Gerland et al., 2023; Parkinson, 2014). Its SIC loss is considered a global climate tipping point, even if the average global temperature stays below the Paris agreement's 2-degree limit (Armstrong McKay et al., 2022). In an attempt to explore the changes in skin temperature and SIC observed in the Barents Sea ourselves, we used Python's package *cartopy* to create graphics for the winter (December, January, February - DJF) and summer months (June, July, August - JJA) of 1980-2023 in the Eastern Barents Sea, which we define as the area east of 25°E longitude. The data was sourced from ERA5, the most recent climate reanalysis developed by the European Centre for Medium-Range Weather Forecasts (ECMWF) (Copernicus Climate Change Service, 2023). We categorize the studied period (1981-2023) as 1981-2001 and 2002-2023, as 2000-2001 is commonly regarded as a turning phase in Arctic warming (Steele et al., 2008).

Figure 2 shows the average winter skin temperature and SIC for the average of the years 1981-2001 (Figure 2a and b) and the average of 2002-2023 (Figure 2c and d) based on the ERA5 reanalysis (Copernicus Climate Change Service, 2023). The skin temperature denotes the temperature of the thin, approximately 500 µm, water layer at the air-sea boundary (Donlon et al., 2002). This means that if sea ice covers the ocean, this variable indicates the temperature of the ice rather than the underlying water. An increase in skin temperature is evident between the two periods. Other simulations by Kohnemann et al. (2017) throughout the Arctic indicate that the maximum and most extreme winter warming of the 2-meter air temperature occurred north of Novaya Zemlya in the Kara Sea and the Barents Sea between 2003 and 2012.

In the SIC panels, lighter blue shows SIE with higher SIC up to the 15% sea ice edge marked by a contour line, while darker blue indicates ice-free areas. It can be observed that the ice-free region has expanded throughout the Barents Sea over the years, with winter sea ice still present on the west coast of Novaya Zemlya between 1981 and 2001. In fact, the SST gradient at the polar front — where the eastern Barents Sea meets the fresh, cold Arctic water — has increased significantly (Barton et al., 2018). This has limited the southward expansion of sea ice beyond the front during recent winters. The primary driver of this change is the rising interannual SST of Atlantic water. Consequently, the salinity and density of Barents Sea water have increased, contributing to the Atlantification of the Barents Sea, potentially impacting the Arctic Ocean's circulation (Lebrun et al., 2019).

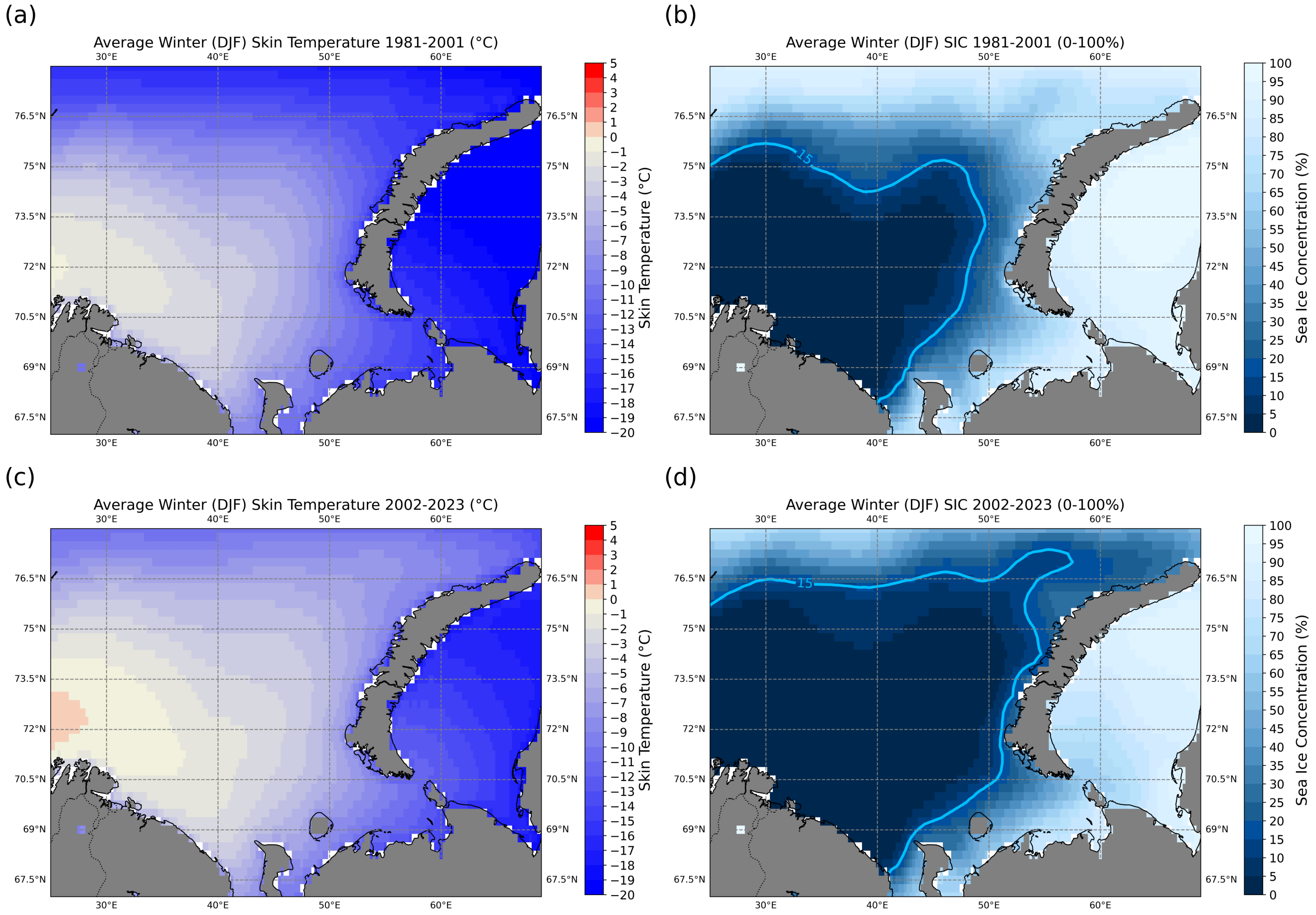

Figure 2: Skin temperatures and SIC during the winter months (December, January, and February - DJF) for the periods 1981-2001 (a, b) and 2002-2023 (c, d) in the Eastern Barents Sea based on the ERA5 reanalysis. Negative skin temperature values (in °C) are represented by shades of light blue to dark blue, with darker tones indicating more negative values. Positive values are similarly represented by shades of red. SIC values range from 0 to 100%, where sea ice-covered regions typically have an SIC greater than 15% as indicated by the blue contour line. Dark blue indicates no sea ice and lighter blue tones indicate higher concentrations of SIC.

Similarly, Figure 3 presents the average summer skin temperatures and SIC for the years 1981-2001 (Figure 3a and b) and 2002-2023 (Figure 3c and d). The figures clearly demonstrate a pronounced seasonal sea ice melt that has intensified over the years, with almost no SIE in winter and entirely gone in the summer months after 2001.

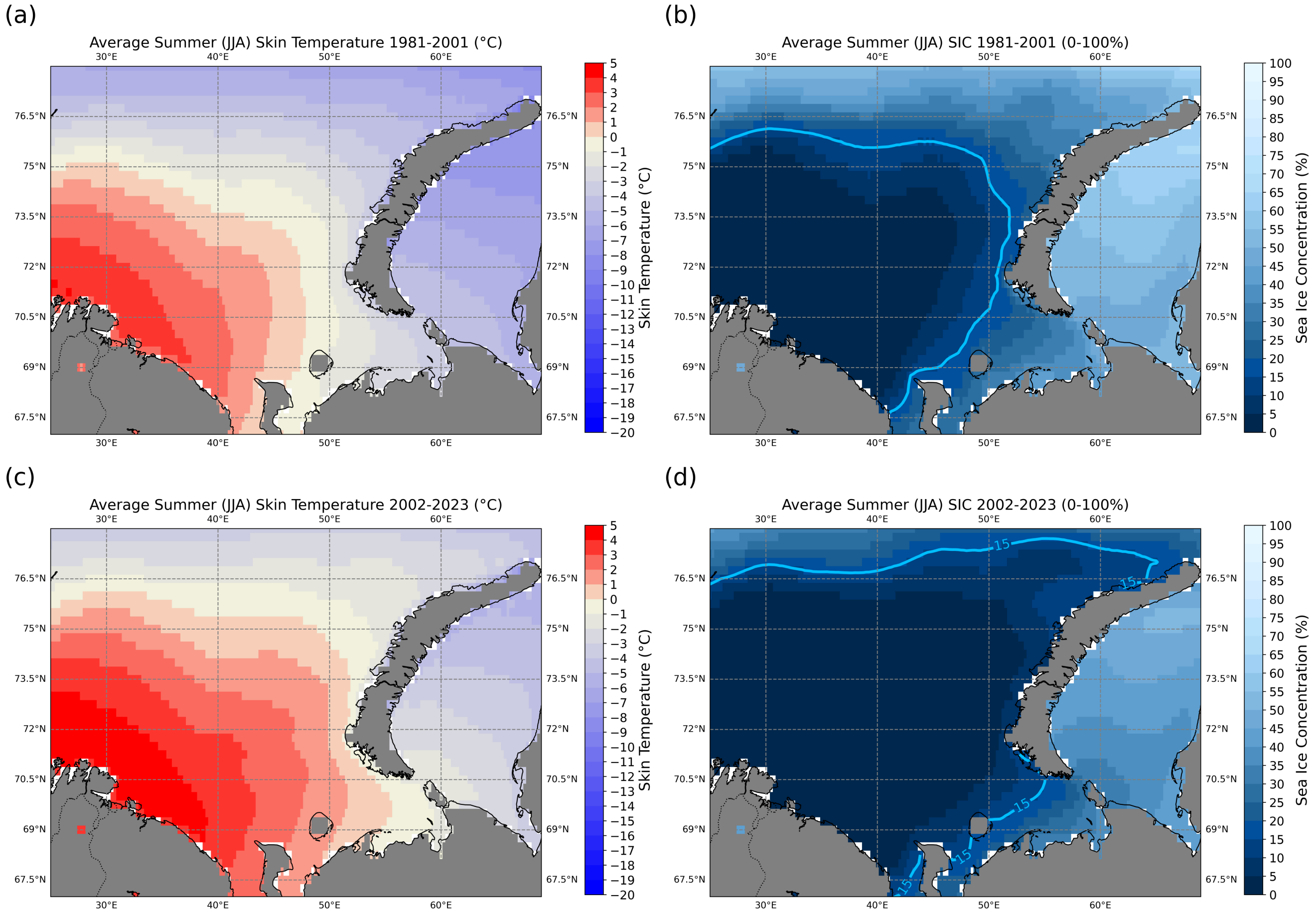

Figure 3: Skin temperatures and SIC during the summer months (June, July, and August - JJA) for the periods 1981-2001 (a, b) and 2002-2023 (c, d) in the Eastern Barents Sea based on the ERA5 reanalysis. Negative skin temperature values (in °C) are represented by shades of light blue to dark blue, with darker tones indicating more negative values. Positive values are similarly represented by shades of red. SIC values range from 0 to 100%, where sea ice-covered regions typically have an SIC greater than 15% as indicated by the blue contour line. Dark blue indicates no sea ice and lighter blue tones indicate higher concentrations of SIC.

There is little agreement in the literature on which drivers are responsible for the increasing trend of skin temperature and the decreasing trend of SIC in the Barents Sea. While some authors suggest that atmospheric factors, such as cyclonic or anticyclonic winds depending on the season (summer or winter), are the primary cause (Dörr et al., 2024; Sorteberg & Kvingedal, 2006), others argue that warm Atlantic water inflow is the main factor behind these trends (Årthun et al., 2012; Barton et al., 2018; Docquier et al., 2020; Kumar et al., 2021; Muilwijk et al., 2018), or that a combination of both is responsible depending on the area or season (Lien et al., 2017; Mohamed et al., 2022b; Pavlova et al., 2014).

In fact, SIC affects the sensitivity of the system to ocean-air variability. When SIC is high, ocean forcing, particularly the inflow of Atlantic water, dominates sea ice variability. However, as SIC decreases significantly, the atmosphere begins to dominate the variations in heat flux in the Barents Sea (Smedsrud et al., 2013). For instance, Dörr et al. (2024) show that there is a causal relationship between local SST in the southern Barents Sea and the SIC. In contrast, in the northeastern Barents Sea, ocean heat transport toward the Arctic has the strongest influence on sea ice. Lien et al. (2017) argue that positive wind stress curls, i.e., cyclonic rotations in the Northern Hemisphere, cause Ekman divergence and thus upwelling. To compensate for this divergence, Atlantic water transport increases along the negative thermal gradient through the Barents Sea. Consequently, advection associated with local winds in the northeastern Barents Sea leads to a decrease in SIC (Moore, 2013).

To quantify the increase in skin temperatures and decrease in SIC, Figure 4, created using NOAA's PyFerret program (NOAA, n.d.-b), shows their temporal evolutions, averaged over the Barents Sea basin pixels, from 1980 to 2023 for winter (solid lines) and summer (dashed lines) months, with a trend line added in red. Although there is considerable variation from one winter to another, the figure reveals a marked trend towards increasingly positive skin temperatures, particularly since 2001, indicating the rapid warming (Figure 4a). The calculated slope of the linear regression winter trend line is 1.17°C/decade, which means that the winter skin temperature increases by an average of 1.17°C each decade in the region. Similarly, Figure 4b shows the evolution of winter and summer SIC as an average for the entire region. The winter slope is -7.1% per decade. What is noticeable is the sharp decline in SIC around 2000 and 2010.

The mostly sea-ice-free summer and autumn mean that the variability of SIC in the winter months can explain 96% of the annual mean Barents SIC (Onarheim et al., 2015). In addition, Mohamed et al. (2022b) concluded the existence of multidecadal SIC variability, since the 5.4-year and 10.7-year time scales showed significant variability. Higher interannual variability was found over the polar front and in areas affected by the inflow of warm Atlantic water, such as the southern regions of Novaya Zemlya (Mohamed et al., 2022b).

Summer skin temperature and SIC also seem to show considerable year-to-year variation. What can be seen is an observed upward trend in summer skin temperatures (0.78°C/decade) and a downward trend in SIC (-4.1% per decade), reaching close to 0% SIC in summer for the entire Barents Sea. A possible explanation for the faster change in recent decades is provided by the study by Mohamed et al. (2022b), which shows that half of all days with marine heatwaves since 1982 occurred in the last decade (2011-2020). These marine heatwave event frequencies are strongly correlated with the increasing positive trend in SST and show significant negative correlations with SIC.

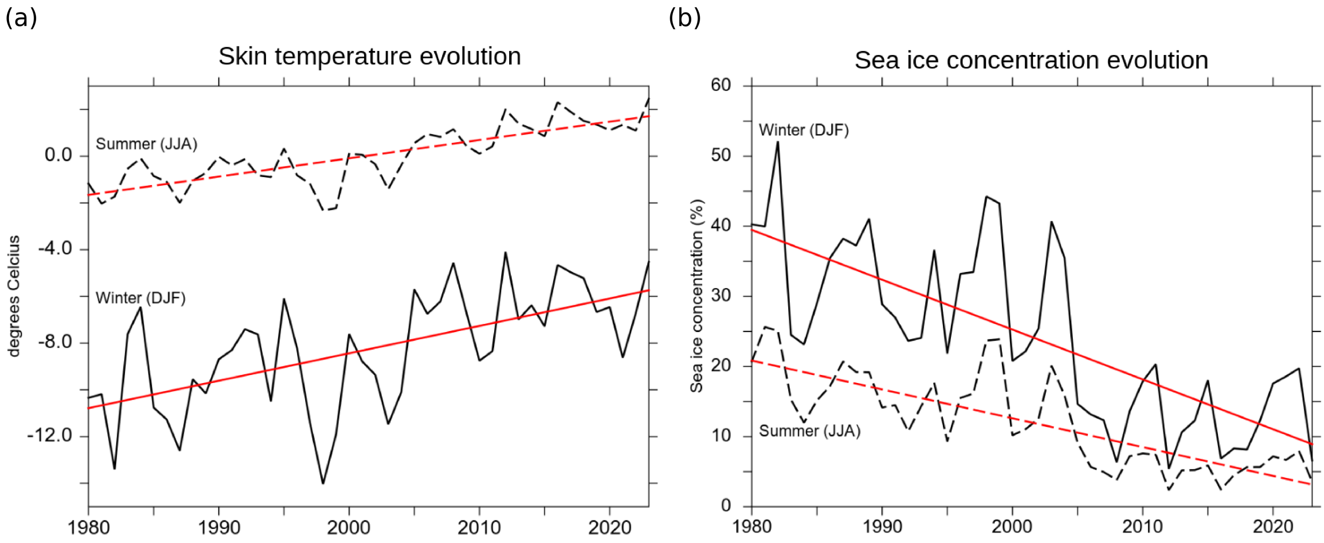

Figure 4: Evolution of skin temperatures and SIC in the Eastern Barents Sea during winter (DJF) (a) and summer (JJA) (b) over the period 1980-2023 based on the ERA5 reanalysis. The Kara Sea, east of Novaya Zemlya, is masked out of the data. Black lines represent the actual values of skin temperatures (in °C) and SIC (%) for winter (solid lines) and summer (dashed lines), with red solid and dashed lines indicating the linear trend for winter and summer months, respectively. The winter trend shows a temperature increase of 1.17°C/decade and a 7.1% SIC decline per decade, while summer trends indicate a 0.78°C/decline temperature rise and a 4.1% SIC decrease per decade.

Other studies, like those of Jakowczyk and Stramska (2014) also seem to confirm a more rapid warming in winter than in summer, particularly in the open Barents Sea area west of Novaya Zemlya. Pavlova et al. (2014) identify the most likely causes as more reduced sea ice transport in winter due to stronger southeastern winds caused by larger sea level pressure gradients, and less mixing of warm Atlantic Ocean water towards the surface in summer. Furthermore, our SIC trend values are supported by the Barents Sea's values reported by Mohamed et al. (2022b), analyzing the SST warming and SIC reduction rates from 1982 to 2020. In this timeframe, their observations reveal a decrease in SIC of 6.52 ± 0.78% per decade, resulting in a reduction in the sea ice season of 26.1 ± 7.5 days per decade or an extended ice-free summer period of 3.4 months during the study period. They claim that the northeastern Barents Sea, specifically between Franz Josef Land and Novaya Zemlya, is believed to be even more affected, showing a more negative trend in the sea ice season of 60 days per decade. This shows that warming trends are not spatially homogeneous across the Barents Sea. However, the sea ice season reduction across the Barents Sea is the most remarkable shrinkage compared to the average 5 days/decade sea ice season reduction seen in the Arctic (Parkinson, 2014).

These trends are likely to continue in the future, since projections by Verezemskaya et al. (2022) indicate that mean surface air temperatures over the Barents Sea are expected to surpass 2 degrees Celsius within the 21st century under climate projections RCP4.5 and RCP8.5.

1.2 Glacier retreat in Novaya Zemlya

Considering changes in the Eastern Barents Sea, it might be worth examining adjacent land changes, like those at Novaya Zemlya. This archipelago in the Russian Arctic is bordered by the Barents Sea to the west and the Kara Sea to the east. Most research on Novaya Zemlya has been focusing on glacier retreat, an important indicator of climate change (Hock & Huss, 2021). Tepes et al. (2021) demonstrate the mass loss of ice caps and glaciers at Novaya Zemlya between 2010 and 2018 to be 9.7 ± 0.5Gt. A study by Ali et al. (2023) addressed Google Earth Engine as a tool for mapping glacier change and found that Novaya Zemlya's glacier area decreased to $21,670 \pm 292$km^2 between 2019 and 2021, corresponding to a 5.8% loss compared to the period from 1986 to 1989. More specifically, the Barents Sea coast experienced a reduction of 7.3%, compared to a 4.2% reduction along the Kara Sea coast.

This important glacier retreat, particularly along the Barents Sea coast, is not only a result of the changes in environmental factors, but also because the characteristics of the glaciers at Novaya Zemlya tend to be more sensitive to climate change (J. R. Carr et al., 2014). A similar pattern was also observed by Kochtitzky and Copland (2022), who highlighted the greater importance of unique glacier-specific factors, such as local characteristics and geometries, in determining glacier sensitivity to climate change, compared to environmental factors alone. For instance, Grant et al. (2009) report that 18% of Novaya Zemlya's glacier area is occupied by surge-type glaciers, which experience cyclic fluctuations with periods of rapid flow velocities and slow flow velocities. This type of glacier is particularly vulnerable to climate change (Kochtitzky & Copland, 2022).

Despite the importance of glacier-specific factors, R. Carr et al. (2023) identify Atlantic water variability as the main contributor to glacier retreat on the Barents Sea coast of Novaya Zemlya, especially as glacier retreat variability on the other side, along the coast of the Kara Sea, does not seem to reveal the same relationship with ocean water temperatures. In fact, J. R. Carr et al. (2017) found that glaciers at Novaya Zemlya that terminate in lakes or the ocean have been melting 3.5 times faster than those terminating on land with particularly rapid melting occurring since 2000 and 2013. These findings are supported by Melkonian et al. (2016), who argue that marine-terminating glaciers along the Barents Sea coast present very high thinning rates, with frontal velocities exceeding those of any other glacier on Novaya Zemlya, particularly in comparison to its land-terminating glaciers. This indicates that ice mass loss occurs not only due to melting but also from significant calving flux, where large chunks of ice break off. Inostrantseva and Vil'kitskogo glaciers are prime examples of fast-retreating glaciers on the Barents Sea coast, where frontal thinning and retreat are driven by high calving rates.

Since glacier retreat is strongly dependent on climate conditions such as air temperatures, wind speed and humidity levels (Hock & Huss, 2021), these examples seem to indicate that the climate at Novaya Zemlya has been changing, while at the same time large changes in SIC at the Barents Sea were observed. However, to our knowledge, published studies that have investigated the effects of changing SIC in the Barents Sea on the climate of Novaya Zemlya since 1980 are limited. Nevertheless, a good understanding of the Arctic climate is essential for understanding the role of the Arctic in the Earth's changing climate (Huang et al., 2017; McGuire et al., 2006).

1.3 Earth System Models vs. Regional Climate Models

To enhance policy decision-making, scientists have developed climate models to describe past, actual and future values of various essential climate variables (Tapiador et al., 2020). Hence, we distinguish Earth System Models (ESM), which numerically describe the Earth's climate by combining physical equations with biological and chemical processes (Climateurope, n.d.) at low spatial resolution, from Regional Climate Models (RCM). RCMs are also numerical models, often coupled with ocean circulation or sea ice models, typically nested within or forced by an ESM, focusing at high spatial resolution on a specific region within the changing global climate. This allows for higher grid resolutions within the limits of available computational power and is better suited to represent local and regional processes, knowing that their physics and parameterisations can be tuned to a specific climate (Flato et al., 2014; Leung, 2012). More particularly, the physics of the Arctic region is poorly represented in current ESMs, or their predecessors Global Climate Models (GCMs), as atmospheric characteristics like convection and turbulence, especially in the lower troposphere, differ significantly from those at lower latitudes. As a result, SIC concentrations are not accurately represented in each region using an ESM (Notz et al., 2013). Hence, RCMs might be useful in improving our understanding of the Arctic climate (Eisenman et al., 2007; Serreze & Barry, 2011).

1.4 Objectives

In Arctic climate and ocean modeling studies, more research efforts focus on the Greenland region (Ding et al., 2014; King et al., 2020; Mouginot et al., 2019; Noël et al., 2014), but fewer researchers have addressed the region around Novaya Zemlya and the Barents Sea despite the large changes observed in these regions. As a result, climate and atmospheric conditions of the Barents Sea and Novaya Zemlya remains poorly understood and could benefit from high-resolution RCM analysis. Especially since ESMs have faced the challenge of Barents Sea bias, where observed winter and spring surface air temperatures were systematically 6-8°C warmer than modeled in 12 out of 14 investigated GCMs in the study, due to the difficulty in accounting for the absence of sea ice in this Arctic region in such models (Chapman & Walsh, 2007). Due to the different effects of sea ice on local climate in different seasons, sparse resolution climate models tend to represent the reality with a large spread (Boeke & Taylor, 2018). Huang et al. (2017) and McGuire et al. (2006) emphasize the importance of understanding changes in local Arctic climate conditions due to perturbations in oceanic factors such as reduced SIC and increased SST, since this might be important in assessing the Arctic's role in Earth's climate.

More specifically, the aim of this thesis is to assess the sensitivity of atmospheric conditions in the Barents Sea and Novaya Zemlya, an area to which much less research efforts have been dedicated despite the strong changes seen in the Barents Sea, to variations in skin temperatures and SIC in the Eastern Barents Sea using the RCM ***M**odèle **A**tmosphérique **R**égional* (MAR). In this way, this study provides new insights into the sensitivity of a local Arctic climate to changes in SIC. The primary focus of this study will be on the winter season, as Arctic amplification in this region appears to affect this season more strongly than summer, which seems to be confirmed by our calculated trend values for SIC decline.

2 Data and methods

This section outlines the methodology used in this master's thesis. It begins with an explanation of the regional climate model MAR, followed by the experiment design, model validation, variable selection, and data processing and analysis. Additional code and scripts are available on GitLab via the link https://gitlab.com/stefvh/ms-thesis-barents-sea. These scripts are numbered, and references to them will be made in the following sections.

2.1 The regional climate model MAR

In our study, the regional climate model MAR is used to study the climate in our domain. MAR stands for *Modèle Atmosphérique Régional* and was originally developed to study polar climates and ice sheets, such as the Greenland Ice Sheet (Fettweis et al., 2005, 2017; Hanna et al., 2020). However, the model knows use cases in various regions, such as Belgium (Doutreloup et al., 2019). MAR consists of a 3D atmospheric module and a 1D surface transfer scheme, which focuses on the vertical processes at each surface point and couples the land, ocean surface, and atmosphere. This scheme, known as Soil Ice Snow Vegetation Atmosphere Transfer (SISVAT), is described in Ridder and Schayes, 1997 and Gallée et al., 2004. The atmospheric module solves the (non-)hydrostatic primitive equations, while the radiative scheme from ECMWF is implemented as detailed in Morcrette, 2002. A more comprehensive description of the model can be found in Gallée and Schayes, 1994 and Gallée et al., 1995. MAR's modules and schemes are also summarized in (Fettweis et al., 2017). The full code of MARv3 is accessible with a GitLab account through gitlab.com/Mar-Group/MARv3.

Regional climate model grid cells are forced with initial and lateral boundary conditions for temperature, zonal and meridional wind components, and specific humidity every six hours at each MAR vertical level in addition to the surface pressure, typically derived from large-scale model outputs such as reanalysis data. In MAR, ocean grid cells are also forced with six-hourly SST and SIC data as MAR is not coupled here with an ocean model like NEMO. For the Barents Sea–Novaya Zemlya region, the initial conditions are provided by ERA5 SST and SIC data for all longitudes north of 40°N since 1980 (Copernicus Climate Change Service, 2023). At the boundaries of the regional domain, MAR includes a relaxation zone, defined as a 7-pixel wide band (extended here to 15 pixels) between the regional and large-scale domains (Marbaix et al., 2003). This zone should not be included in the analysis, as inaccuracies may arise due to the downscaling required to transition from low large-scale model resolution to high regional grid resolution.

Appendix A.1 provides details on the MAR pre-processing software for grid initialization and boundary forcings.

2.2 Sensitivity experiment

The years 2000-2001 appear to mark a climate shift era for the Barents Sea–Novaya Zemlya region, as a drastic change in SIC has been observed since then (Steele et al., 2008). Therefore, two time periods are analyzed: 1981–2001 (P1) and 2002–2023 (P2). In this study, winter for any given year consists of the average daily values for January and February of that year, and December of the previous year.

The starting point of P1 is set to 1981, as SST observations became more reliable with the advent of high-quality satellite data. One objective of this study is to compare the evolution of atmospheric conditions between P1 and P2. However, the primary goal is to identify the relationship and interconnection between these atmospheric conditions and changes in SST and SIC. To achieve this, the sensitivity of atmospheric conditions to SIC and SST changes is tested using two hindcast simulations performed with a regional climate model.

In the first simulation (run1), actual SST and SIC data from ERA5 are prescribed into MAR to simulate atmospheric conditions. These data for all longitudes north of 40°N from 1981 onward were retrieved from the ERA5 portal, the latest climate reanalysis developed by the European Centre for Medium-Range Weather Forecasts (ECMWF) (Copernicus Climate Change Service, 2023).

In contrast, the second simulation (run2) does not use actual ERA5 SST and SIC data as MAR forcing. Instead, it assigns a climatological value for each day of the year, based on the average SST and SIC values from 1980 to 1999 (derived from ERA5). This setup assumes that SST and SIC follow the same annual cycle each year, creating a hypothetical scenario in which SIC remains partially present. To optimize computational resources, run2 only covers P2, which is more relevant given the SIC and SST changes illustrated in Figures 2, 3, and 4. The key difference between run1 and run2 is that in run1, sea ice may be largely absent in P2, whereas in run2, sea ice is still present based on historical climatology. By comparing these two runs, we can improve our understanding of how sensitive atmospheric variables are to SIC changes, particularly in P2. More specifically, this comparison helps to evaluate the effects of complete SIC absence (run1) versus partial SIC presence (run2), with all other parameters remaining the same. Hence, this approach directly addresses the research questions.

The climatologies for run2 were calculated using Fortran. Values for February 29th in leap years were excluded from the climatology calculation, resulting in a dataset of 365 values per pixel for SST and SIC. In leap years, February 29th was assigned the same values as February 28th. Another element to consider are potential differences between ERA5 land sea mask and MAR land sea mask in how certain regions, such as fjords, are classified as either continental or ocean pixels. To prevent missing data when forcing MAR with ERA5 data, SIC and SST values were also assigned to land pixels based on the nearest ocean pixels. The full climatology calculation scripts are provided in GitLab script 1 and 2.

2.3 Model validation: comparison with observations

Due to the sparse availability of observational data, models like MAR are useful to increase our understanding on atmospheric conditions. While MAR has been extensively validated over Greenland, its performance in the Barents Sea region remains unassessed. To evaluate the quality of MAR simulations, the results of run1 are compared with observational station data for sea level pressure, 2-meter air temperature, and average 10-meter wind speed, as well as downward radiation data from CERES.

In total, data from 19 stations were used for comparison, as shown in Figure 5. Only stations with more than two years of non-missing data between 1981 and 2023 were included. The stations are located along the coasts of the Barents Sea in Novaya Zemlya (NZ), mainland Russia (RU), Svalbard (SV), and mainland Norway (NO). Of these, data for one station were obtained from the Norwegian Center for Climate Services (NCCS) Observations and Weather Statistics Portal (NCCS, 2025), while the remaining 18 stations are part of the NOAA daily observational dataset, which contains daily weather station data from around the world (NOAA, 2025).

Data from 1980-2023 were obtained as CSV files, selecting mean air temperature, sea level pressure, and average wind speed as variables. In the NCSS dataset, all variables were already in the same units as the MAR data: temperature in degrees Celsius, sea level pressure in hPa, and wind speed in meters per second. Therefore, only the NOAA dataset has been converted to the international system.

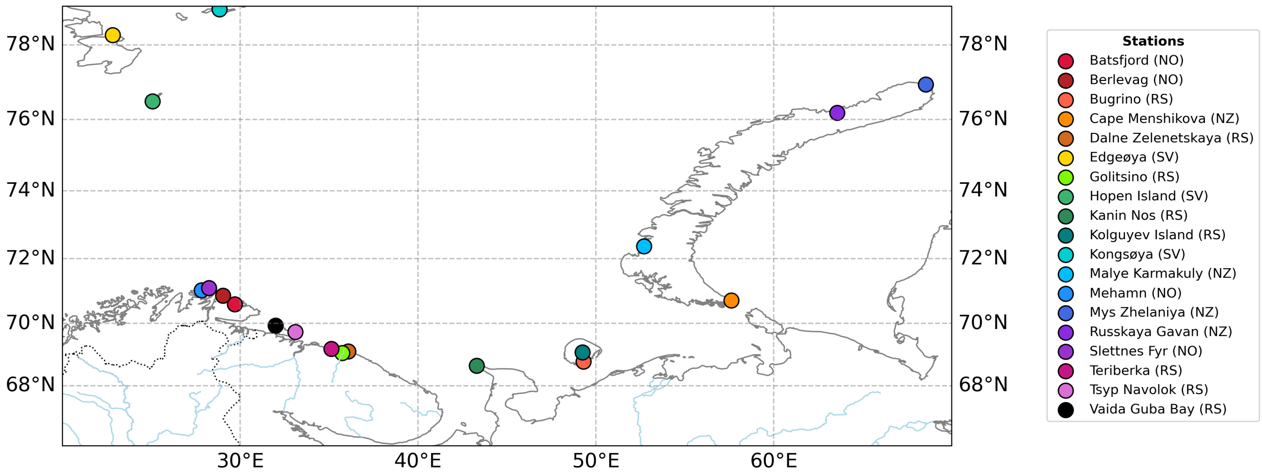

Figure 5: Map showing observation stations around the Barents Sea used to evaluate the quality of run1 model output. The stations are located in Novaya Zemlya (NZ), mainland Russia (RS), Svalbard (SV), and mainland Norway (NO).

Since MAR uses a kilometric grid, regridding was required to align the model output with the station coordinates. This was performed in Python using the nearest neighbor regridding algorithm from the xESMF package, ensuring that the closest land pixel was used for comparison (Jiawei, 2025). Monthly averages were then computed for both the MAR and observational datasets applying the mean function on Python's Pandas DataFrame resampler, specifying `'ME'` (pandas via NumFOCUS, 2024). The comparison was based on these monthly values, from which statistical metrics were derived, including Pearson's correlation coefficient (R), mean absolute error (MAE), bias, root mean squared difference (RMSD), standard deviation (STD), and normalized standard deviation (NSD) (relative to station STD). These metrics were calculated using Python's NumPy package (NumPy team, 2025). As MAR provides continuous data for 1980–2023, but observational records contain gaps and missing values, it was essential to restrict the analysis to the valid time period of each station and exclude missing values when computing metrics. This was ensured using a mask with NumPy's `isnan` function (NumPy team, 2025). The full script is available in GitLab script 5.

Similarly, monthly mean sea level pressure and temperature data from ERA5 daily reanalysis were compared to assess whether any potential bias in MAR could be attributed to biases in the ERA5 forcing or to the MAR model itself. Since ERA5 is known to underestimate wind speeds, particularly during strong winter winds in coastal regions, its wind data were not considered in this analysis (Gandoin & Garza, 2024).

For downward radiation, daily 1°-resolution data for the region 25°E–70°E, 67°N–78°N from the

Clouds and the Earth's Radiant Energy System (CERES) project were used (NASA/LARC/SD/ASDC, 2025). These data were available from 2000 to 2023. The CERES team is part of the National Aeronautics and Space Administration (NASA), and its instruments are aboard various satellites, such as Aqua and Terra (NOAA, 2024). Similarly to the station data, monthly averages were computed, but this time for the average of the CERES data for the entire region, which were compared to the spatial averages of the MAR data.

2.4 Variable selection

Based on the variables most closely linked to changes in SIC and SST, a selection of focus variables has been chosen for this study. These include 2-meter air temperature (T2M) and 10-meter wind speed (WDSP), which is computed as the square root of the sum of the squares of the zonal (U10) and meridional (V10) components, as shown in Equation 4.

$$\text{WDSP} = \sqrt{U_{10}^2 + V_{10}^2} \tag{1}$$

Additionally, this study focuses on cloudiness, specifically low cloud cover (CD), which refers to clouds below 2,000 meters in altitude (NOAA, 2023). These clouds have been shown to be linked to changes in sea ice and open water (Li et al., 2023). Other selected variables include surface mass balance (SMB) net surface heat flux (Q_{net}). To compute SMB, snowfall, runoff of meltwater and rainwater, sublimation from snow/soil and meltwater production are taken into account (Kittel et al., 2021), while Q_{net} is determined by the balance of radiative and turbulent heat fluxes, as expressed in Equation 5 (Qiao et al., 2025):

$$Q_{net} = LWD + SWD - LWU - SWU - SHF - LHF \tag{2}$$

where LWD and SWD are longwave and shortwave downward radiation, LWU and SWU are longwave and shortwave upward radiation, and SHF and LHF represent sensible and latent heat flux, respectively.

Sea level pressure (SLP) is also included to assess the quality of the model outputs, as this variable should be consistent between model simulations and observations.

Although humidity levels are also likely associated with changes in SST and SIC, they are not well represented in MAR at this stage (not shown) and tend to be overestimated. Therefore, this

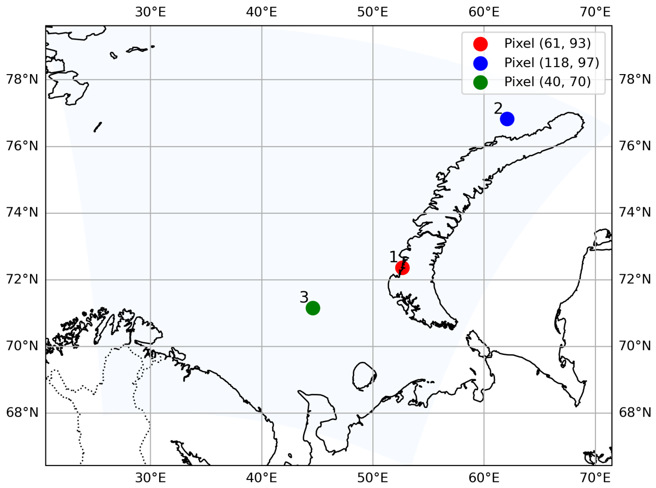

Figure 6: Map with three random pixels selected for calculating data distribution metrics. Pixel 1 corresponds to (52.66°E, 72.26°N), pixel 2 to (62.08°E, 76.92°N) and pixel 3 to (44.61°E, 71.15°N).

variable is excluded from the analysis.

2.5 Processing model outputs before analysis

The MAR output netCDF files contain daily values for various variables. However, when performing an interannual analysis and comparing different periods, merged files are required. Since the files are too large to merge all at once, details on this merging process are in GitLab script 4.

2.6 Data distribution

For each dataset (DJF and JJA data in P1 and P2), skewness and kurtosis were computed for each variable. Skewness (α_3) measures the asymmetry of a distribution, while kurtosis (α_4) represents its peakedness. A normal distribution has (α_3) and (α_4) values close to 0. If (α_3) is less than or greater than 0, the left or right tail, respectively, is longer. If (α_4) is negative, the peak is flatter than that of a normal distribution, whereas if it is positive, the peak is sharper. To test for normality, the Shapiro-Wilk test was used. The null hypothesis assumes that the data follow a normal distribution; if rejected, the data are not normally distributed. This test is effective for sample sizes up to 50. Since our dataset consists of a large number of pixels, exceeding this threshold, three data pixels are randomly selected, as shown in Figure 6. The pixels correspond to (52.66°E, 72.26°N), (62.08°E, 76.92°N) and (44.61°E, 71.15°N). For each of these pixels, there are 44 data points, which were used to assess normality for the selected variables (Mishra et al., 2019).

Table 1 presents the values of α_3, α_4, the Shapiro-Wilk test statistic (W), and the corresponding p-values for DJF. For T2M, all pixels across all datasets follow a normal distribution, as the null hypothesis is not rejected. For WDSP, normality is violated in DJF for P1 run1 at pixel 1. Regarding Q_{net}, two exceptions to normality were found: one in the DJF P1 (run1) dataset at pixel 2 and another in the DJF P2 (run2) dataset at pixel 1. Similarly, CD is likely normally distributed, except for pixel 2 in the DJF P2 (run2) dataset. For SMB, normality statistics could not be calculated for pixels 2 and 3, as valid values exist only over land. However, in pixel 1, all datasets can be assumed to follow a normal distribution.

Given that most pixels for all variables do not reject normality, we assume a normal distribution for the statistical tests used in the analysis.

Table 1: Skewness (α_3), kurtosis (α_4), Shapiro-Wilk test statistic (W) and the corresponding p-value for normality across three random pixels (1), (2) and (3) for the three winter season (DJF) datasets. Pixel 1 corresponds to (52.66°E, 72.26°N), pixel 2 to (62.08°E, 76.92°N) and pixel 3 to (44.61°E, 71.15°N).

	DJF P1 (run1)				**DJF P2 (run1)**				**DJF P2 (run2)**			
Variable	α_3	α_4	W	p	α_3	α_4	W	p	α_3	α_4	W	p
T2M (1)	0.25	-0.58	0.95	0.32	0.14	-0.34	0.98	0.94	0.28	0.00	0.98	0.88
T2M (2)	0.53	0.26	0.96	0.60	-0.80	-0.38	0.91	0.04	-0.08	-0.62	0.98	0.85
T2M (3)	-0.47	-0.20	0.93	0.15	-0.13	-0.53	0.98	0.96	0.28	-0.66	0.97	0.73
WDSP (1)	0.87	-0.01	0.90	0.04*	0.17	-0.02	0.97	0.72	-0.02	-0.28	0.99	0.98
WDSP (2)	0.99	1.05	0.93	0.15	0.50	-0.55	0.96	0.48	0.50	-0.61	0.94	0.24
WDSP (3)	0.60	-0.34	0.95	0.30	0.76	-0.10	0.94	0.19	0.77	0.13	0.94	0.19
Q_{net} (1)	0.80	-0.35	0.92	0.07	-0.35	-0.27	0.97	0.62	-1.29	2.79	0.90	0.04*
Q_{net} (2)	1.98	3.93	0.77	0.00*	-0.02	-1.06	0.97	0.61	0.27	-0.70	0.97	0.65
Q_{net} (3)	-0.32	-0.86	0.94	0.22	0.10	-0.64	0.98	0.87	0.32	-0.54	0.97	0.81
CD (1)	-0.21	-0.30	0.96	0.46	-1.26	1.83	0.91	0.03	-0.91	0.34	0.93	0.10
CD (2)	-0.67	-0.40	0.94	0.20	-0.99	0.81	0.93	0.09	-1.22	1.24	0.89	0.02*
CD (3)	-0.26	0.52	0.95	0.37	-0.77	-0.65	0.89	0.01	-0.37	-0.48	0.95	0.29
SMB (1)	0.27	-0.37	0.97	0.77	0.58	-0.35	0.96	0.49	0.69	-0.17	0.94	0.17
SMB (2)	-	-	-	-	-	-	-	-	-	-	-	-
SMB (3)	-	-	-	-	-	-	-	-	-	-	-	-

2.7 Analysis and statistical tests

To determine whether the difference in means between two periods of a variable at a specific pixel is statistically significant, this study employs a two-sample t-test. Both datasets consist of continuous and independent data and, as demonstrated in the previous section, are approximately normally distributed. Furthermore, the variances of the two datasets should be comparable. A comparison of the standard deviations of the DJF datasets, as shown in Table 2, indicates that the variances are of similar magnitude. Therefore, the Student t-test is appropriate for this analysis. The test is also applied to compare the model outputs between run1 P1 and P2, as well as between run1 P2 and run2 P2. Additionally, the same t-test is used to evaluate whether the Pearson correlation coefficients between SIC and the selected variables are statistically significant, using the `pearsonr` function from the same package (The SciPy community, 2025). The full Python scripts are to be found in GitLab scripts 6, 7 and 8.

Table 2: Mean and standard deviation of different variables during DJF (December–January–February) periods.

	T2M (°C)		WDSP (m/s)		Q_{net} (W/m^2)		CD (%)		SMB (mmWE/day)	
	Mean	Std	Mean	Std	Mean	Std	Mean	Std	Mean	Std
DJF P1 (run1)	-11.80	7.32	3.10	1.71	36.76	84.53	0.85	0.08	0.26	0.63
DJF P2 (run1)	-8.08	6.72	3.08	1.62	40.28	77.31	0.82	0.09	0.27	0.66
DJF P2 (run2)	-9.46	6.49	2.96	1.58	20.85	69.91	0.85	0.08	0.26	0.64

2.8 Use of generative AI

In the context of this master's thesis, generative AI tools, specifically the free ChatGPT-3.5 model, were used in accordance with the permitted uses defined by the ULiège Charter for the use of generative artificial intelligence in academic work (ULiège, 2023). In particular, this included use as a linguistic assistant to improve the formulation of self-written texts and for translation purposes, as well as an information search assistant, such as identifying appropriate keywords or domain-specific terms for literature searches. Additionally, ChatGPT was used to check the existence of relevant Python libraries and to help interpret or resolve error messages related to Fortran or Python code used for figure creation and analysis.

3 Results

3.1 Model comparision with observations

This section presents and discusses the metric tables comparing MAR model outputs to DJF observations or reconstructions. Table 3 reports Pearson's correlation coefficient, mean absolute error (MAE), bias, root mean squared deviation (RMSD), and normalized standard deviation (NSD) between DJF MAR data and station observation data for SLP, T2M, and wind speed, respectively. Table 4 represents the CERES vs. MAR comparison of SWD and LWD metrics, averaged over the region 25°E–70°E, 67°N–78°N for DJF months.

All other tables and figures are provided in Appendix A.2. First, this includes the station observation metric tables for ERA5 (DJF months) (Table A.2.5) and MAR (all months) (Table A.2.6) comparing these datasets with observations. Furthermore, plots for each station illustrate variable patterns for station data, MAR, and ERA5 (Figures A.2.17 to A.2.35). Similarly, a plot comparing shortwave and longwave downward radiation from CERES with MAR, averaged over the region, is shown in Figure A.2.36 in the same appendix.

For SLP, correlation coefficients are generally high, typically 0.95 or above, except at a few stations such as Dalne Zelenetskaya, Edgeøya, Golitsino, Kolguyev Island, and Tsyp Navolok. The lower correlations at these sites can likely be attributed to shorter data availability and frequent missing values, often surrounded by anomalous behavior or outliers, as can for instance be observed for the Edgeøya station in Appendix A.2, Figure A.2.22. Despite these limitations, MAR's performance remains comparable to ERA5 in terms of correlation and MAE, with MAE values generally low, between 0 and 2 hPa.

Similarly, T2M also shows high correlation coefficients, although these are generally lower when restricted to the winter months compared to values based on the full annual cycle (see Appendix A.2, Table A.2.6). This is likely due to the more extreme interannual winter temperature variations and the less defined seasonal cycle compared to the full year. Winter temperature biases are negative at two stations (Dalne Zelenetskaya and Tsyp Navolok), and biases range from 0.72°C (Dalne Zelenetskaya) to –4.66°C (Ruskaya Gavan). For several stations, the absolute values of the biases are close to the MAE values. In contrast, ERA5 shows different biases, ranging from 2.24°C (Golitsino) to –3.12°C

(Berlevag), with half of the stations indicating positive biases and the other half negative biases, thereby highlighting T2M differences between MAR and ERA5. This shows well that MAR simulates its own boundary layer with respect to the one of ERA5. The lowest T2M correlation coefficients occur at Golitsino (0.70) and Tsyp Navolok (0.56), suggesting biases in the observations, as the correlation is significantly higher for stations near these two, and there is no reason to expect poor results on just a few pixels, given that the MAR fields are spatially continuous.

Wind speeds, on the contrary, exhibit weaker correlations than both T2M and SLP, with values ranging from 0.28 (Mehamn) to 0.87 (Malye Karmakuly), though still positive and relatively high. This is expected, as 10-meter wind speeds display a less pronounced seasonal cycle than temperature. MAR consistently overestimates wind speeds, with biases ranging from 0.37 m/s at Kolguyev Island to 4.49 m/s at Russkaya Gavan. RMSD values range from 1.06 m/s (Kolguyev Island) to 5.08 m/s (Golitsino). For most stations, NSDs are close to 1, suggesting that MAR reproduces wind speed variability reasonably well. However, when considering wind speeds across all months (Appendix Table A.2.6), correlations are slightly higher, and NSDs also appear to be slightly higher, though still around 1, except for Golitsino (1.69) and Hopen Island (1.50). In particular, the plots in the appendix suggest that MAR often tends to overestimate maximum outliers, as can, for instance, be seen in Figure A.2.28.

Table 3: Comparison of station vs. MAR metrics for DJF months for SLP, T2M, and WDSP.

Station	SLP					T2M					WDSP				
	R	MAE	Bias	RMSD	NSD	R	MAE	Bias	RMSD	NSD	R	MAE	Bias	RMSD	NSD
Batsfjord	0.99	1.21	0.44	1.70	0.95	0.82	2.70	-2.65	2.85	0.90	0.79	1.74	1.71	1.91	1.14
Berlevag	0.98	1.17	0.16	1.97	0.93	0.89	4.67	-4.67	4.73	1.08	0.54	1.98	1.97	2.32	1.18
Bugrino	0.97	1.37	0.36	2.21	0.96	0.95	1.77	-1.69	2.33	1.12	0.73	1.92	1.87	2.09	1.15
Cape Menshikova	1.00	0.47	0.37	0.54	1.00	0.96	1.64	-1.26	1.90	0.95	0.66	1.84	1.84	2.16	0.87
Dalne Zelenetskaya	0.91	3.81	0.81	4.83	0.77	0.81	2.40	0.72	3.09	0.44	0.43	3.78	3.61	4.05	0.81
Edgeøya	0.87	2.22	0.19	4.97	0.81	0.94	3.33	-3.32	3.76	1.04	0.84	1.47	1.15	1.64	0.65
Golitsino	0.88	2.90	0.65	5.62	0.75	0.70	2.80	-1.07	4.10	0.51	0.57	4.96	4.96	5.08	1.16
Hopen Island	1.00	0.38	0.20	0.54	1.00	0.98	0.85	-0.39	1.12	1.09	0.65	4.36	4.36	4.48	1.14
Kanin Nos	0.99	1.01	0.66	1.57	0.99	0.98	0.95	-0.77	1.28	1.19	0.58	1.06	0.83	1.32	1.12
Kolguyev Island	0.91	2.85	2.10	4.19	0.90	0.95	3.92	-3.89	4.20	1.04	0.73	0.84	0.37	1.06	0.93
Kongsøya	1.00	0.34	0.32	0.38	1.00	0.96	1.28	-0.99	1.67	1.14	0.86	1.74	1.74	1.94	1.03
Malye Karmakuly	1.00	0.61	0.49	0.83	0.99	0.99	2.77	-2.77	2.89	1.09	0.87	2.45	2.44	2.64	0.98
Mehamn	0.99	1.25	1.02	1.83	1.02	0.92	3.87	-3.87	3.92	1.06	0.28	2.27	2.27	2.57	1.35
Mys Zhelaniya	0.96	1.36	0.78	2.35	1.01	0.97	1.93	-1.79	2.16	0.93	0.79	1.16	1.08	1.35	1.00
Russkaya Gavan	0.98	1.46	1.46	2.07	0.98	0.96	4.66	-4.66	4.81	0.85	0.81	4.49	4.49	4.63	1.19
Slettnes Fyr	0.98	1.19	0.85	2.06	0.98	0.91	3.34	-3.31	3.42	1.04	0.44	1.78	1.63	2.23	0.76
Teriberka	0.98	1.02	0.16	1.79	0.95	0.94	4.22	-4.22	4.34	0.92	0.63	1.55	1.44	1.84	0.89
Tsyp Navolok	0.80	3.39	0.44	6.80	0.74	0.56	1.86	1.32	3.09	0.44	-	-	-	-	-
Vaida Guba Bay	0.98	1.11	-0.33	1.91	1.01	0.78	2.23	-1.88	2.47	0.79	-	-	-	-	-

In the comparison between CERES and MAR for SWD and LWD radiation metrics (Table 4), averaged throughout the region, the correlation coefficients are high, particularly for SWD, which reaches 0.99. SWD peaks are slightly overestimated, with a bias of 0.26 W/m^2 and a MAE of 0.28 W/m^2. A similar overestimation is observed for LWD, which shows a bias of 6.53 W/m^2 and an MAE of 6.72 W/m^2. The NSDs for both variables are close to 1, indicating that the variability in MAR aligns well with that of the CERES reconstruction.

Table 4: CERES vs. MAR comparison of SWD and LWD metrics, averaged over the region 25°E–70°E, 67°N–78°N for DJF months.

Variable	R	MAE	Bias	RMSD	NSD
SWD	0.99	0.28	0.26	0.53	1.14
LWD	0.93	6.72	6.53	7.80	0.92

3.2 Comparison before and after the 2000-2001 SIC shift and trends

The following sections compare run1 average DJF figures for P1 vs. P2 for the selected variables.

3.2.1 2-meter air temperatures (T2M)

Figure 7 presents the climatological mean daily T2M during the winter months for P1 (a), P2 (b), the difference between P2 and P1 (c), and the linear decadal trend since 1981 (d), based on MAR model output for run1. T2M varies considerably across the Barents Sea, remaining generally below 0°C. The warmest temperatures occur in the southwestern Barents Sea, north of Norway, fluctuating around the freezing point. In contrast, the coldest DJF temperatures, around –20°C or lower, are found over land at Novaya Zemlya.

When comparing P2 to P1, the largest differences, reaching up to 9°C, are observed in the northern Barents Sea, coinciding with the region experiencing the most pronounced decline in SIC (Figure 7c). Across the entire Barents Sea and Novaya Zemlya, T2M shows significant differences between P2 and P1, with linear warming trends reaching up to 2.7°C per decade (Figure 7d). In contrast, summer (JJA) T2M increased by no more than 3°C between P2 and P1, as shown in Appendix A.3, Figure A.3.37c. In the southern Barents Sea, DJF temperature increases are more moderate, ranging from 1 to 2°C between P2 and P1 or approximately 0.9°C per decade, but these increases remain statistically significant.

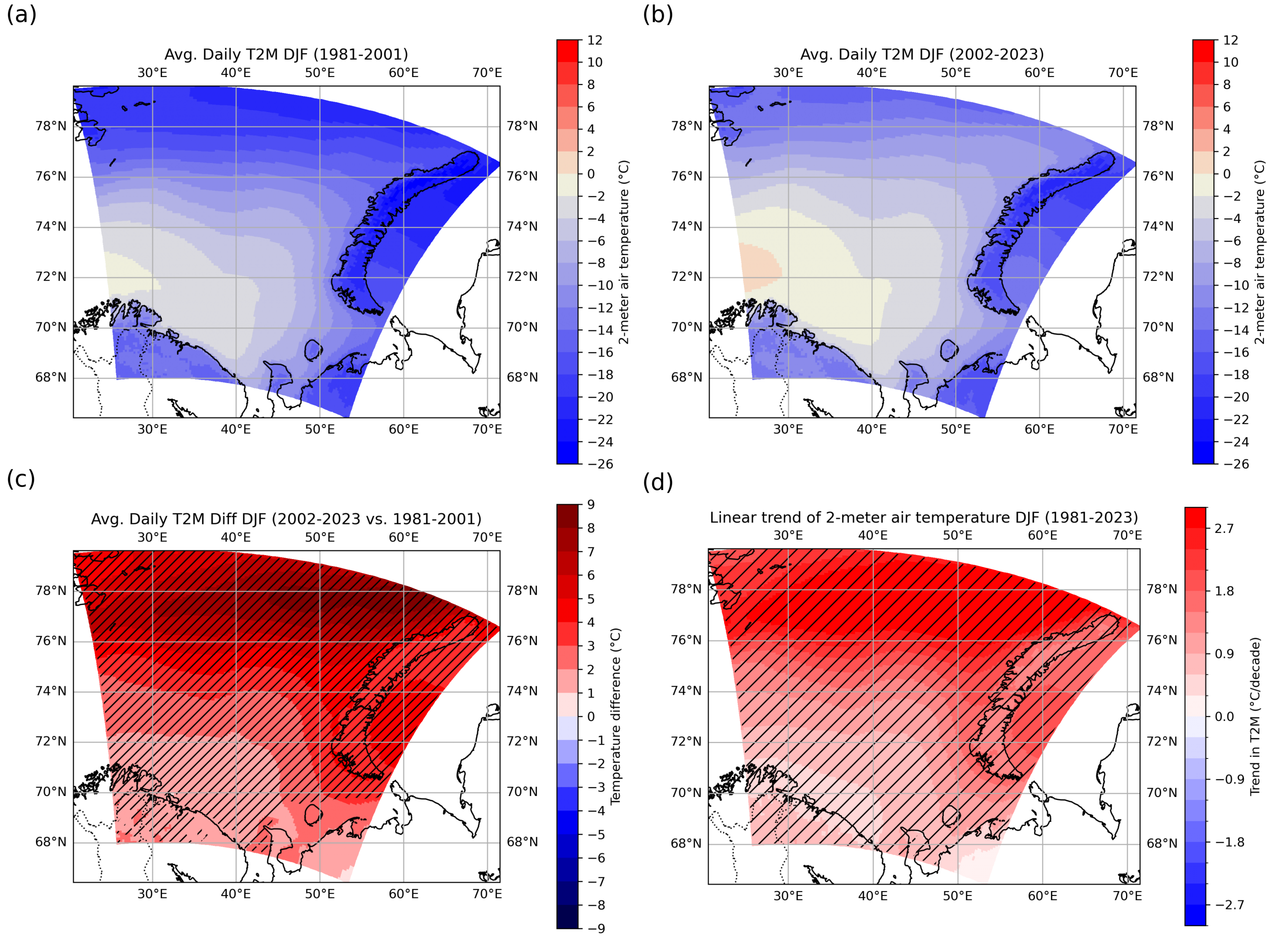

Figure 7: Mean daily T2M (°C) for winter (DJF) for the periods 1981–2001 (a) and 2002–2023 (b), as well as the differences between the two periods (c) and its linear decadal trend value between 1981 and 2023 (d), based on model simulations (run1) using actual SST and SIC values from ERA5 reanalysis data. Significant differences, determined using a Student's t-test with a p-value of 0.05 or lower, are indicated by hatching.

3.2.2 Net surface heat flux

Figure 8 presents the mean daily Q_{net} during the winter months for P1 (a), P2 (b), the difference between P2 and P1 (c), and the linear decadal trend since 1981 (d), based on MAR model output for run1. Positive values (red) indicate heat absorption, while negative values (blue) represent heat release. Open ocean areas typically absorb heat, whereas land and regions covered by (partly) sea ice generally do not. While heat absorption is related to temperature increase, the two are not equivalent. Maximum Q_{net} values, around 200 W/m^2, are found in the central Barents Sea, while the lowest values, approximately –100 W/m^2, occur in the northern Barents Sea—despite the reduction in its longitudinal extent when comparing P2 to P1. In particular, the northern Barents Sea and the area near Novaya Zemlya, both know a significant decline in SIC, exhibit the highest increases in heat absorption, with linear trends reaching up to 45 W/m^2 per decade. In contrast, the central Barents Sea shows a weakening of heat absorption by up to 20 W/m^2 per decade.

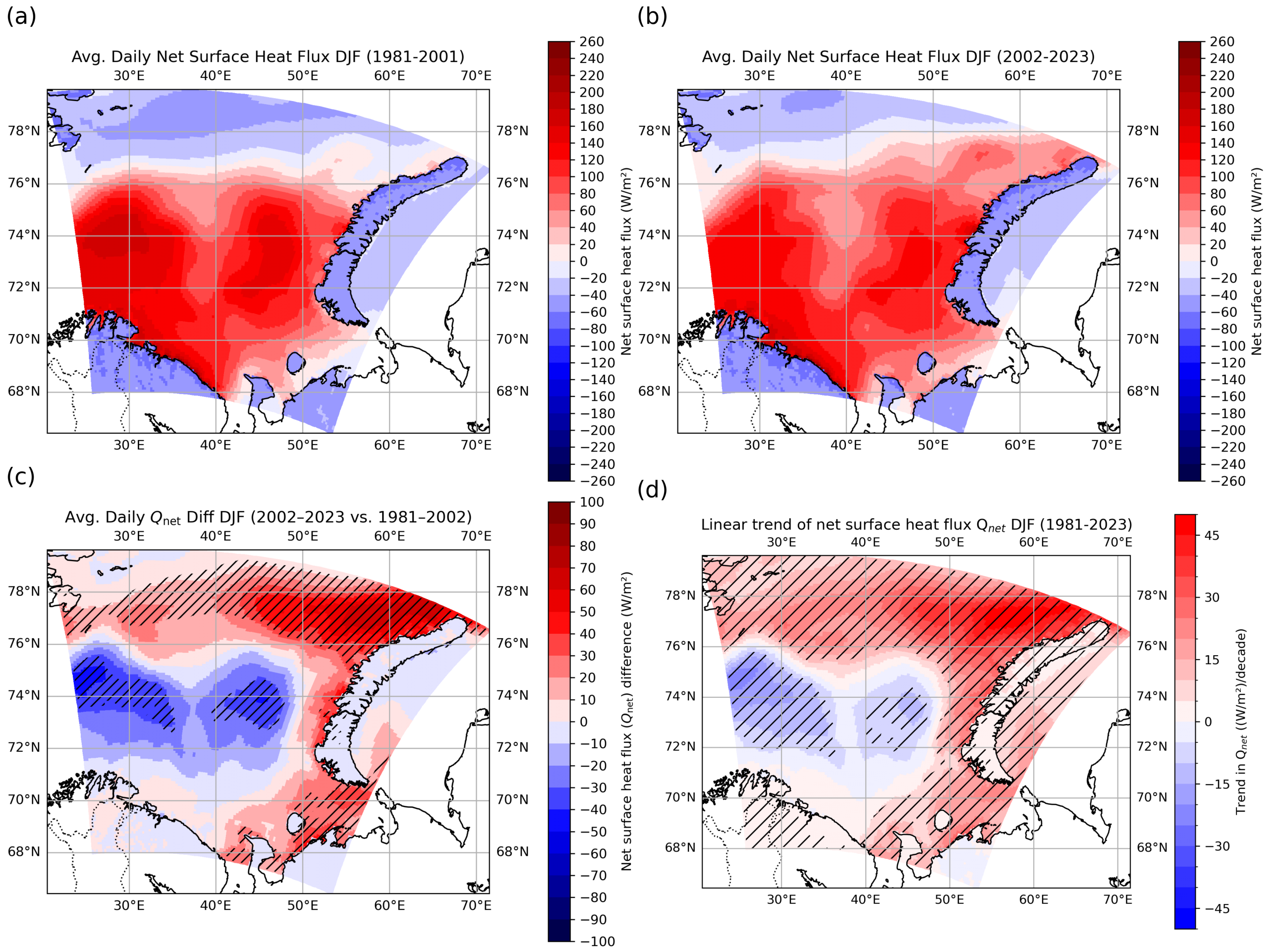

Figure 8: Mean daily net surface heat flux Q_{net} (W/m^2) for winter (DJF) for the periods 1981–2001 (a) and 2002–2023 (b), as well as the differences between the two periods (c) and its linear decadal trend value between 1981 and 2023 (d), based on model simulations (run1) using actual SST and SIC values from ERA5 reanalysis data. Significant differences, determined using a Student's t-test with a p-value of 0.05 or lower, are indicated by hatching.

3.2.3 10-meter wind speed (U10)

Figure 9 presents the mean daily wind speeds and directions during the winter months for P1 (a), P2 (b), the difference between P2 and P1 (c), and the linear decadal trend since 1981 for average wind speed (d), as well as the zonal (east–west) wind component (e) and the meridional (north–south) component (f), based on MAR model output for run1. Strong wind speeds of up to 7 m/s are observed along the northwestern coastline of Novaya Zemlya. As a mountainous region, Novaya Zemlya appears to have its windward side on the west, facing the Barents Sea and the strongest winds, while the leeward side lies to the east, facing the Kara Sea.

Differences in wind speed between P1 and P2 are generally small and not statistically significant, except in the Barents Sea southeast of Svalbard, where wind speeds have decreased by approximately

1.5 m/s. Slight increases are also seen along the northern Novaya Zemlya coast and around 50°E, 69°N in the southeastern Barents Sea. These are not significant in the direct P2–P1 comparison (c) but become significant when examining the linear trend (d).

However, wind directions, which are defined as the direction from which the wind originates, appear to have changed. The general wind patterns in panels (a) and (b) indicate a cyclonic circulation over the Barents Sea, which corresponds to a counterclockwise rotation around a low-pressure system in the Northern Hemisphere, due to the Coriolis effect deflecting winds to the right (NOAA, n.d.-a). The difference in wind direction in panel (c) seems to show that around western Novaya Zemlya, winds have shifted more towards the northwestward direction (i.e., shifting toward the northwest, originating from the southeast), potentially enhancing offshore sea ice drift. This is supported by the zonal wind trends shown in (e): a significant negative trend in the zonal component along the northern Barents Sea side of Novaya Zemlya indicates strengthening westerly winds (i.e., blowing toward the east, from the west). Simultaneously, the meridional component in (f) shows a significant positive trend across most of the Barents Sea, except in the southwest, indicating an increase in southerly (northward-blowing) winds. Together, these trends suggest potential enhanced wind-driven sea ice drift away from Novaya Zemlya toward the east.

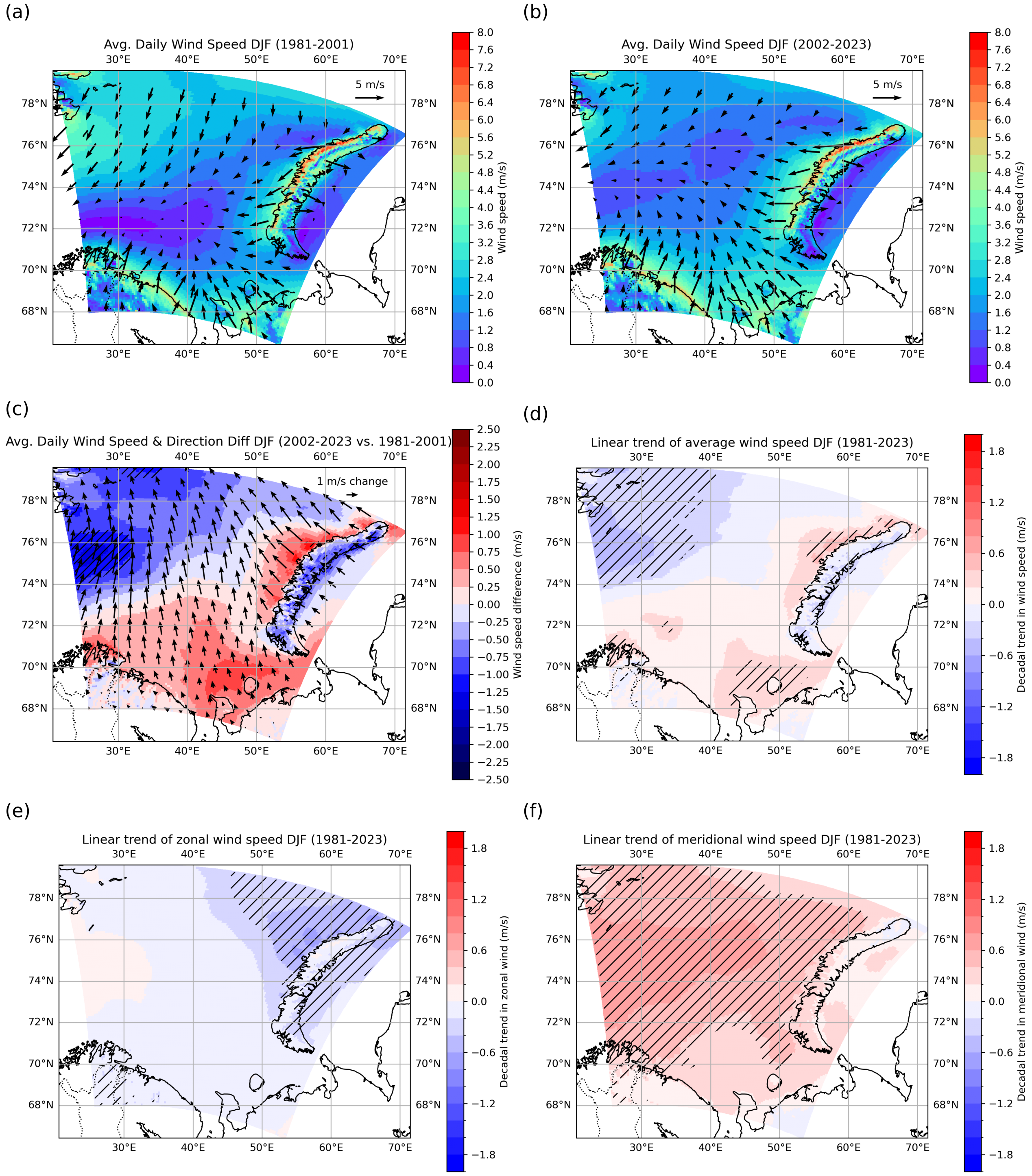

Figure 9: Mean daily 10-meter wind speed and direction (m/s) for winter (DJF) for the periods 1981–2001 (a) and 2002–2023 (b), as well as the differences between the two periods (c) and its linear decadal trend value between 1981 and 2023 for average wind speed (d), the zonal wind speed component (e) and the meridional wind speed component (f), based on model simulations (run1) using actual SST and SIC values from ERA5 reanalysis data. Significant differences, determined using a Student's t-test with a p-value of 0.05 or lower, are indicated by hatching.

3.2.4 Cloudiness (CD)

For cloudiness, only low-level clouds up to 2,000m altitude are considered. Figure 10 presents the mean daily low-level cloud cover during the winter months for P1 (a), P2 (b), the difference between P2 and P1 (c), and the linear decadal trend since 1981 (d), based on MAR model output for run1. The region is generally quite cloudy in DJF, with typical values ranging from 65% to 95%. The highest cloud cover is found in the northern central Barents Sea in both P1 and P2.

However, when comparing P2 to P1, a slight decrease in cloudiness is observed across a large part of the Barents Sea (except for the southern Barents Sea), with absolute reductions of about 5–10 percentage points. This corresponds to a statistically significant decreasing trend of approximately –0.03 percentage points per decade (or less). In contrast, above Novaya Zemlya, a slight increase in low-level cloud cover is seen, though this difference is not statistically significant.

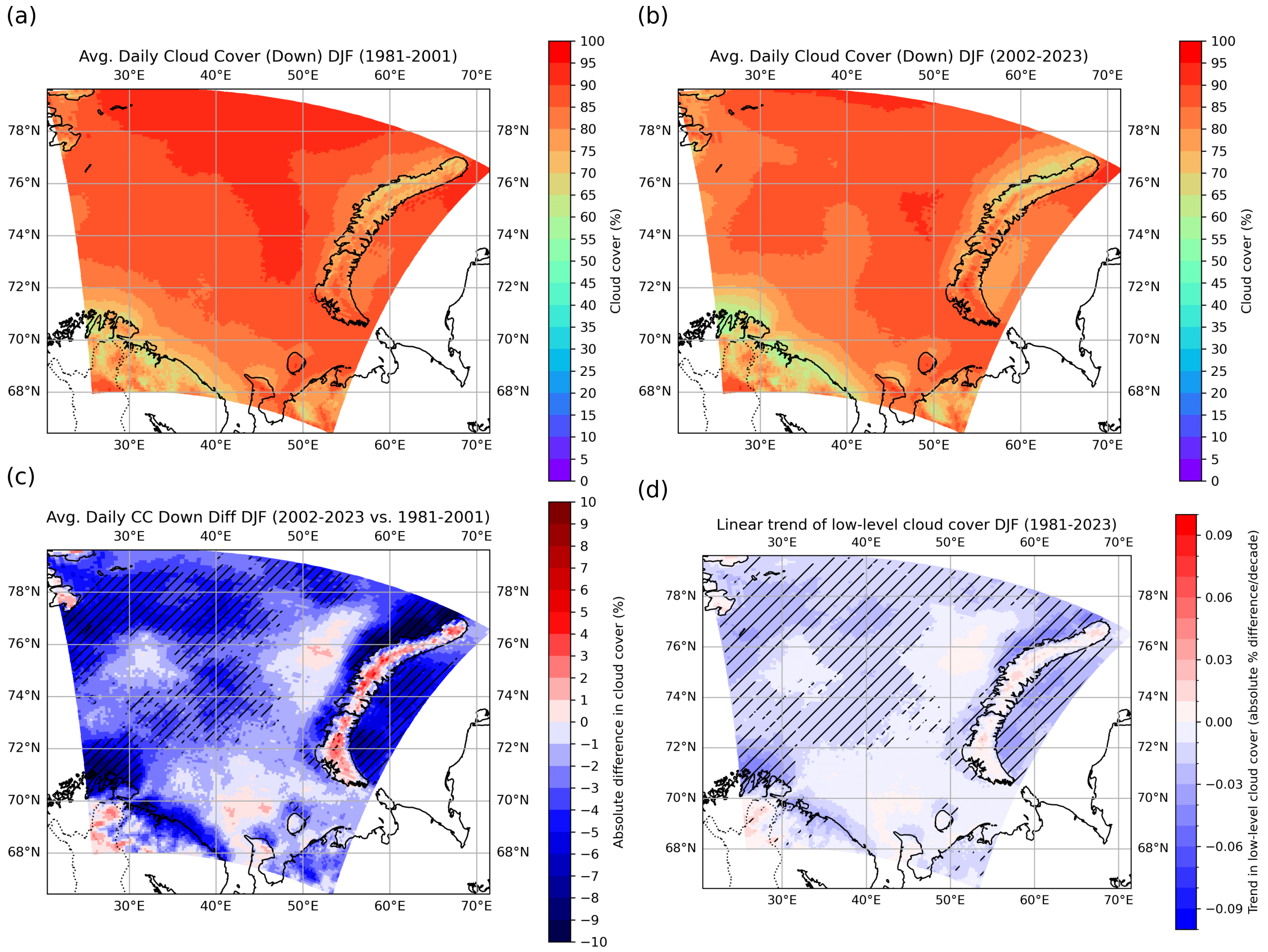

Figure 10: Mean daily low-level cloud cover (%) for winter (DJF) for the periods 1981–2001 (a) and 2002–2023 (b), as well as the differences between the two periods (c) and its linear decadal trend value between 1981 and 2023 (d), based on model simulations (run1) using actual SST and SIC values from ERA5 reanalysis data. Significant differences, determined using a Student's t-test with a p-value of 0.05 or lower, are indicated by hatching.

3.2.5 Surface mass balance (SMB)

Figure 11 presents the mean daily SMB, expressed in millimeters water equivalent per day (mmWE/day), during the winter months for P1 (a), P2 (b), the difference between P2 and P1 (c), and the linear decadal trend since 1981 (d), based on MAR model output for run1 for the ice sheet area, which is situated in northern Novaya Zemlya. Panels (c) and (d) show significant increases in SMB by 0.10-0.30 mmWE/day per decade for ice sheet area north of 74°N. This increase is likely due to higher snowfall in P2 compared to P1 (not shown). In contrast, during the summer months (see Appendix A.3), much stronger glacier mass losses are observed comparing P2 and P1, with significant SMB difference values reaching -3 mmWE/day or lower (Figure A.3.37o).

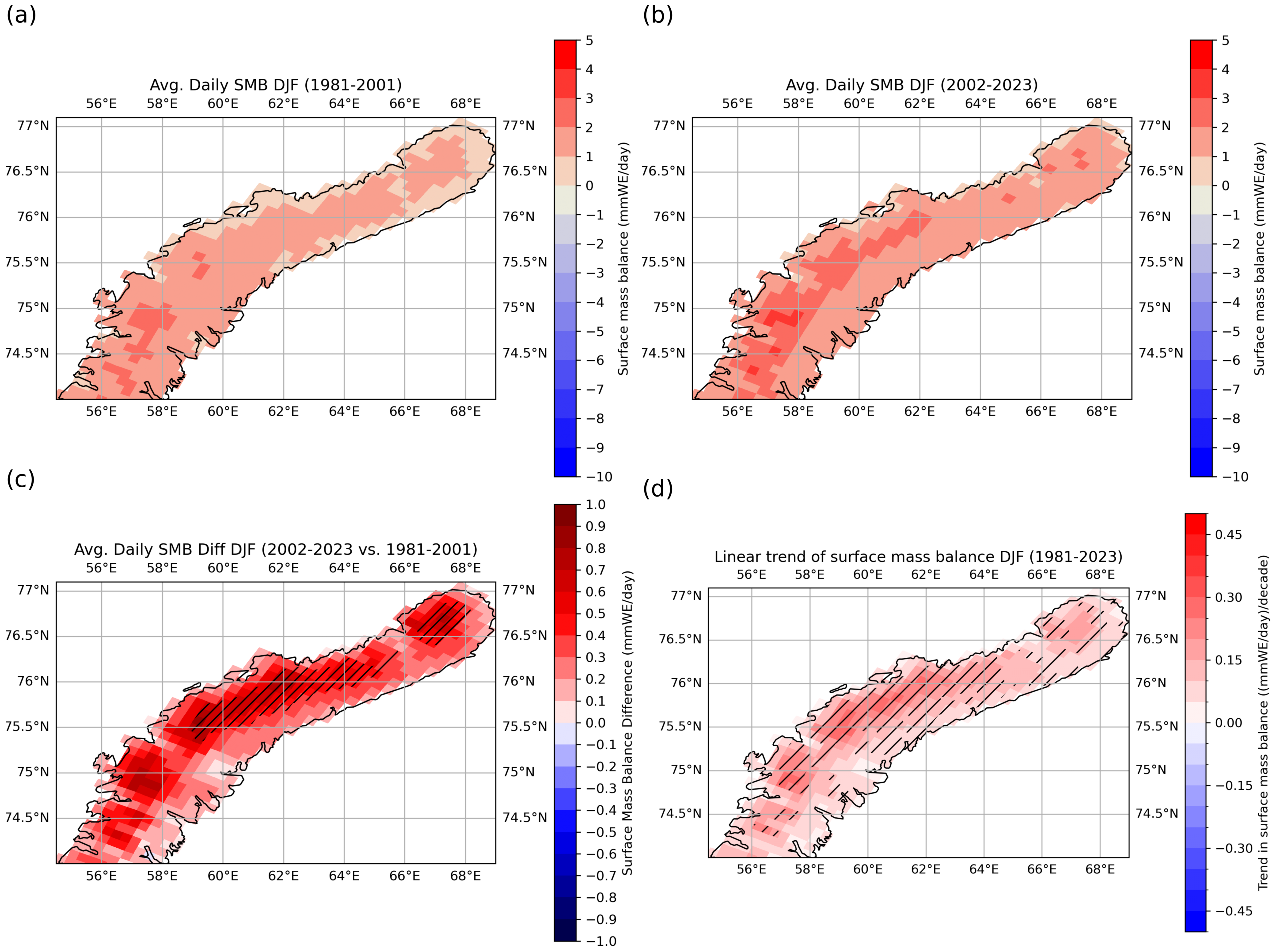

Figure 11: Mean daily SMB (mmWE/day) in northern Novaya Zemlya for winter (DJF) for the periods 1981–2001 (a) and 2002–2023 (b), as well as the differences between the two periods (c) and its linear decadal trend value between 1981 and 2023 (d), based on model simulations (run1) using actual SST and SIC values from ERA5 reanalysis data. Significant differences, determined using a Student's t-test with a p-value of 0.05 or lower, are indicated by hatching.

3.3 Comparison of climate variables between two model runs

Figure 12 presents the differences in DJF averages for P2, as simulated by run1 and run2, for T2M (a), Q_{net} (b), wind speed and direction (c), cloud cover (d), and SMB (e). These differences are solely due to variations in SIC and skin temperature, and thereby illustrate the impact of a warming Barents Sea and declining SIC. For all variables, positive differences are shown in red and negative differences in blue. A positive value indicates that run1 simulated higher values than run2. In other words, the variable increases under reduced SIC and elevated skin temperatures.

T2M: A general increase in T2M is observed across the Barents Sea–Novaya Zemlya region. However, only the differences in the northeastern Barents Sea, ranging from +3°C to +5°C, are statistically significant and can be attributed to changes in SIC and skin temperature.

$Q_{\mathbf{net}}$: All differences are positive as well, particularly in the northern and eastern Barents Sea, including areas just offshore from the Novaya Zemlya coast and north of eastern Russia. In these regions, the differences between both model runs are statistically significant, reaching up to +100 W/m^2. More heat is absorbed in run1 compared to run2, likely due to differences in SIE and open water areas. During the summer months (JJA), different subregions are affected, as shown in Appendix A.3, Figure A.3.38. In that season, the differences are generally limited to +20 W/m^2, with significant changes mainly occurring in the southern and western Barents Sea.

Wind speed and direction: No statistically significant changes in average wind speed are detected between both model runs. Nonetheless, there appears to be a weakening of wind by about 1 m/s in the eastern Barents Sea, while the lee side of Novaya Zemlya shows a slight increase of similar magnitude. In both DJF simulations (run1 and run2, P2), sea ice tends to drift away from Novaya Zemlya.

Cloud cover: Differences in cloud cover are predominantly negative, with absolute values up to -10%, indicating a notable decrease across much of the Barents Sea — especially in the northern part and a central zone. Above Novaya Zemlya, changes in cloud cover are positive in the north, though these are not statistically significant.

SMB: Finally, SMB differences are generally positive, but are only significant in some inland areas, suggesting that glacier accumulation in run1 is possibly (indirectly) influenced by reduced SIC and higher skin temperatures. In contrast, run2 P2 shows almost no difference compared to run1 P1, which is likely due to variations in snowfall (not shown).

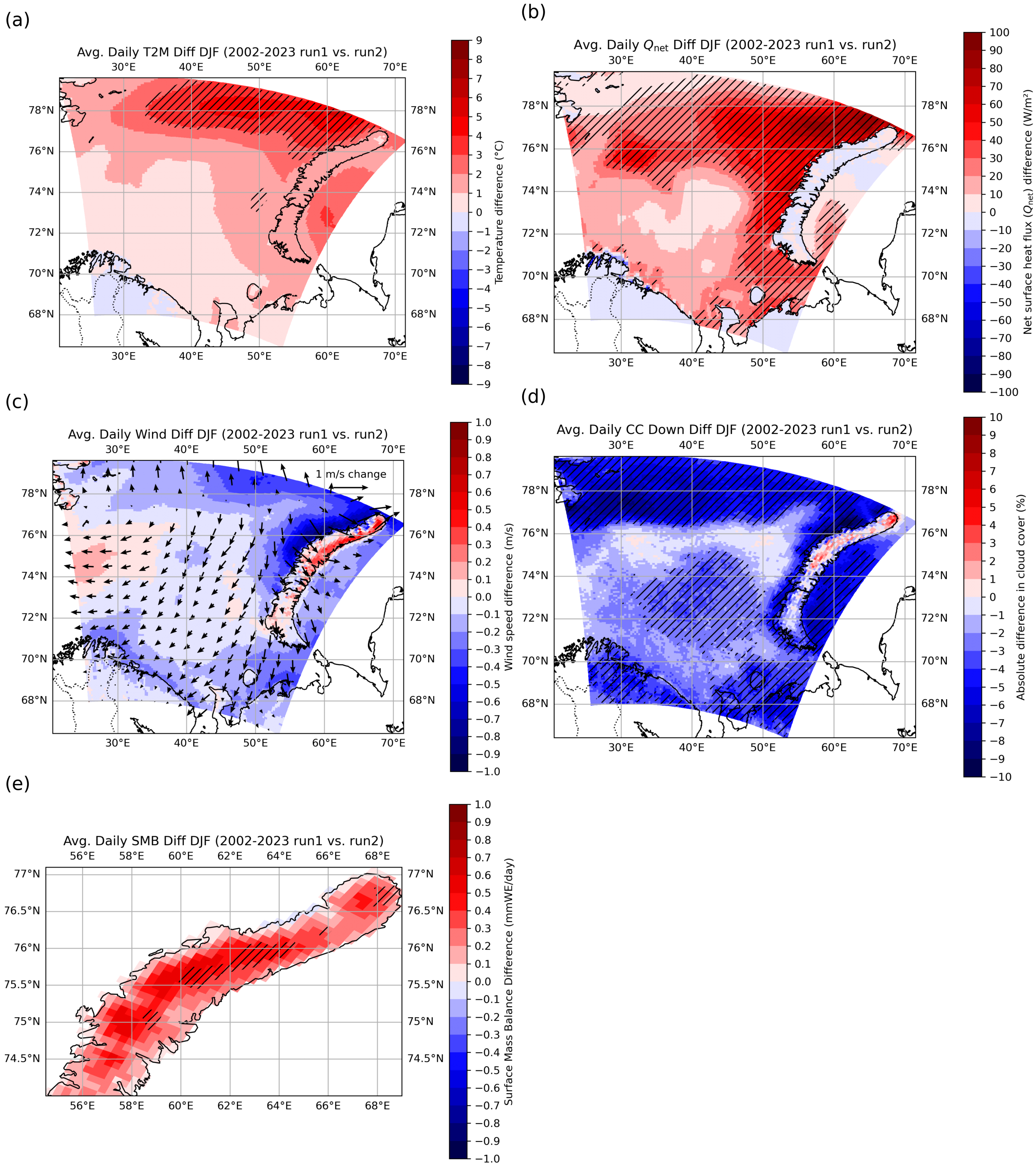

Figure 12: Differences in mean daily T2M (°C) (a), net surface heat flux (W/m^2) (b), 10-meter wind speed and direction (m/s) (c), low-level cloud cover (%) (d) and SMB (mmWE/day) (e) for winter (DJF) during the period 2002–2023, comparing two model simulations run1 vs. run2 with different SIC/SST values. Significant differences ($p < 0.05$) according to the Student's t-test are indicated by hatching.

3.4 Correlation between SIC and climate variables

This section presents Pearson's correlation coefficients between SIC and the selected variables in the ocean areas that were at least partially sea ice covered during DJF 1981–2023 (Figure 13). Since SMB contains values only over land, no correlation plot is shown for this variable.

T2M (panel a): The correlation coefficients are negative throughout the study area, with the most negative and significant values located in the northern Barents Sea and in regions that experienced the greatest decrease in sea ice. In the northern Barents Sea, a linear relationship appears to exist between SIC and T2M: as T2M increases, SIC decreases.

$\boldsymbol{Q}_{\mathbf{net}}$ (panel b): The sign of the correlation coefficient varies across the Barents Sea: it is positive in the central part and negative in the northern and southern regions. However, only the negative correlation coefficients in the northern Barents Sea, where SIC has declined the most, are significant, suggesting a linear relationship between Q_{net} and SIC in this region during DJF. When SIC declines, the area transitions to open water and consequently absorbs more heat. In contrast, in the central part, where SIC was already low or absent, ocean temperatures have been rising, reducing the ocean's heat absorption efficiency. This results in positive, though not significant, correlation coefficients.

Wind speed and direction: Correlation coefficients between total 10-meter wind speed and SIC (panel c) vary but are mostly negative. This indicates that wind speeds tend to increase as sea ice declines, consistent with the trends presented earlier. However, this correlation is only significant in a small area between 75°N and 76.5°N along the Novaya Zemlya coast. Overall, this suggests that there is unlikely to be a direct linear relationship between SIC and wind speed over the entire period, implying that the relationship is either non-existent, indirect, or more complex.

Regarding U10 (panel d), correlation coefficients are generally positive, except south of Novaya Zemlya. The northwesternmost part of the Barents Sea, north of 75°N, shows significant positive correlations, suggesting that in this area, declining SIC is associated with stronger easterlies (blowing from east to west), possibly contributing to sea ice drift.

For V10 (panel e), correlation coefficients are negative in the northern, central, and southern Barents Sea, and positive in the eastern Barents Sea. However, only the area near the Novaya Zemlya coast between 75°N and 76.5°N shows significant values. This implies that, in this local area, SIC decline is associated with stronger southerly winds (blowing from south to north).

Cloud cover (panel f): Correlation coefficients between SIC and cloud cover are generally negative and non-significant offshore, except in the northern Barents Sea. However, the coast of Novaya Zemlya north of 75°N and areas of the northern Barents Sea exhibit significant positive correlations, suggesting that cloud cover decreases alongside declining SIC in this region. When separating the time series into two periods (P1 and P2), significant negative correlation coefficients appear over larger areas of the central Barents Sea during P1 (not shown). In P2, the correlation becomes positive, indicating that declining SIC is associated with increased low-level cloud cover, as seen in the trend figures, although it is no longer significant (not shown).

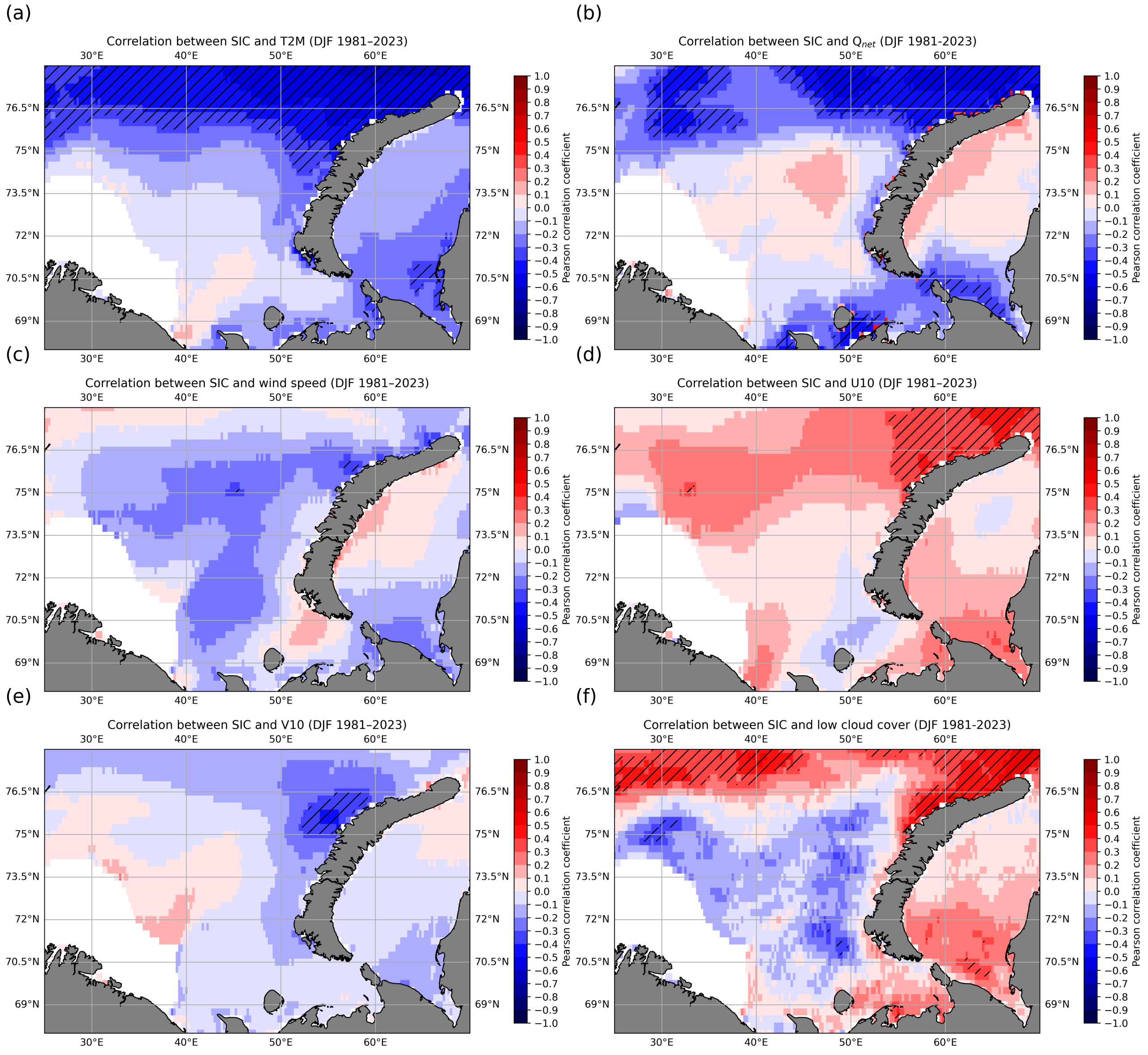

Figure 13: Pearson correlation coefficients between SIC from ERA5 and selected MAR variables during DJF 1981-2023: (a) 2-meter air temperature (T2M), (b) net surface heat flux (Q_{net}), (c) average 10-meter wind speed, (d) zonal wind speed (U10), (e) meridional wind speed (V10), and (f) low-level cloud cover (CD). Positive correlations are shown in red, and negative correlations in blue. Statistically significant correlations, determined using the scipy.stats.pearsonr function in Python, are hatched where $p < 0.05$, allowing us to reject the null hypothesis that there is no linear relationship between the two variables.

3.5 Time series of three selected coordinates

Based on the correlation coefficient analysis in the previous section, it becomes evident that most significant DJF correlations between atmospheric variables and SIC occur in the northern Barents Sea, particularly in the eastern part bordering Novaya Zemlya. However, moving westward away from Novaya Zemlya, the correlations tend to become less significant for some variables.

To better understand the processes occurring in this region, three coordinates were selected, as shown in Figure 14, for which time series of all variables are shown in Figure 15. These points are located further offshore in the northern Barents Sea (point 1: 50°E, 76.5°N), in the northern Barents Sea near the Novaya Zemlya coast (point 2: 60°E, 76.5°N), and further south near the Novaya Zemlya coast (point 3: 50°E, 72°N). Each of these points had more than 15% SIC, i.e. the sea ice edge, during the DJF P1, but in P2, all experienced a decline in SIC. Nevertheless, SIC remained around 15% at point 1, above 15% at point 2, and fell below 15% at point 3. The time series results, along with their SIC correlation values from the previous section, are presented.

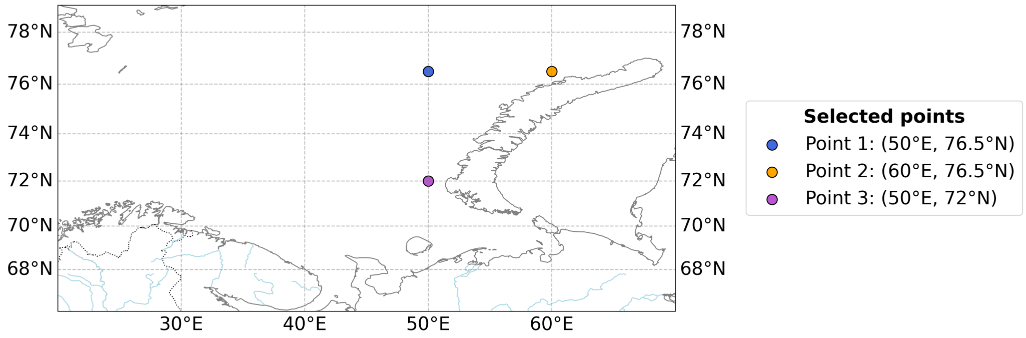

Figure 14: Map with three selected pixels for time series analysis (point 1: 50°E, 76.5°N, point 2: 60°E, 76.5°E, point 3: 50°E, 72°).

By 2023, the three selected coordinates had nearly reached 0% SIC, reflecting a strong decline since DJF 1981. Specifically, SIC decreased by 18.93% per decade at point 1, 21.14% per decade at point 2, and 7.01% per decade at point 3 (panel a).

At point 1 and 2, correlation coefficients between SIC and both T2M and Q_{net} were significant. These locations experienced pronounced warming trends of +3.06°C/decade and +2.72°C/decade (panel b), along with strong increases in Q_{net}: +18.05 W/m^2/decade and +24.09 W/m^2/decade, respectively (panel c). In contrast, at point 3, correlations with SIC were not significant, and the trends were smaller: +1.51°C/decade for T2M and +5.26 W/m^2/decade for Q_{net}.

For U10, significant positive correlations with SIC were observed at point 2, near the northern Novaya Zemlya coast. At point 1, correlation coefficients were between 0.2 and 0.3 but not statistically significant. At point 3, correlations were slightly negative, between 0 and -0.1. Despite the differences in correlation strength, U10 trends were negative at all three points (panel d), ranging from -0.12 m/s/decade in the southern Barents Sea (point 3) to -0.60 m/s/decade (point 2). This suggests that easterly winds, i.e. blowing from the east to the west, may contribute to SIC decline near the Novaya Zemlya coast but likely play a lesser role further offshore and in the southern Barents Sea.

For V10 (panel e), the spatial differences were less distinct. All three locations showed negative trends: -0.64 m/s/decade at point 1, -0.59 m/s/decade at point 2, and -0.50 m/s/decade at point 3. None of these trends were associated with significant correlations, although correlation coefficients in the northern Barents Sea ranged between -0.2 and -0.3. These values are close to areas where significant relationships were observed, suggesting that SIC may be influenced by meridional winds in a small part of the northern Barents Sea. However, the effects are likely non-linear and influenced by other interacting factors.

Finally, CD showed a significant positive correlation with SIC only at point 2, while the other two points had correlation coefficients closer to zero. This pattern is reflected in the CD trends (panel f), where DJF CD decreased by 3.26% per decade at point 2. This implies that more solar radiation reached the surface in that region, which may partly explain the significant CD-SIC correlation.

When considering all variables over the 1981-2023 timeline, the periods 2001–2005 and 2006–2010 stand out due to marked fluctuations. During 2001–2005, T2M appears to increase more rapidly than in earlier years, while U10 also shows a more abrupt decrease. This coincides with an initial sharp drop in SIC around 2001–2005. After a short period of relative stabilization, the years 2006–2010 exhibit an even more pronounced rise in T2M, reaching values up to approximately -5°C, and a further decline in U10, reaching negative values as low as -8 m/s. During this period, V10 also increases more rapidly, reaching up to around 3.5 m/s, and at point 2, CD even falls below 50% during one winter. This interval also marks the first time SIC values approach nearly 0% at the three studied coordinates, after which DJF sea ice continues to struggle in subsequent years. Particularly at the northern Barents Sea locations, 2006–2010 also appears to coincide with the most rapid increase in Q_{net}.

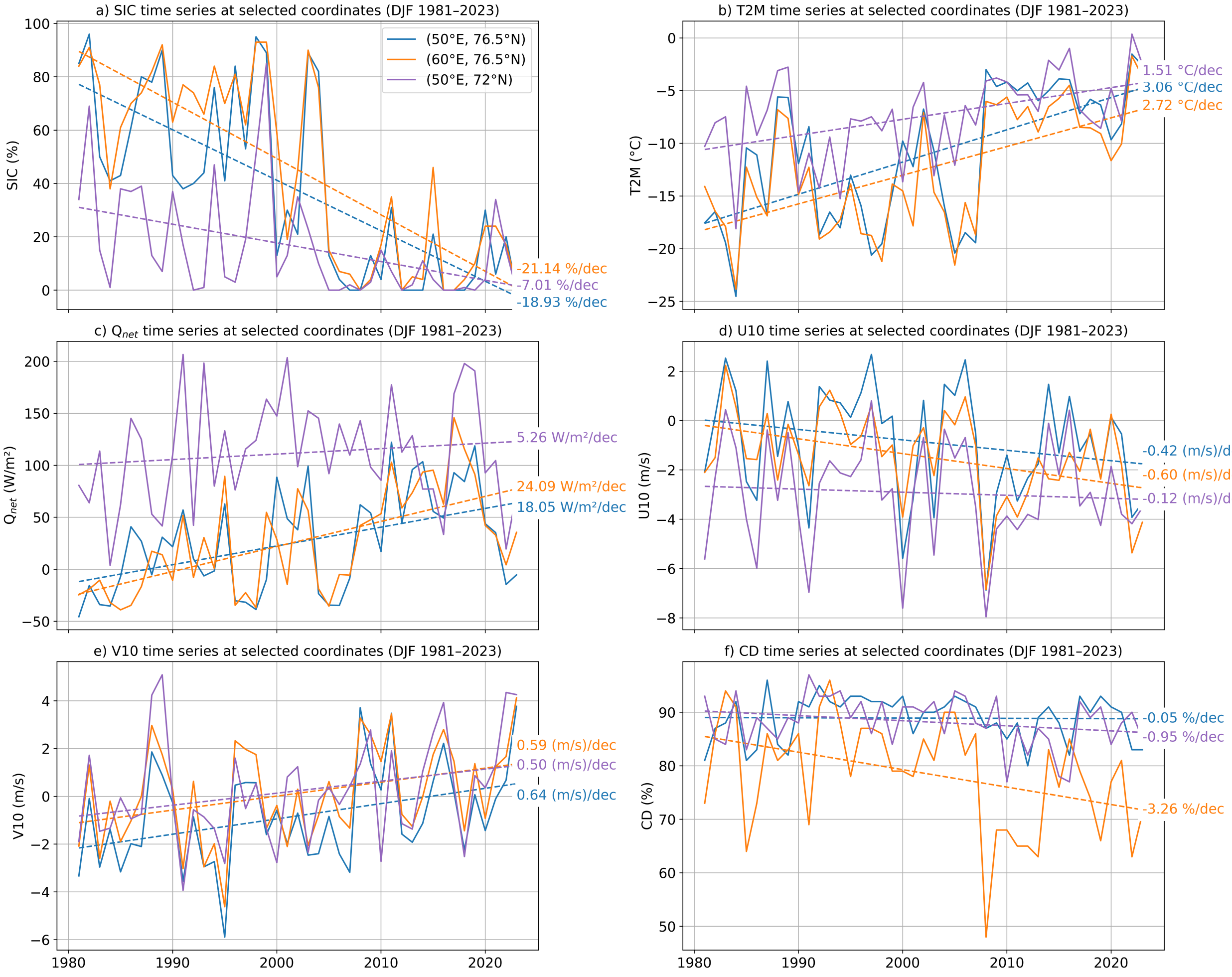

Figure 15: Time series of three selected coordinates, point 1 (50°E, 76.5°N), point 2 (60°E, 76.5°N), point 3 (50°E, 72°N) and for SIC (a), T2M (b), Q_{net},(c), U10 (d), V10 (e), CD (f) for DJF 1981-2023.

4 Discussion

In this study, the aim is to reconstruct how climate and atmospheric variables in the Barents Sea–Novaya Zemlya region have evolved during winter, by comparing the periods before and after a climate shift that occurred in 2000–2001. This shift was driven by rising SST and a rapid decline in SIC in the Barents Sea. The study also aims to identify links between these variables and SIC. In this section, the interpretations of the key results and potential links derived from them are presented first. Then, the limitations of the study's methodology are discussed.

4.1 Links between climate and atmospheric variables and SIC

This section interprets the main results and patterns. Across the Barents Sea, the results showed that the northern part, the formerly perennial ice region, has experienced the most significant warming (Kumar et al., 2021). As a result, areas with multi-year sea ice (ice that survives the summer months) have also been affected. This warming leads to thinner ice and, combined with rising SST, delays sea ice formation in the Barents Sea due to its connection to the Atlantic Ocean (Serreze & Meier, 2019).

4.1.1 Role of changing atmospheric circulation in sea ice drift

In the study region, a low-pressure system is generally present, characterized by counterclockwise winds, contributing to the atmospheric dynamics. Westerlies are dominant in the Kara Sea, while easterlies prevail in the Barents Sea due to the cyclonic activity there (Haacker et al., 2024). Consequently, the Kara Sea, lying on the leeward side, typically experiences colder temperatures and therefore retains more sea ice, whereas the Barents Sea remains warmer. As global temperatures change, pressure systems also change. This can cause winds in the Barents Sea to deviate more strongly towards the west and north, resulting in increased sea ice drift. However, the general circulation in the free atmosphere is entirely forced by the lateral boundaries, which are the same in both MAR simulations. The only differences we might observe are changes in the local circulation within the boundary layer. However, since the integration domain remains relatively small, much of the variability in the near-surface wind simulated by MAR is still influenced by the lateral boundaries (particularly surface pressure), preventing MAR from simulating a fully distinct near-surface circulation.

For instance, strong southeasterly winds from Novaya Zemlya have been identified as a driver for the formation of larger polynyas, i.e., open water areas surrounded by sea ice, in the Barents Sea (Moore, 2013). These polynyas form when sea ice is pushed away by strong winds. New sea ice can only form if the ocean's surface loses heat to the atmosphere (Serreze & Barry, 2014). However, with rising SST, once the existing ice is displaced, no new ice forms due to insufficient ocean-atmosphere heat loss (Petoukhov & Semenov, 2010).

4.1.2 Warm Atlantic water inflow reinforces sea ice melt

In fact, increased heat transport through the Barents Sea Opening has been linked to accelerated sea ice melt (Docquier et al., 2020). In recent decades, a larger volume of Atlantic water has flowed into the Barents Sea through this opening, facilitating the northward expansion of Atlantic waters into the Arctic (Muilwijk et al., 2018). This inflow raises SST, which reduces the ocean's heat absorption capacity and hinders sea ice formation (Dörr et al., 2024).

Therefore, there is clearly a correlation between warmer Atlantic water and declining SIC. The influx of warmer Atlantic water reinforces sea ice melt (Armstrong McKay et al., 2022). Nevertheless, our figures seem to indicate that the initial ice melt is primarily due to rising air temperatures and stronger winds because of changing pressure levels, especially in the northern Barents Sea, primarily near the coast of Novaya Zemlya and extending somewhat further offshore in line with Pavlova et al., 2014. There, T2M have risen, sea ice has melted and weakened, and zonal winds have intensified, pushing the ice offshore toward warmer Atlantic waters. Once this initial combination of higher air temperatures and changing wind directions occurred, some areas experienced increased solar radiation due to reduced cloud cover. This further warmed the ocean, decreased SIE, and created a positive feedback loop reinforcing SIC loss.

These changes, in combination with enhanced Atlantic heat transport, prevent sea ice recovery (Mohamed et al., 2022b). Thus, sea ice loss appears to be more a consequence than a cause of changes in atmospheric and climatic parameters, specifically stronger zonal wind speeds and warmer air temperatures, and is also influenced by interactions with warmer ocean waters.

4.1.3 Regional differences in heat uptake and sea ice decline in the Barents Sea

In zones that transitioned from being ice-covered to being ice-free, heat absorption increases due to the absence of reflective ice, resulting in higher net heat flux (Q_{net}). However, where open water was already present, the ocean absorbed heat less efficiently as SST rose. This raises concerns about the Arctic's diminishing role as a heat sink (Deser et al., 2015). Further south of Novaya Zemlya, relationships between SIC and atmospheric/oceanic variables seem to be less direct. Although no strong linear correlations were found, run1 still indicates a trend of rising air temperatures and lower cloud cover, contributing to increasing SST and sea ice melt. In this case, the Atlantic inflow may have amplified rather than initiated the decline.

A comparison of P2 in run1 and run2 reveals that in the southeastern Barents Sea, differences emerged in wind direction, Q_{net}, and cloud cover. Significantly higher air temperatures were only observed in the northern Barents Sea. The greater heat absorption in run1 (higher Q_{net}) suggests higher SST in run1 P2 compared to run2 P2. This supports the idea that Atlantic inflow either reached further or became warmer in run1. Thus, the warmer Atlantic water played a reinforcing role in the second rapid SIC decline, preventing recovery to initial levels. As SST rise, ocean heat uptake becomes less efficient, reducing the Arctic's capacity as a heat sink (Deser et al., 2015).

4.1.4 Impact on Novaya's Zemlya's SMB

Finally, SMB may also be affected. In DJF, the the SMB remains positive due to additional snowfall, as temperatures, although increasing, remain below freezing (Boisvert & Stroeve, 2015).

4.1.5 Seasonal differences: a brief summer vs. winter comparison

Although the main focus of this master's thesis is on the winter (DJF) evolution, a brief comparison with the summer season (JJA) may offer additional insights. The full set of JJA figures is provided in Appendix A.3; for run1, see Figure A.3.37.

During JJA, T2M rose significantly across the entire study area, except for Novaya Zemlya despite the significant changes in the southernmost parts, consistent with Beck et al., 2018. However, the magnitude of warming was lower than that observed in DJF. In some restricted areas, such as areas in the western, central, and southeastern Barents Sea, significantly more heat was absorbed in P2 compared to P1. Yet in most regions, there were no significant differences in heat uptake, despite widespread T2M increases. This could suggest that the ocean's heat sink efficiency has reached a limit, reducing its ability to buffer further climate warming (Deser et al., 2015).

Wind speeds in summer are generally lower than in winter, with the strongest winds occurring over the mountainous regions in northern Novaya Zemlya. However, significant changes in wind speeds between P1 and P2 were only found in the northwestern Barents Sea, near Svalbard. In contrast, cloud cover during JJA decreased significantly only in the southeastern Barents Sea. During DJF, this decrease occurred over a much larger area, particularly in the northern half.

SMB also declined significantly during JJA, indicating glacier retreat in central and northern Novaya Zemlya by 3 mmWE/day or more, especially along the Barents Sea coastline, in line with R. Carr et al., 2023.

In JJA run2 (Figure A.3.38), significant differences between both model runs for P2 mainly affected T2M, Q_{net}, and cloud cover, although cloud cover did not change significantly in the northern central Barents Sea. These findings suggest that, in summer, winds and atmospheric circulation likely played a smaller role in SIC decline than in winter. Instead, increasing air temperatures and reduced cloud cover, which allowed more incoming solar radiation, played a more dominant role. This aligns with the increase in marine heat wave occurrences in the Barents Sea during summer since 1982 (Mohamed et al., 2022a). Regarding reduced cloud cover, this was especially the case in the southeastern Barents Sea, where up to 10 percent absolute decrease in cloud cover was simulated. Without the reflective effect of sea ice that was still present in P1, more radiation is now absorbed by the ocean, reinforcing warming and SIC loss. This aligns with the southeastern Barents Sea's high interannual variability (Mohamed et al., 2022b).

In conclusion, while sea ice decline in winter appears to be mainly driven by changes in atmospheric circulation, with reinforcing interactions involving warm Atlantic water, summer changes seem more closely related to rising air temperatures and the inflow of Atlantic water (Pavlova et al., 2014).

4.2 Limitations

This section discusses study limitations and suggests improvements for future research.

The main limitation is the failure to account for ocean–atmosphere interactions, as MAR is not coupled with an ocean model. Even if MAR simulates different near-surface climate conditions, these do not influence the ocean or variables such as sea ice thickness (SIT), for example.

For instance, this study focuses on SIC but does not delve into details regarding SIT. SIT is not provided by ERA5 and is therefore fixed in the MAR simulation at 55 cm of ice plus the accumulated snowpack simulated by MAR. However, since sea ice is not advected in MAR, snow cover results only from local winter snowfall, whereas in reality, the snowpack over sea ice may originate from other regions. It is important to note that snow has an insulating effect on sea ice, SIT affects the transmittance of radiative energy, and fresh snow increases albedo (Petrich & Eicken, 2010). Figure A.4.39 and its description in Appendix A.4 show in more detail the changes in SIT between the data that were available for P1 and P2, where it can be observed that changes vary from one place to another, as well as DJF sea ice drifting northward and westward between 1993 and 2001. As the aim of both MAR and ERA5 is to simulate the surface and atmosphere, SIT is fixed in both models impacting model results above sea ice. Uhlíková et al. (2024) argue that such assumptions in ERA5 primarily affect the accuracy of turbulent fluxes, namely SHF and LHF. These fluxes were compared to values from the Climate Forecast System Reanalysis (CFSR) by the National Centers for Environmental Prediction (NCEP), which incorporates more accurate SIT and snow depth data. As a result, turbulent fluxes in CFSR were found to be more sensitive to changes in SIC for the reasons mentioned above. However, this dataset is only available up to 2011 and therefore does not cover the full period of our study. The only way to obtain a realistic SIT is to couple MAR with an ocean–sea ice model like NEMO-S3, which can advect sea ice and simulate its growth and melt.

Lastly, a more comprehensive interpretation could have been achieved by analyzing the total heat budget, rather than focusing solely on Q_{net}, as was done in this study. The total heat budget ocean transport processes, i.e. advection. While Q_{net} provides insight into whether the ocean is gaining or losing heat to the atmosphere, it does not account for internal oceanic processes. In contrast, changes in the total heat budget directly reflect variations in ocean temperature (Qiao et al., 2025). Therefore, incorporating ocean circulation data would have been beneficial to better quantify heat transport processes and, in turn, improve the understanding of the connection with rising ocean temperatures.

5 Conclusion and perspectives

In this master's thesis, the climate of one of the most rapidly changing regions in the Arctic, the Barents Sea and Novaya Zemlya region, and its link to sea ice decline during the winter months since 1981 was investigated using simulations from the regional climate model MAR.

As shown in the validation section, MAR performs well in comparison to available observations, although it still slightly underestimates winter air temperatures. Consequently, the model's results are useful for comparing the period before and after a major climate shift, as well as for comparing different scenarios of SIC and SST in the Barents Sea.

The main findings suggest that during winter, changes in atmospheric circulation and specifically stronger southeasterly winds along the Barents Sea coast of the northern part of Novaya Zemlya have contributed to sea ice drift. In combination with higher air and water temperatures, driven in part by increased solar radiation due to reduced cloud cover in some areas, these factors have inhibited sea ice formation, following a significant climate shift after 2001. In other words, once the decline in SIC was initiated by changes in wind direction and warmer air temperatures, the northern Barents Sea absorbed more heat, a process that was partly amplified by decreased cloud cover.

This study is limited by the lack of ocean-atmosphere interactions and ocean circulation data, which prevents a proper estimation of the advection component of the heat budget and makes it difficult to accurately simulate changes in water temperature. Moreover, a more detailed analysis of SIT would have improved the accuracy of the radiation-related components of the model, as thinning rates directly affect these processes. Future research could focus on coupling MAR with an ocean model to enhance the quality and realism of the simulations.

Despite these limitations, the region's sparse observational coverage highlights the urgent need for more data in this rapidly evolving environment. This study emphasizes the vulnerability of this Arctic region, where SIC is rapidly declining, and illustrates how various climate factors are interconnected. It underlines the importance of continued research, given the role this region may play in regulating heat absorption and thus its potential contribution to mitigating global warming.

References

Ali, A., Dunlop, P., Coleman, S., Kerr, D., McNabb, R. W., & Noormets, R. (2023). Glacier area changes in Novaya Zemlya from 1986–89 to 2019–21 using object-based image analysis in Google Earth Engine. *Journal of Glaciology*, *69*(277), 1305–1316. https://doi.org/10.1017/jog.2023.18

Armstrong McKay, D. I., Staal, A., Abrams, J. F., Winkelmann, R., Sakschewski, B., Loriani, S., Fetzer, I., Cornell, S. E., Rockström, J., & Lenton, T. M. (2022). Exceeding 1.5 °C global warming could trigger multiple climate tipping points. *Science*, *377*(6611), eabn7950. https://doi.org/10.1126/science.abn7950

Årthun, M., Eldevik, T., Smedsrud, L. H., Skagseth, Ø., & Ingvaldsen, R. B. (2012). Quantifying the influence of Atlantic heat on Barents sea ice variability and retreat. *Journal of Climate*, *25*(13), 4736–4743. https://doi.org/10.1175/JCLI-D-11-00466.1

Barton, B. I., Lenn, Y.-D., & Lique, C. (2018). Observed atlantification of the Barents Sea causes the polar front to limit the expansion of winter sea ice. *Journal of Physical Oceanography*, *48*(8), 1849–1866. https://doi.org/10.1175/JPO-D-18-0003.1

Beck, H. E., Zimmermann, N. E., McVicar, T. R., Vergopolan, N., Berg, A., & Wood, E. F. (2018). Present and future Köppen-Geiger climate classification maps at 1-km resolution. *Scientific Data*, *5*(1), 180214. https://doi.org/10.1038/sdata.2018.214

Boeke, R. C., & Taylor, P. C. (2018). Seasonal energy exchange in sea ice retreat regions contributes to differences in projected Arctic warming. *Nature Communications*, *9*(1), 5017. https://doi.org/10.1038/s41467-018-07061-9

Boisvert, L. N., & Stroeve, J. C. (2015). The Arctic is becoming warmer and wetter as revealed by the Atmospheric Infrared Sounder. *Geophysical Research Letters*, *42*(11), 4439–4446. https://doi.org/10.1002/2015GL063775

Britannica. (2024). North pole. Retrieved October 28, 2024, from https://www.britannica.com/place/North-Pole

Bromwich, D. H., Wilson, A. B., Bai, L., Liu, Z., Barlage, M., Shih, C.-F., Maldonado, S., Hines, K. M., Wang, S.-H., Woollen, J., Kuo, B., Lin, H.-C., Wee, T.-K., Serreze, M. C., & Walsh, J. E. (2018). The Arctic System Reanalysis, Version 2. *Bulletin of the American Meteorological Society*, *99*(4), 805–828. https://doi.org/10.1175/BAMS-D-16-0215.1

Carr, J. R., Bell, H., Killick, R., & Holt, T. (2017). Exceptional retreat of Novaya Zemlya's marine-terminating outlet glaciers between 2000 and 2013. *The Cryosphere*, *11*(5), 2149–2174. https://doi.org/10.5194/tc-11-2149-2017

Carr, J. R., Stokes, C., & Vieli, A. (2014). Recent retreat of major outlet glaciers on Novaya Zemlya, Russian Arctic, influenced by fjord geometry and sea-ice conditions. *Journal of Glaciology*, *60*(219), 155–170. https://doi.org/10.3189/2014JoG13J122

Carr, R., Murphy, Z., Nienow, P., Jakob, L., & Gourmelen, N. (2023). Rapid and synchronous response of outlet glaciers to ocean warming on the Barents Sea coast, Novaya Zemlya. *Journal of Glaciology*, 1–17. https://doi.org/10.1017/jog.2023.104

Chapman, W. L., & Walsh, J. E. (2007). Simulations of Arctic temperature and pressure by global coupled models. *Journal of Climate*, *20*(4), 609–632. https://doi.org/10.1175/JCLI4026.1

Climateurope. (n.d.). Earth system modeling, a definition. Retrieved October 9, 2024, from https://www.climateurope.eu/earth-system-modeling-a-definition/

Cohen, J., Zhang, X., Francis, J., Jung, T., Kwok, R., Overland, J., Ballinger, T. J., Bhatt, U. S., Chen, H. W., Coumou, D., Feldstein, S., Gu, H., Handorf, D., Henderson, G., Ionita, M., Kretschmer, M., Laliberte, F., Lee, S., Linderholm, H. W., . . . Yoon, J. (2020). Divergent consensuses on Arctic amplification influence on midlatitude severe winter weather. *Nature Climate Change*, *10*(1), 20–29. https://doi.org/10.1038/s41558-019-0662-y

Comiso, J. C., Parkinson, C. L., Gersten, R., & Stock, L. (2008). Accelerated decline in the Arctic sea ice cover. *Geophysical Research Letters*, *35*(1), 2007GL031972. https://doi.org/10.1029/2007GL031972

Copernicus Climate Change Service. (2023). ERA5 hourly data on single levels from 1940 to present. https://doi.org/10.24381/CDS.ADBB2D47

Deser, C., Tomas, R. A., & Sun, L. (2015). The role of ocean–atmosphere coupling in the zonal-mean atmospheric response to Arctic sea ice loss. *Journal of Climate*, *28*(6), 2168–2186. https://doi.org/10.1175/JCLI-D-14-00325.1

Ding, Q., Wallace, J. M., Battisti, D. S., Steig, E. J., Gallant, A. J. E., Kim, H.-J., & Geng, L. (2014). Tropical forcing of the recent rapid Arctic warming in northeastern Canada and Greenland. *Nature*, *509*(7499), 209–212. https://doi.org/10.1038/nature13260

Docquier, D., Fuentes-Franco, R., Koenigk, T., & Fichefet, T. (2020). Sea ice—ocean interactions in the Barents Sea modeled at different resolutions. *Frontiers in Earth Science*, *8*, 172. https://doi.org/10.3389/feart.2020.00172

Donlon, C. J., Minnett, P. J., Gentemann, C., Nightingale, T. J., Barton, I. J., Ward, B., & Murray, M. J. (2002). Toward improved validation of satellite sea surface skin temperature measurements for climate research. *Journal of Climate*, *15*(4), 353–369. https://doi.org/10.1175/1520-0442(2002)015<0353:TIVOSS>2.0.CO;2

Dörr, J., Årthun, M., Docquier, D., Li, C., & Eldevik, T. (2024). Causal links between sea-ice variability in the Barents-Kara seas and oceanic and atmospheric drivers [Publisher: American Geophysical Union (AGU)]. *Geophysical Research Letters*, *51*(7). https://doi.org/10.1029/2024gl108195

Döscher, R., Vihma, T., & Maksimovich, E. (2014). Recent advances in understanding the arctic climate system state and change from a sea ice perspective: A review. *Atmospheric Chemistry and Physics*, *14*(24), 13571–13600. https://doi.org/10.5194/acp-14-13571-2014

Doutreloup, S., Wyard, C., Amory, C., Kittel, C., Erpicum, M., & Fettweis, X. (2019). Sensitivity to convective schemes on precipitation simulated by the regional climate model mar over belgium (1987–2017). *Atmosphere*, *10*(1), 34. https://doi.org/10.3390/atmos10010034

Eisenman, I., Untersteiner, N., & Wettlaufer, J. S. (2007). On the reliability of simulated Arctic sea ice in global climate models. *Geophysical Research Letters*, *34*(10), 2007GL029914. https://doi.org/10.1029/2007GL029914

E.U. Copernicus Marine Service Information. (2023). Global ocean physics reanalysis. Retrieved April 3, 2025, from https://doi.org/10.48670/moi-00021

Fettweis, X., Box, J. E., Agosta, C., Amory, C., Kittel, C., Lang, C., Van As, D., Machguth, H., & Gallée, H. (2017). Reconstructions of the 1900–2015 greenland ice sheet surface mass balance using the regional climate mar model. *The Cryosphere*, *11*(2), 1015–1033. https://doi.org/10.5194/tc-11-1015-2017

Fettweis, X., Gallée, H., Lefebre, F., & van Ypersele, J.-P. (2005). Greenland surface mass balance simulated by a regional climate model and comparison with satellite-derived data in 1990–1991. *Climate Dynamics*, *24*, 623–640. https://doi.org/10.1007/s00382-005-0010-y

Flato, G., Marotzke, J., Abiodun, B., Braconnot, P., Chou, S. C., Collins, W., Cox, P., Driouech, F., Emori, S., Eyring, V., et al. (2014). Evaluation of climate models. In *Climate change 2013: The physical science basis. contribution of working group i to the fifth assessment report of the intergovernmental panel on climate change* (pp. 741–866). Cambridge University Press.

Gallée, H., Moufouma-Okia, W., Bechtold, P., Brasseur, O., Dupays, I., Marbaix, P., Messager, C., Ramel, R., & Lebel, T. (2004). A high-resolution simulation of a West African rainy season using a regional climate model. *Journal of Geophysical Research: Atmospheres*, *109*(D5). https://doi.org/10.1029/2003JD004020

Gallée, H., Fontaine de Ghélin, O., & van den Broeke, M. R. (1995). Simulation of atmospheric circulation during the gimex 91 experiment using a meso-γ primitive equations model. *Journal of climate*, *8*(11), 2843–2859. https://doi.org/10.1175/1520-0442(1995)008<2843:SOACDT>2.0.CO;2

Gallée, H., & Schayes, G. (1994). Development of a three-dimensional meso-γ primitive equation model: Katabatic winds simulation in the area of Terra Nova Bay, Antarctica. *Monthly Weather Review*, *122*(4), 671–685. https://doi.org/10.1175/1520-0493(1994)122<0671:DOATDM>2.0.CO;2

Gandoin, R., & Garza, J. (2024). Underestimation of strong wind speeds offshore in era5: Evidence, discussion and correction. *Wind Energy Science*, *9*(8), 1727–1745. https://doi.org/10.5194/wes-9-1727-2024

Gerland, S., Ingvaldsen, R. B., Reigstad, M., Sundfjord, A., Bogstad, B., Chierici, M., Hop, H., Renaud, P. E., Smedsrud, L. H., Stige, L. C., et al. (2023). Still Arctic?—The changing Barents Sea. *Elem Sci Anth*, *11*(1), 00088. https://doi.org/10.1525/elementa.2022.00088

Graillet, J.-F. (2022). Optimizing NESTOR, a tool for preparing meteorological and surface data for the MAR model. Retrieved March 18, 2025, from https://matheo.uliege.be/bitstream/2268.2/14780/4/JFGrailet_TFE_NESTOR.pdf

Grant, K. L., Stokes, C. R., & Evans, I. S. (2009). Identification and characteristics of surge-type glaciers on Novaya Zemlya, Russian Arctic [Publisher: International Glaciological Society]. *Journal of Glaciology*, *55*(194), 960–972. https://doi.org/10.3189/002214309790794940

Haacker, J., Wouters, B., Fettweis, X., Glissenaar, I. A., & Box, J. E. (2024). Atmospheric-river-induced foehn events drain glaciers on Novaya Zemlya. *Nature Communications*, *15*(1), 7021. https://doi.org/10.1038/s41467-024-51404-8

Hanna, E., Cappelen, J., Fettweis, X., Mernild, S. H., Mote, T. L., Mottram, R., Steffen, K., Ballinger, T. J., & Hall, R. J. (2020). Greenland surface air temperature changes from 1981 to 2019 and implications for ice-sheet melt and mass-balance change. *International Journal of Climatology*, *41*, E1336–E1352. https://doi.org//doi.org/10.1002/joc.6771

Hock, R., & Huss, M. (2021). Glaciers and climate change. In *Climate Change* (pp. 157–176). Elsevier. https://doi.org/10.1016/B978-0-12-821575-3.00009-8

Huang, J., Zhang, X., Zhang, Q., Lin, Y., Hao, M., Luo, Y., Zhao, Z., Yao, Y., Chen, X., Wang, L., Nie, S., Yin, Y., Xu, Y., & Zhang, J. (2017). Recently amplified Arctic warming has contributed to a continual global warming trend. *Nature Climate Change*, *7*(12), 875–879. https://doi.org/10.1038/s41558-017-0009-5

Jakob, L., & Gourmelen, N. (2023). Glacier mass loss between 2010 and 2020 dominated by atmospheric forcing. *Geophysical Research Letters*, *50*(8), e2023GL102954. https://doi.org/10.1029/2023GL102954

Jakowczyk, M., & Stramska, M. (2014). Spatial and temporal variability of satellite-derived sea surface temperature in the Barents Sea. *International Journal of Remote Sensing*, *35*(17), 6545–6560. https://doi.org/10.1080/01431161.2014.958247

Jiawei, Z. (2025). Comparison of six regridding algorithms. Retrieved March 23, 2025, from https://xesmf.readthedocs.io/en/latest/notebooks/Compare_algorithms.html

King, M. D., Howat, I. M., Candela, S. G., Noh, M. J., Jeong, S., Noël, B. P. Y., Van Den Broeke, M. R., Wouters, B., & Negrete, A. (2020). Dynamic ice loss from the Greenland Ice Sheet driven by sustained glacier retreat. *Communications Earth & Environment*, *1*(1), 1. https://doi.org/10.1038/s43247-020-0001-2

Kittel, C., Amory, C., Agosta, C., Jourdain, N. C., Hofer, S., Delhasse, A., Doutreloup, S., Huot, P.-V., Lang, C., Fichefet, T., et al. (2021). Diverging future surface mass balance between the Antarctic ice shelves and grounded ice sheet. *The Cryosphere*, *15*, 1215–1236. https://doi.org/10.5194/tc-15-1215-2021

Kochtitzky, W., & Copland, L. (2022). Retreat of Northern Hemisphere marine-terminating glaciers, 2000–2020. *Geophysical Research Letters*, *49*(3), e2021GL096501. https://doi.org/10.1029/2021GL096501

Kohnemann, S. H. E., Heinemann, G., Bromwich, D. H., & Gutjahr, O. (2017). Extreme warming in the Kara Sea and Barents Sea during the winter period 2000–16. *Journal of Climate*, *30*(22), 8913–8927. https://doi.org/10.1175/JCLI-D-16-0693.1

Kumar, A., Yadav, J., & Mohan, R. (2021). Spatio-temporal change and variability of Barents-Kara sea ice, in the Arctic: Ocean and atmospheric implications. *Science of The Total Environment*, *753*, 142046. https://doi.org/10.1016/j.scitotenv.2020.142046

Lebrun, M., Vancoppenolle, M., Madec, G., & Massonnet, F. (2019). Arctic sea-ice-free season projected to extend into autumn. *The Cryosphere*, *13*(1), 79–96. https://doi.org/10.5194/tc-13-79-2019

Lee, H., Calvin, K., Dasgupta, D., Krinner, G., Mukherji, A., Thorne, P., Trisos, C., Romero, J., Aldunce, P., Barret, K., et al. (2023). Climate change 2023: Synthesis report, summary for policymakers. contribution of working groups I, II and III to the Sixth Assessment Report of the Intergovernmental Panel on Climate Change. *Intergovernmental Panel on Climate Change*. https://doi.org/10.59327/IPCC/AR6-9789291691647.001

Leung, L. R. (2012). Regional climate models. In R. A. Meyers (Ed.), *Encyclopedia of sustainability science and technology* (pp. 8902–8919). Springer New York. https://doi.org/10.1007/978-1-4419-0851-3_363

Li, X., Tan, Z., Zheng, Y., Bushuk, M., & Donner, L. J. (2023). Open water in sea ice causes high bias in polar low-level clouds in GFDL CM4. *Geophysical Research Letters*, *50*(24), e2023GL106322. https://doi.org/10.1029/2023GL106322

Lien, V. S., Schlichtholz, P., Skagseth, Ø., & Vikebø, F. B. (2017). Wind-driven Atlantic water flow as a direct mode for reduced Barents sea ice cover. *Journal of Climate*, *30*(2), 803–812. https://doi.org/10.1175/JCLI-D-16-0025.1

Ma, W., Wang, H., Chen, G., Leung, L. R., Lu, J., Rasch, P. J., Fu, Q., Kravitz, B., Zou, Y., Cassano, J. J., & Maslowski, W. (2024). The role of interdecadal climate oscillations in driving Arctic atmospheric river trends. *Nature Communications*, *15*(1), 2135. https://doi.org/10.1038/s41467-024-45159-5

Marbaix, P., Gallée, H., Brasseur, O., & van Ypersele, J.-P. (2003). Lateral boundary conditions in regional climate models: A detailed study of the relaxation procedure. *Monthly weather review*, *131*(3), 461–479. https://doi.org/10.1175/1520-0493(2003)131<0461:LBCIRC>2.0.CO;2

Maslanik, J. A., Fowler, C., Stroeve, J., Drobot, S., Zwally, J., Yi, D., & Emery, W. (2007). A younger, thinner Arctic ice cover: Increased potential for rapid, extensive sea-ice loss. *Geophysical Research Letters*, *34*(24), 2007GL032043. https://doi.org/10.1029/2007GL032043

McGuire, A. D., Chapin, F., Walsh, J. E., & Wirth, C. (2006). Integrated regional changes in Arctic climate feedbacks: Implications for the global climate system. *Annual Review of Environment and Resources*, *31*(1), 61–91. https://doi.org/10.1146/annurev.energy.31.020105.100253

McPhee, M. (2008). *Air-ice-ocean interaction*. Springer New York. https://doi.org/10.1007/978-0-387-78335-2

Melkonian, A. K., Willis, M. J., Pritchard, M. E., & Stewart, A. J. (2016). Recent changes in glacier velocities and thinning at Novaya Zemlya. *Remote Sensing of Environment*, *174*, 244–257. https://doi.org/10.1016/j.rse.2015.11.001

Mishra, P., Pandey, C. M., Singh, U., Gupta, A., Sahu, C., & Keshri, A. (2019). Descriptive statistics and normality tests for statistical data. *Annals of cardiac anaesthesia*, *22*(1), 67–72. https://doi.org/10.4103/aca.ACA_157_18

Mohamed, B., Nilsen, F., & Skogseth, R. (2022a). Marine heatwaves characteristics in the Barents Sea based on high resolution satellite data (1982–2020). *Frontiers in Marine Science*, *9*, 821646. https://doi.org/10.3389/fmars.2022.821646

Mohamed, B., Nilsen, F., & Skogseth, R. (2022b). Interannual and decadal variability of sea surface temperature and sea ice concentration in the Barents Sea. *Remote Sensing*, *14*(17), 4413. https://doi.org/10.3390/rs14174413

Moore, G. (2013). The Novaya Zemlya bora and its impact on Barents Sea air-sea interaction. *Geophysical research letters*, *40*(13), 3462–3467. https://doi.org/10.1002/grl.50641

Morcrette, J.-J. (2002). The surface downward longwave radiation in the ECMWF forecast system. *Journal of climate*, *15*(14), 1875–1892. https://doi.org/10.1175/1520-0442(2002)015<1875:TSDLRI>2.0.CO;2

Mouginot, J., Rignot, E., Bjørk, A. A., Van Den Broeke, M., Millan, R., Morlighem, M., Noël, B., Scheuchl, B., & Wood, M. (2019). Forty-six years of Greenland Ice Sheet mass balance from 1972 to 2018. *Proceedings of the National Academy of Sciences*, *116*(19), 9239–9244. https://doi.org/10.1073/pnas.1904242116

Muilwijk, M., Smedsrud, L. H., Ilicak, M., & Drange, H. (2018). Atlantic water heat transport variability in the 20th century arctic ocean from a global ocean model and observations. *Journal of Geophysical Research: Oceans*, *123*(11), 8159–8179. https://doi.org/10.1029/2018JC014327

NASA/LARC/SD/ASDC. (2025). CERES and GEO-enhanced TOA, within-atmosphere and surface fluxes, clouds and aerosols daily Terra-Aqua edition4a [data set]. Retrieved March 20, 2025, from https://doi.org/10.5067/Terra+Aqua/CERES/SYN1degDay_L3.004A

National Snow and Ice Data Center. (2024). Quick facts about sea ice. Retrieved December 8, 2024, from https://nsidc.org/learn/parts-cryosphere/sea-ice/quick-facts-about-sea-ice

NCCS. (2025). Seklima - observations and weather statistics [data set]. Retrieved March 20, 2025, from https://seklima.met.no/observations/

NOAA. (n.d.-a). The coriolis effect. Retrieved April 6, 2025, from https://doi.org/10.48670/moi-00021

NOAA. (n.d.-b). Data visualization and analysis. Retrieved May 28, 2025, from https://ferret.pmel.noaa.gov/Ferret/

NOAA. (2023). The four core types of clouds. Retrieved March 24, 2025, from https://www.noaa.gov/jetstream/clouds/four-core-types-of-clouds

NOAA. (2024). What is ceres? Retrieved March 23, 2025, from https://ceres.larc.nasa.gov/

NOAA. (2025). Global surface summary of the day - GSOD [data set]. Retrieved March 20, 2025, from https://www.ncei.noaa.gov/maps/daily/

Noël, B., Fettweis, X., Van De Berg, W. J., Van Den Broeke, M. R., & Erpicum, M. (2014). Sensitivity of Greenland Ice Sheet surface mass balance to perturbations in sea surface temperature and sea ice cover: A study with the regional climate model MAR. *The Cryosphere*, *8*(5), 1871–1883. https://doi.org/10.5194/tc-8-1871-2014

Notz, D., Haumann, F. A., Haak, H., Jungclaus, J. H., & Marotzke, J. (2013). Arctic sea-ice evolution as modeled by Max Planck Institute for meteorology's earth system model. *Journal of Advances in Modeling Earth Systems*, *5*(2), 173–194. https://doi.org/10.1002/jame.20016

NumPy team. (2025). The fundamental package for scientific computing with Python. Retrieved March 23, 2025, from https://numpy.org/

Onarheim, I. H., Eldevik, T., Årthun, M., Ingvaldsen, R. B., & Smedsrud, L. H. (2015). Skillful prediction of Barents Sea ice cover. *Geophysical Research Letters*, *42*(13), 5364–5371. https://doi.org/10.1002/2015GL064359

pandas via NumFOCUS. (2024). Pandas.dataframe.resample. Retrieved March 23, 2025, from https://pandas.pydata.org/docs/reference/api/pandas.DataFrame.resample.html#pandas.DataFrame.resample

Parkinson, C. L. (2014). Spatially mapped reductions in the length of the Arctic sea ice season. *Geophysical Research Letters*, *41*(12), 4316–4322. https://doi.org/10.1002/2014GL060434

Pavlova, O., Pavlov, V., & Gerland, S. (2014). The impact of winds and sea surface temperatures on the Barents Sea ice extent, a statistical approach. *Journal of Marine Systems*, *130*, 248–255. https://doi.org/10.1016/j.jmarsys.2013.02.011

Peel, M. C., Finlayson, B. L., & McMahon, T. A. (2007). Updated world map of the Köppen-Geiger climate classification. *Hydrology and Earth System Sciences*, *11*(5), 1633–1644. https://doi.org/10.5194/hess-11-1633-2007

Petoukhov, V., & Semenov, V. A. (2010). A link between reduced Barents-Kara sea ice and cold winter extremes over northern continents. *Journal of Geophysical Research: Atmospheres*, *115*(D21), 2009JD013568. https://doi.org/10.1029/2009JD013568

Petrich, C., & Eicken, H. (2010). Growth, structure and properties of sea ice. *Sea ice*, *2*, 23–77. https://doi.org/10.1002/9781444317145.ch2

Qiao, L., Tang, H., & Huang, G. (2025). Drivers and predictability of summer marine heatwaves in the northwest pacific. *Journal of Geophysical Research: Atmospheres*, *130*(6), e2024JD042994. https://doi.org/10.1029/2024JD042994

Rantanen, M., Karpechko, A. Y., Lipponen, A., Nordling, K., Hyvärinen, O., Ruosteenoja, K., Vihma, T., & Laaksonen, A. (2022). The Arctic has warmed nearly four times faster than the globe since 1979. *Communications Earth & Environment*, *3*(1), 168. https://doi.org/10.1038/s43247-022-00498-3

Ridder, K. D., & Schayes, G. (1997). The iagl land surface model. *Journal of applied meteorology*, *36*(2), 167–182. https://doi.org/10.1175/1520-0450(1997)036<0167:TILSM>2.0.CO;2

Serreze, M. C., & Barry, R. G. (2011). Processes and impacts of Arctic amplification: A research synthesis. *Global and Planetary Change*, *77*(1-2), 85–96. https://doi.org/10.1016/j.gloplacha.2011.03.004

Serreze, M. C., & Barry, R. G. (2014). *The Arctic climate system* (2nd ed.). Cambridge University Press. https://doi.org/10.1017/CBO9781139583817

Serreze, M. C., & Meier, W. N. (2019). The Arctic's sea ice cover: Trends, variability, predictability, and comparisons to the Antarctic. *Annals of the New York Academy of Sciences*, *1436*(1), 36–53. https://doi.org/10.1111/nyas.13856

Smedsrud, L. H., Esau, I., Ingvaldsen, R. B., Eldevik, T., Haugan, P. M., Li, C., Lien, V. S., Olsen, A., Omar, A. M., Otterå, O. H., Risebrobakken, B., Sandø, A. B., Semenov, V. A., & Sorokina, S. A. (2013). The role of the Barents Sea in the Arctic climate system. *Reviews of Geophysics*, *51*(3), 415–449. https://doi.org/10.1002/rog.20017

Sorteberg, A., & Kvingedal, B. (2006). Atmospheric forcing on the Barents Sea winter ice extent. *Journal of Climate*, *19*(19), 4772–4784. https://doi.org/10.1175/JCLI3885.1

Steele, M., Ermold, W., & Zhang, J. (2008). Arctic Ocean surface warming trends over the past 100 years. *Geophysical Research Letters*, *35*(2), 2007GL031651. https://doi.org/10.1029/2007GL031651

Stroeve, J. C., Mioduszewski, J. R., Rennermalm, A., Boisvert, L. N., Tedesco, M., & Robinson, D. (2017). Investigating the local-scale influence of sea ice on Greenland surface melt. *The Cryosphere*, *11*(5), 2363–2381. https://doi.org/10.5194/tc-11-2363-2017

Tapiador, F. J., Navarro, A., Moreno, R., Sánchez, J. L., & García-Ortega, E. (2020). Regional climate models: 30 years of dynamical downscaling. *Atmospheric Research*, *235*, 104785. https://doi.org/10.1016/j.atmosres.2019.104785

Taylor, P., Hegyi, B., Boeke, R., & Boisvert, L. (2018). On the increasing importance of air-sea exchanges in a thawing Arctic: A review. *Atmosphere*, *9*(2), 41. https://doi.org/10.3390/atmos9020041

Tepes, P., Nienow, P., & Gourmelen, N. (2021). Accelerating ice mass loss across Arctic Russia in response to atmospheric warming, sea ice decline, and Atlantification of the Eurasian Arctic shelf seas. *Journal of Geophysical Research: Earth Surface*, *126*(7), e2021JF006068. https://doi.org/10.1029/2021JF006068

The SciPy community. (2025). Statistical functions (scipy.stats). Retrieved April 9, 2025, from https://docs.scipy.org/doc/scipy/reference/stats.html

Uhlíková, T., Vihma, T., Karpechko, A. Y., & Uotila, P. (2024). Effects of Arctic sea-ice concentration on turbulent surface fluxes in four atmospheric reanalyses. *The Cryosphere*, *18*(2), 957–976. https://doi.org/10.5194/tc-18-957-2024

ULiège. (2023). Uliège Charter for the use of generative artificial intelligence in academic work. Retrieved April 6, 2025, from https://www.student.uliege.be/cms/c_19230399/en/uliege-charter-for-the-use-of-generative-artificial-intelligence-in-academic-work

Verezemskaya, P., Selivanova, Y., Tilinina, N., Markina, M., Krinitskiy, M., Sharmar, V., & Razorenova, O. (2022). Projected changes in the near-surface atmosphere over the Barents Sea based on CMIP5 scenarios. *Russian Journal of Earth Sciences*, 1–11. https://doi.org/10.2205/2021ES000770

Vihma, T. (2014). Effects of Arctic sea ice decline on weather and climate: A review. *Surveys in Geophysics*, *35*(5), 1175–1214. https://doi.org/10.1007/s10712-014-9284-0

A Appendix

A.1 NESTOR

In order to initialize the grid at the start of the simulation and assign values for boundary forcing from NetCDF files, MAR utilizes the NESTOR pre-processing software, which stands for *NESTing ORganization for the preparation of meteorological and surface fields in regional climate models* (Graillet, 2022). Its functionality is illustrated in the schematic shown in Figure 16.

Once NESTOR is configured correctly, as detailed in the next section, the MAR model can be launched. It is important to account for a spin-up time, the period required for the model simulations to become sufficiently independent of the initial conditions and produce reliable output. Therefore, simulations are initiated in September of the year preceding the actual study period. In our case, the simulations start in September 1979 for run1 and September 2000 for run2.

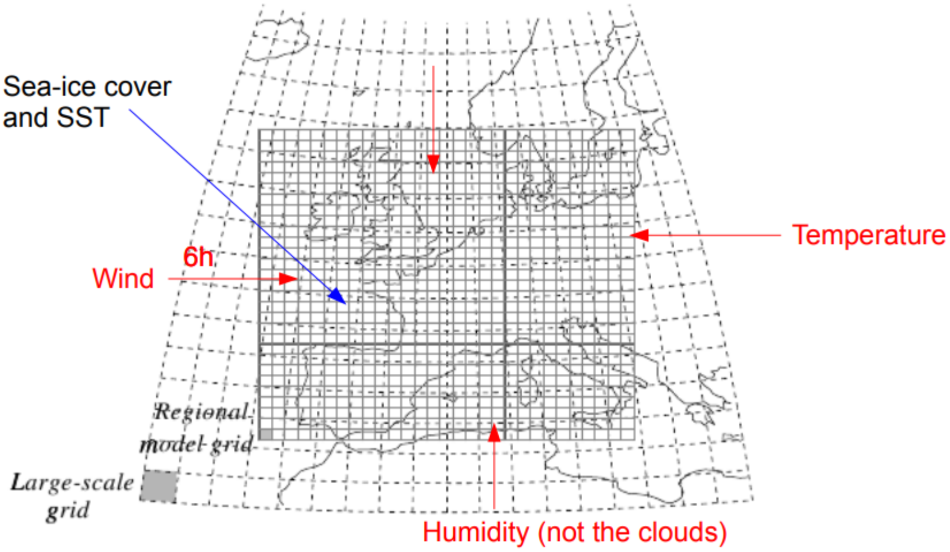

Figure 16: Schematic of NESTOR: Initial and boundary conditions are derived from a large-scale model, whose grid is downscaled to the regional MAR grid, creating a relaxation zone. Figure from Fettweis, X. (2024). Climate Modelling course, October 2024 (unpublished material).

A.1.1 Configuring NESTOR

After successfully installing MAR, specify the region in which your domain is situated in `~/MAR/bin/INI.ctr`. For this study, we select the polar regions by setting `"GR"`. Executing this file will generate the necessary links and directories required for further setup.

In `~/MAR/bin/NST.ctr`, the large-scale model ERA5 and the nested model MAR are specified.

A 6-hour time interval is set between the two forcings. The following settings are applied: Soil model: Ridder and Schayes (1997), Soil wetness: 60% in all layers, wind gust estimation: standard WGE method of Brasseur (2001), and topography source: ETOPO1 dataset (resolution: 1 minute).

The next step involves configuring NESTOR in the `$SCRATCH` directory. The full NESTOR code is accessible via GitLab with an account:
gitlab.com/Mar-Group/MARv3/-/tree/master/src/NESTOR/NESTOR.5.0.

In the `$SCRATCH` directory the `MARgrd.ctr` and `NSTdim.inc` are modified. First, the MAR grid's mesh size and domain center coordinates are specified in `MARgrd.ctr`. For this study, a 10-km resolution is used, with the MAR domain centered at longitude 33° and latitude 70.2°. Second, the file `NSTdim.inc` defines the grid dimensions. Here, a 160 × 170 pixel domain is selected, including a 15-pixel-wide relaxation zone on all sides. After removing this zone in the analysis part, the effective domain remains 120 × 130 pixels, ensuring the study area is still well represented.

For run1, the next step is compilation. For run2, however, the climatology values must be read correctly. Therefore, modifications are made in the `src` directory within the files `LSCvar.inc`, `NSTint.f`, and `NESTOR.f`. First, `LSCvar.inc` contains the shared variables, so new variables must be defined to store climatology values for each pixel for 365 time steps, corresponding to the number of days in a non-leap year. Second, in `NSTint.f`, since the climatology file provides daily values but 6-hourly output is required, linear interpolation is performed as illustrated in GitLab script 3. Third, `NESTOR.f` reads the climatology values in three dimensions (longitude, latitude, and time) but should save them in two dimensions (longitude and latitude).

NESTOR is then compiled using `./Compile.exe` and `./NESTOR.exe`. Next, the configuration files are copied to the appropriate directory, where they can be launched for the desired period using a bash script that executes the following commands:

- `NST $DOM $YYYY $MM`
- `qsub $HOME/MAR/sim/GRa/input/NESTOR/run/NST_GRa.$YY.$MM.*.cmd`

This process creates folders for all specified years. Finally, MAR is compiled using the command `CODE a01`, generating netCDF files with daily values for various variables, which will be used for further analysis.

A.2 Comparison of station observations, MAR and ERA5

Table 5: Comparison of station vs. ERA5 SLP and T2M metrics (DJF)

Station	SLP					T2M				
	R	MAE	Bias	RMSD	NSD	R	MAE	Bias	RMSD	NSD
Batsfjord	0.98	1.24	0.43	1.83	0.95	0.82	2.19	-2.08	2.43	1.20
Berlevag	0.98	1.23	0.15	2.06	0.93	0.89	3.12	-3.12	3.25	1.23
Bugrino	0.97	1.45	0.21	2.28	0.96	0.95	1.53	1.14	1.85	1.03
Cape Menshikova	1.00	0.44	0.07	0.55	0.99	0.98	0.74	0.55	1.08	0.95
Dalne Zelenetskaya	0.90	4.00	1.29	5.02	0.77	0.81	2.41	-1.62	3.04	0.71
Edgeøya	0.88	2.30	0.18	4.88	0.81	0.95	1.06	-0.22	1.57	0.93
Golitsino	0.87	3.01	0.54	5.65	0.75	0.75	3.07	2.24	4.33	0.55
Hopen Island	1.00	0.47	0.27	0.60	1.00	0.99	0.79	0.59	0.98	1.01
Kanin Nos	0.99	0.84	0.41	1.50	1.01	0.97	2.05	2.05	2.23	1.05
Kolguyev Island	0.91	2.70	1.78	4.06	0.90	0.94	1.96	-1.67	2.34	1.03
Kongsøya	1.00	0.43	0.37	0.54	1.00	0.98	1.13	0.94	1.33	0.96
Malye Karmakuly	1.00	0.81	0.76	1.03	1.01	0.99	1.83	-1.83	1.93	1.09
Mehamn	0.98	1.04	0.72	1.75	1.02	0.94	0.57	-0.41	0.76	1.17
Mys Zhelaniya	0.96	1.19	0.58	2.30	1.01	0.98	0.76	-0.46	1.15	1.00
Russkaya Gavan	0.99	0.84	0.66	1.56	0.98	0.98	1.91	-1.88	2.04	0.92
Slettnes Fyr	0.97	1.24	0.88	2.13	0.99	0.93	1.68	-1.62	1.87	1.24
Teriberka	0.98	1.07	-0.07	1.82	0.96	0.96	0.57	0.20	0.83	0.91
Tsyp Navolok	0.80	3.36	0.45	6.76	0.75	0.58	2.48	2.16	3.49	0.49
Vaida Guba Bay	0.97	1.24	-0.55	2.02	1.02	0.85	1.25	1.11	1.76	0.76

Table 6: Comparison of station vs. MAR metrics (all months) for SLP, T2M, and WDSP

Station	SLP					T2M					WDSP				
	R	MAE	Bias	RMSD	NSD	R	MAE	Bias	RMSD	NSD	R	MAE	Bias	RMSD	NSD
Batsfjord	0.97	1.07	0.56	1.96	0.91	0.98	2.48	-2.46	2.71	1.02	0.90	1.56	1.55	1.74	1.12
Berlevag	0.97	0.99	0.08	1.91	0.93	0.99	3.60	-3.56	3.82	1.20	0.80	1.59	1.52	1.89	1.16
Bugrino	0.95	1.08	0.22	2.18	0.95	0.99	1.34	-1.22	1.81	1.05	0.75	1.53	1.48	1.73	1.15
Cape Menshikova	1.00	0.36	0.19	0.45	0.99	0.99	1.13	-0.98	1.39	1.01	0.73	1.58	1.56	1.87	0.97
Dalne Zelenetskaya	0.92	2.19	-0.20	3.18	0.86	0.97	1.51	-0.61	2.03	0.85	0.77	2.99	2.94	3.32	1.23
Edgeøya	0.92	1.17	-0.16	3.14	0.88	0.97	2.18	-2.00	2.66	1.11	0.79	1.16	0.85	1.38	0.83
Golitsino	0.91	1.96	-0.15	3.57	0.84	0.96	2.13	-1.47	2.88	0.94	0.56	3.71	3.69	3.93	1.69
Hopen Island	0.99	0.41	0.27	0.75	1.00	0.99	0.84	-0.62	1.05	1.00	0.68	3.50	3.50	3.76	1.50
Kanin Nos	0.99	0.75	0.48	1.15	0.98	0.99	0.82	-0.68	1.09	1.05	0.78	0.83	0.66	1.10	1.06
Kolguyev Island	0.92	1.91	1.04	3.11	0.90	0.98	2.57	-2.45	3.04	1.14	0.70	0.90	0.58	1.19	0.86
Kongsøya	1.00	0.36	0.33	0.45	0.99	0.99	0.75	-0.54	1.11	1.06	0.92	1.27	1.27	1.44	1.20
Malye Karmakuly	1.00	0.51	0.38	0.68	0.99	1.00	2.04	-2.03	2.25	1.08	0.90	1.47	1.39	1.82	1.31
Mehamn	0.97	1.06	0.39	1.72	0.97	0.99	3.09	-3.07	3.24	1.12	0.82	1.96	1.96	2.18	1.13
Mys Zhelaniya	0.98	1.01	0.76	1.58	0.99	0.99	1.44	-1.27	1.80	1.04	0.79	0.96	0.77	1.35	0.93
Russkaya Gavan	0.99	0.83	0.71	1.22	0.97	0.99	4.11	-4.10	4.30	1.03	0.81	3.75	3.75	3.98	1.25
Slettnes Fyr	0.98	0.81	0.58	1.46	0.97	0.99	2.25	-2.19	2.53	1.20	0.70	1.23	1.06	1.71	1.02
Teriberka	0.99	0.71	-0.02	1.20	0.97	0.99	2.97	-2.95	3.29	1.16	0.83	0.91	0.69	1.23	1.16
Tsyp Navolok	0.84	2.45	0.37	4.46	0.85	0.96	1.22	-0.00	1.92	0.82	0.82	2.52	2.45	2.74	1.04
Vaida Guba Bay	0.97	0.93	-0.29	1.72	1.00	0.98	1.54	-1.29	1.91	1.10	0.86	1.33	1.29	1.55	1.05

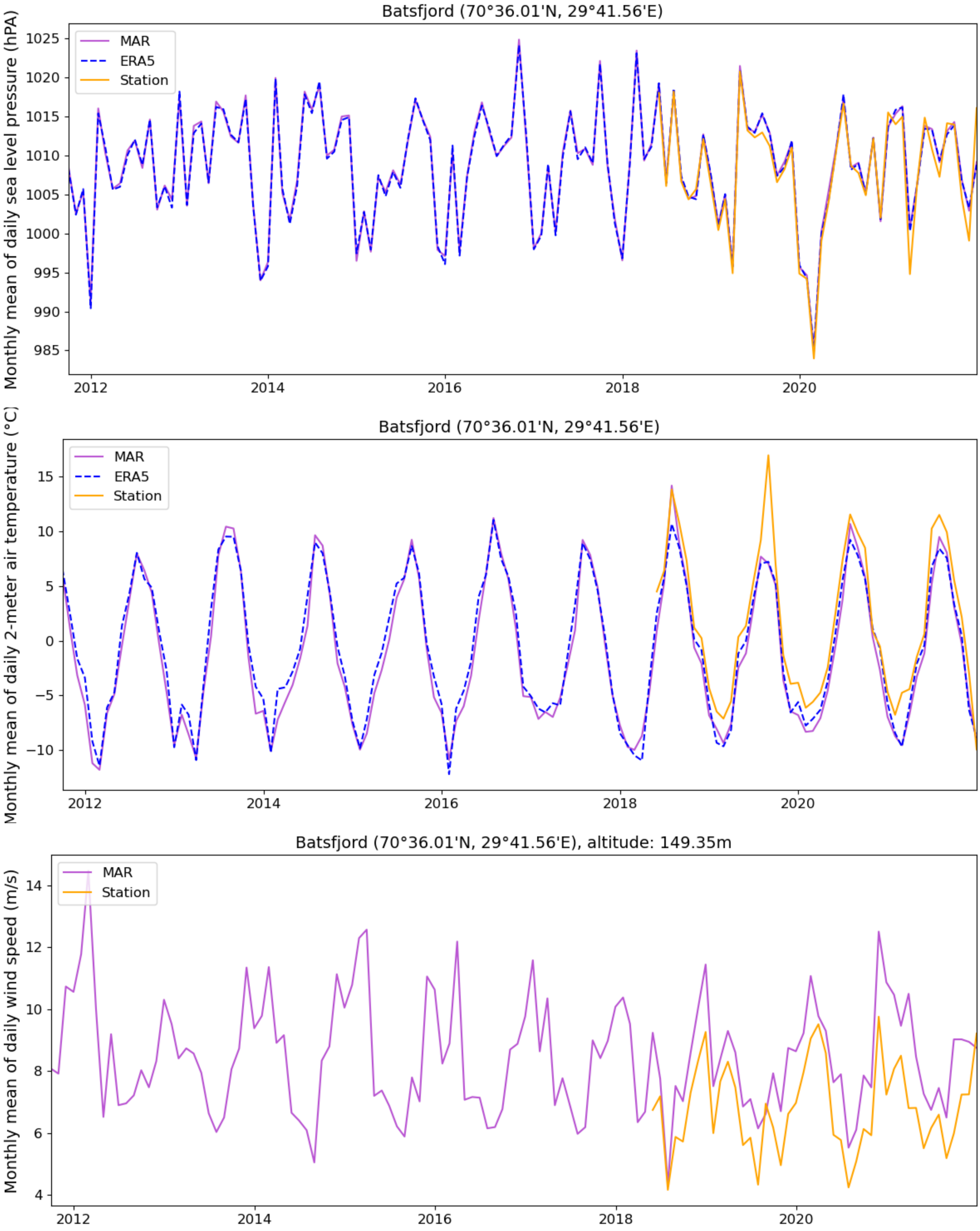

Figure 17: Validation plot: Batsfjord

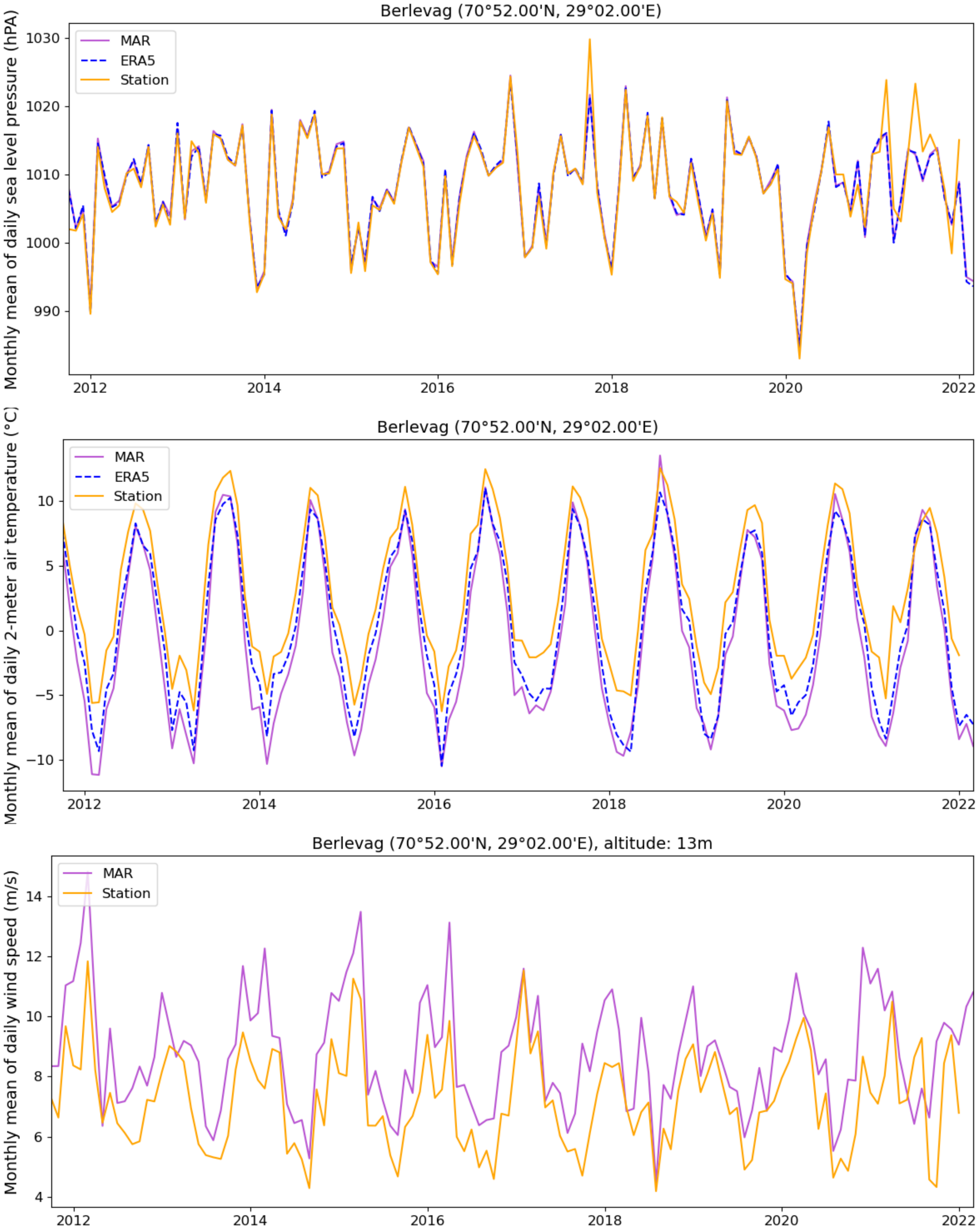

Figure 18: Validation plot: Berlevag

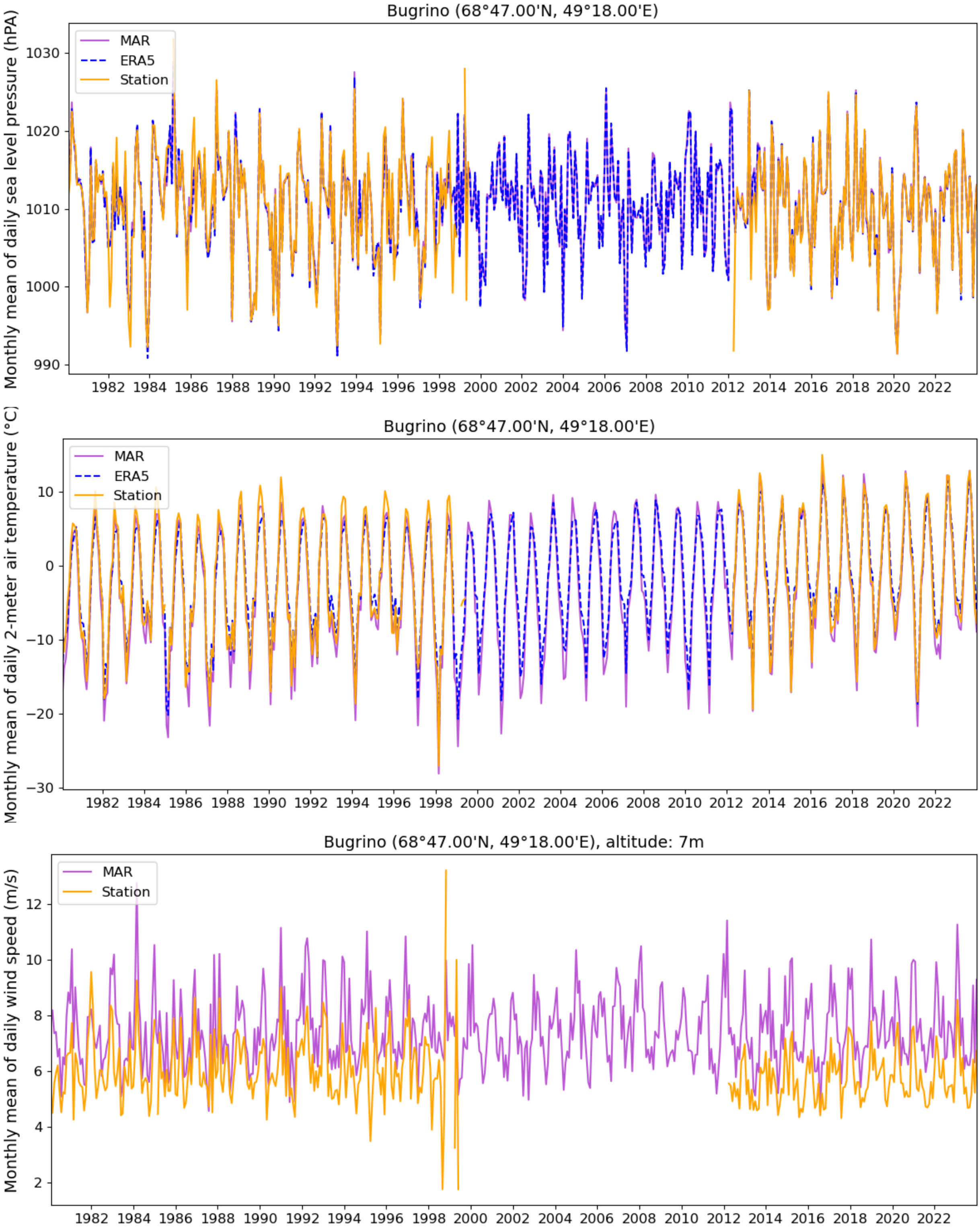

Figure 19: Validation plot: Bugrino

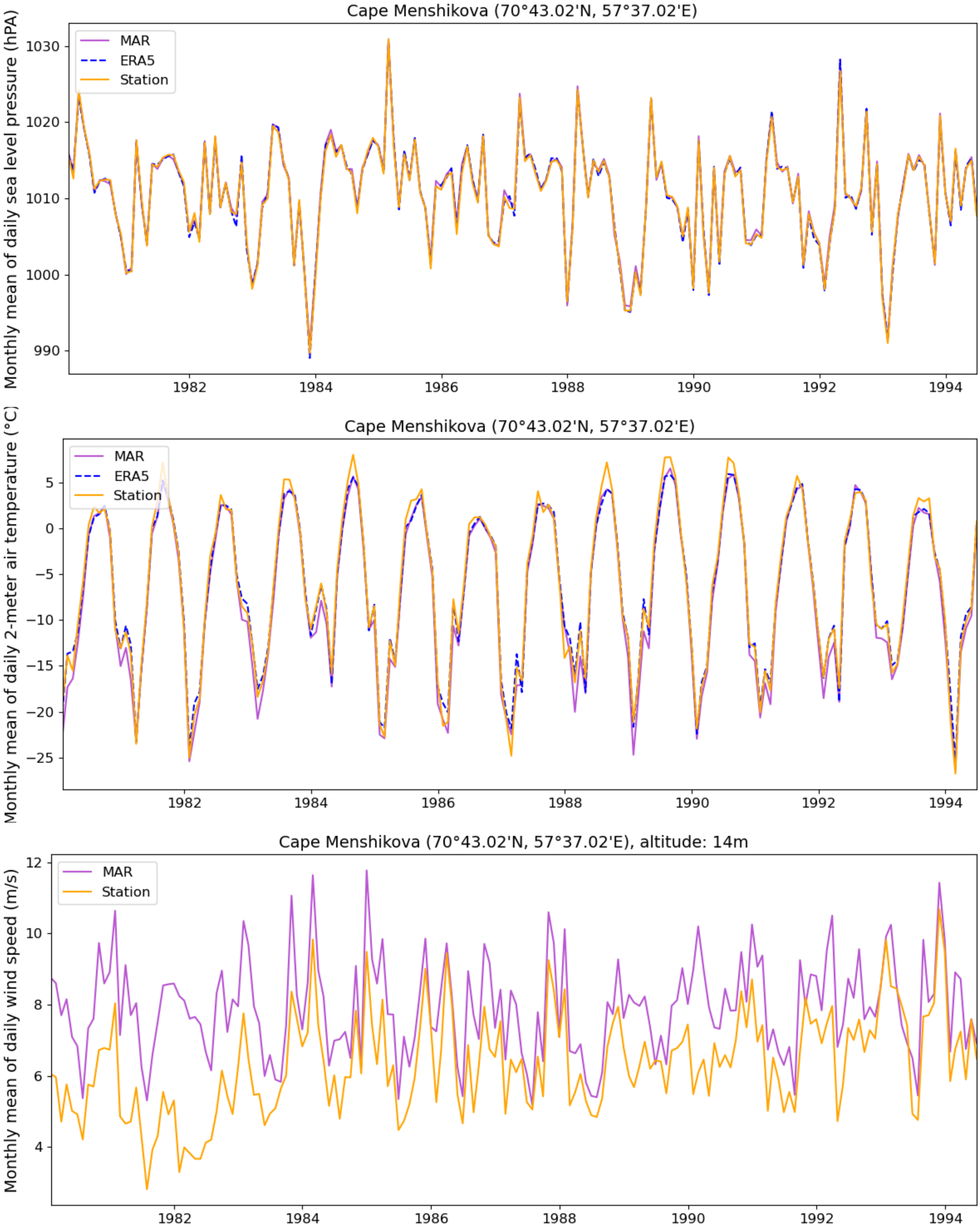

Figure 20: Validation plot: Cape Menshikova

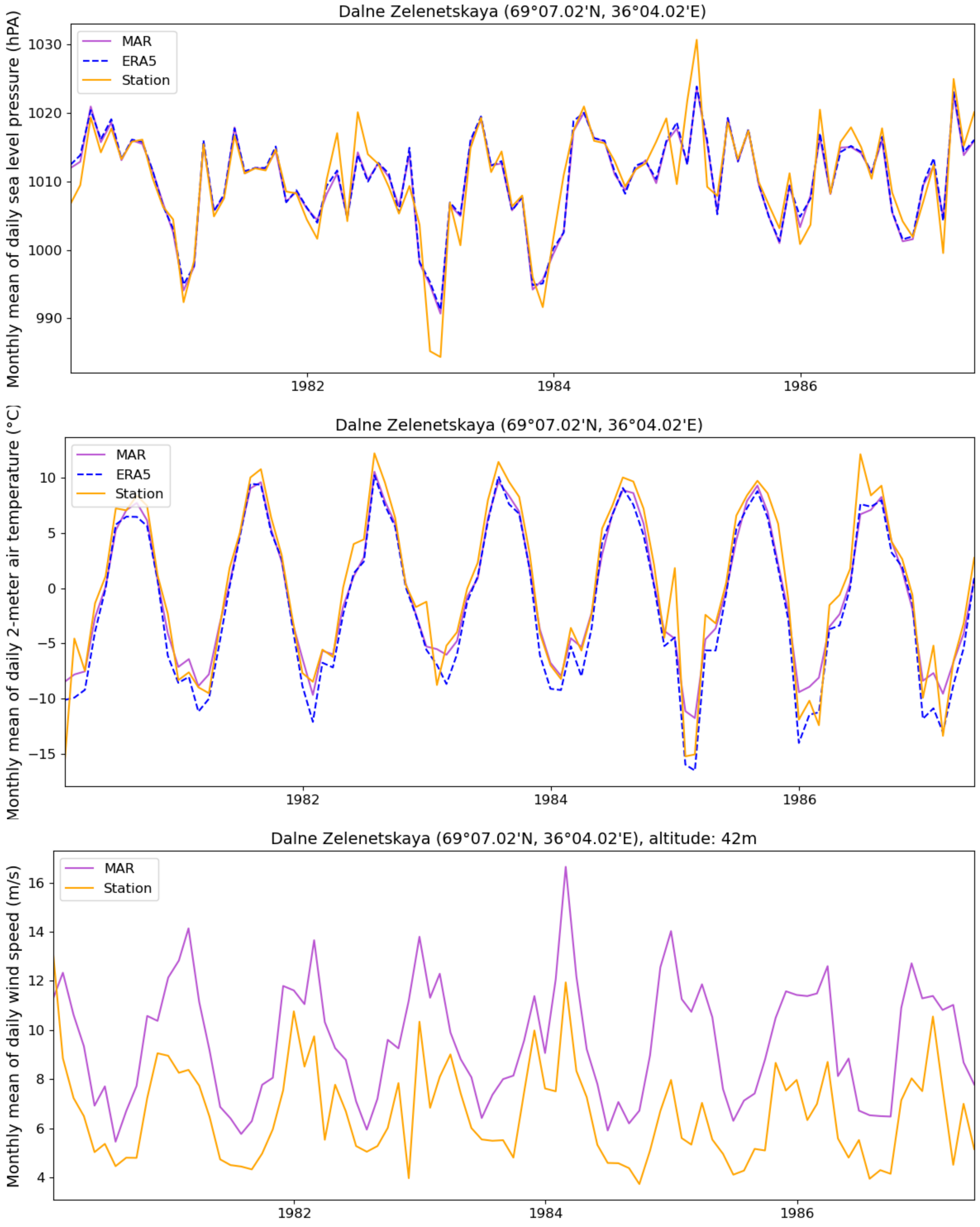

Figure 21: Validation plot: Dalne Zelenetskaya

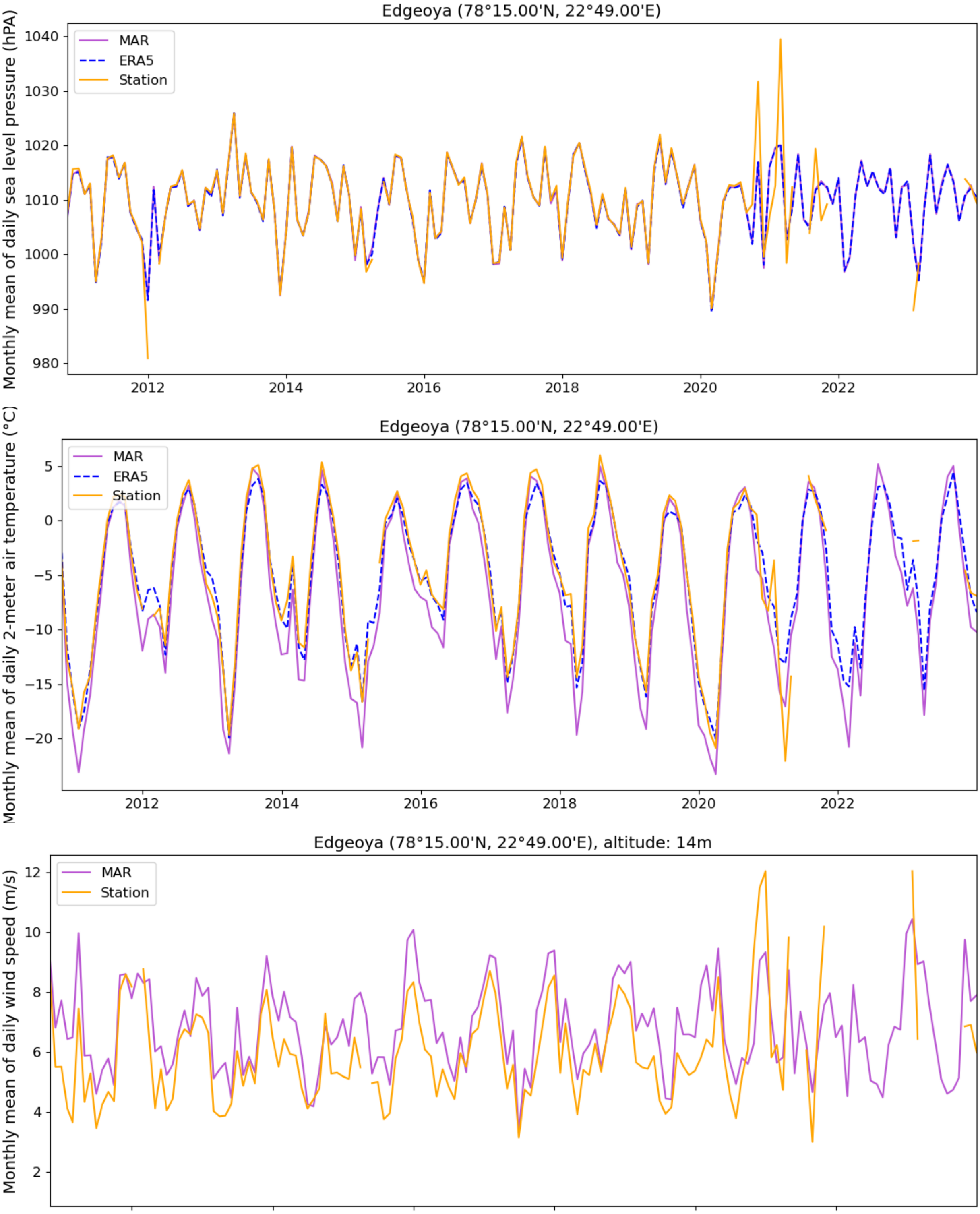

Figure 22: Validation plot: Edgeøya

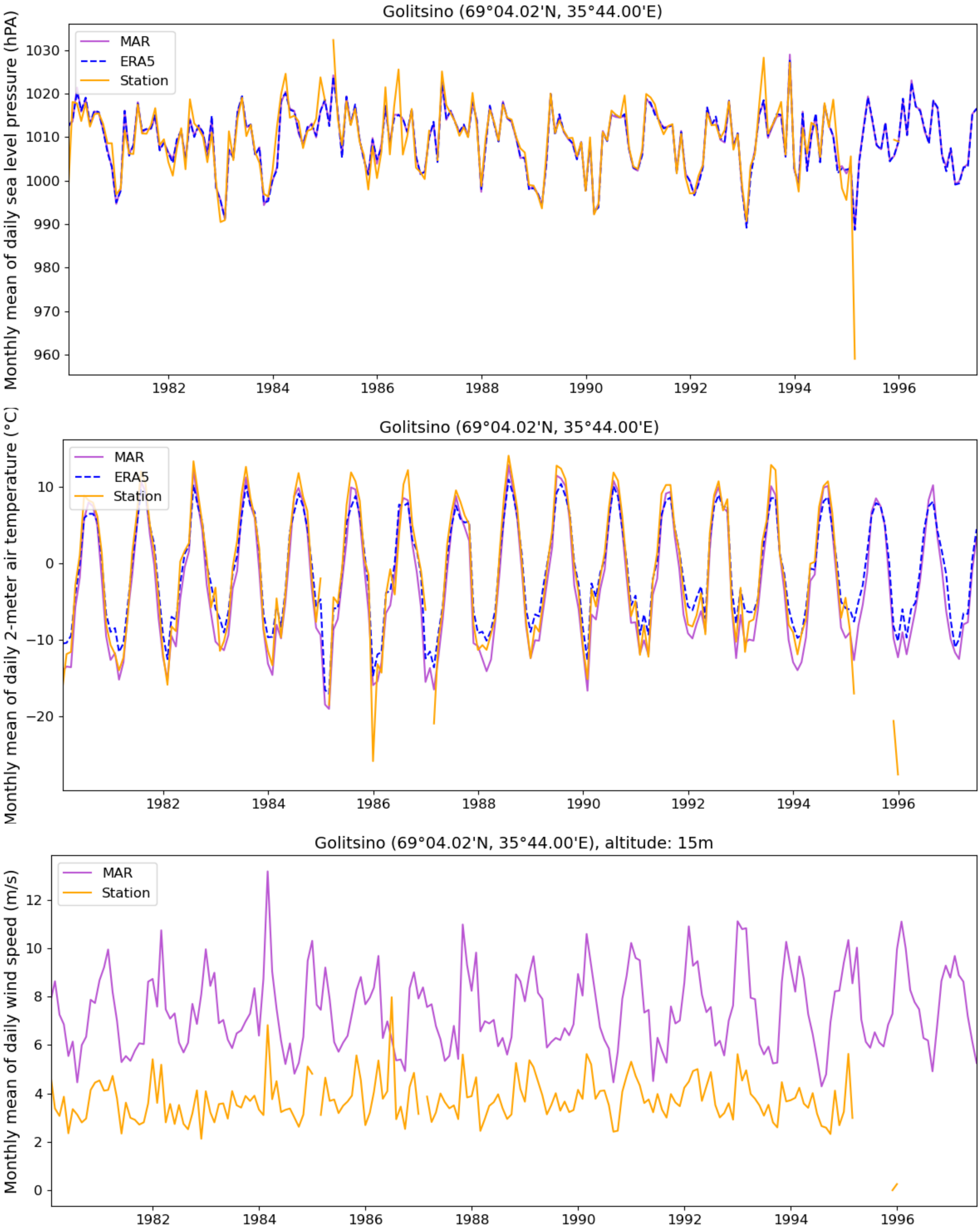

Figure 23: Validation plot: Golitsino

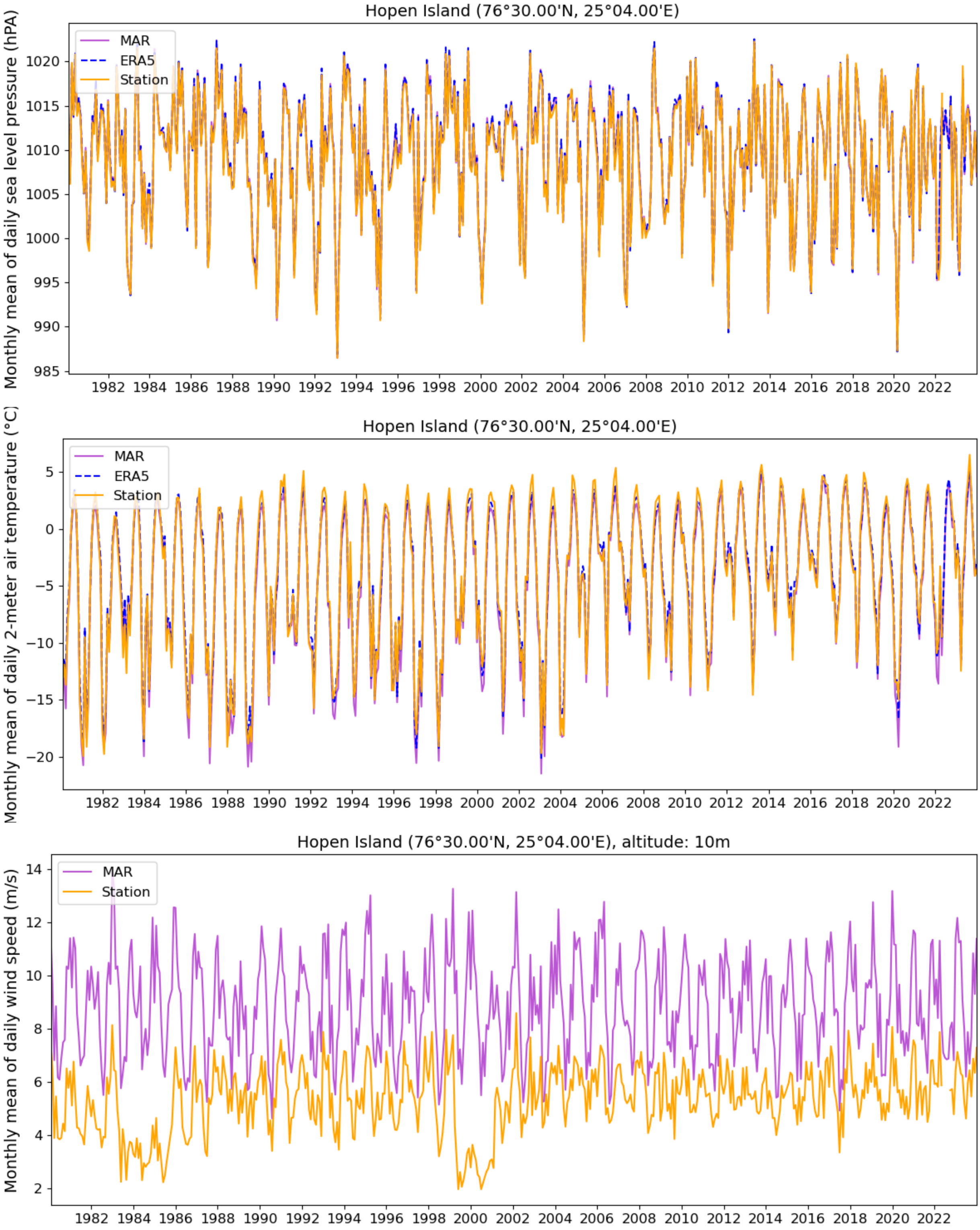

Figure 24: Validation plot: Hopen Island

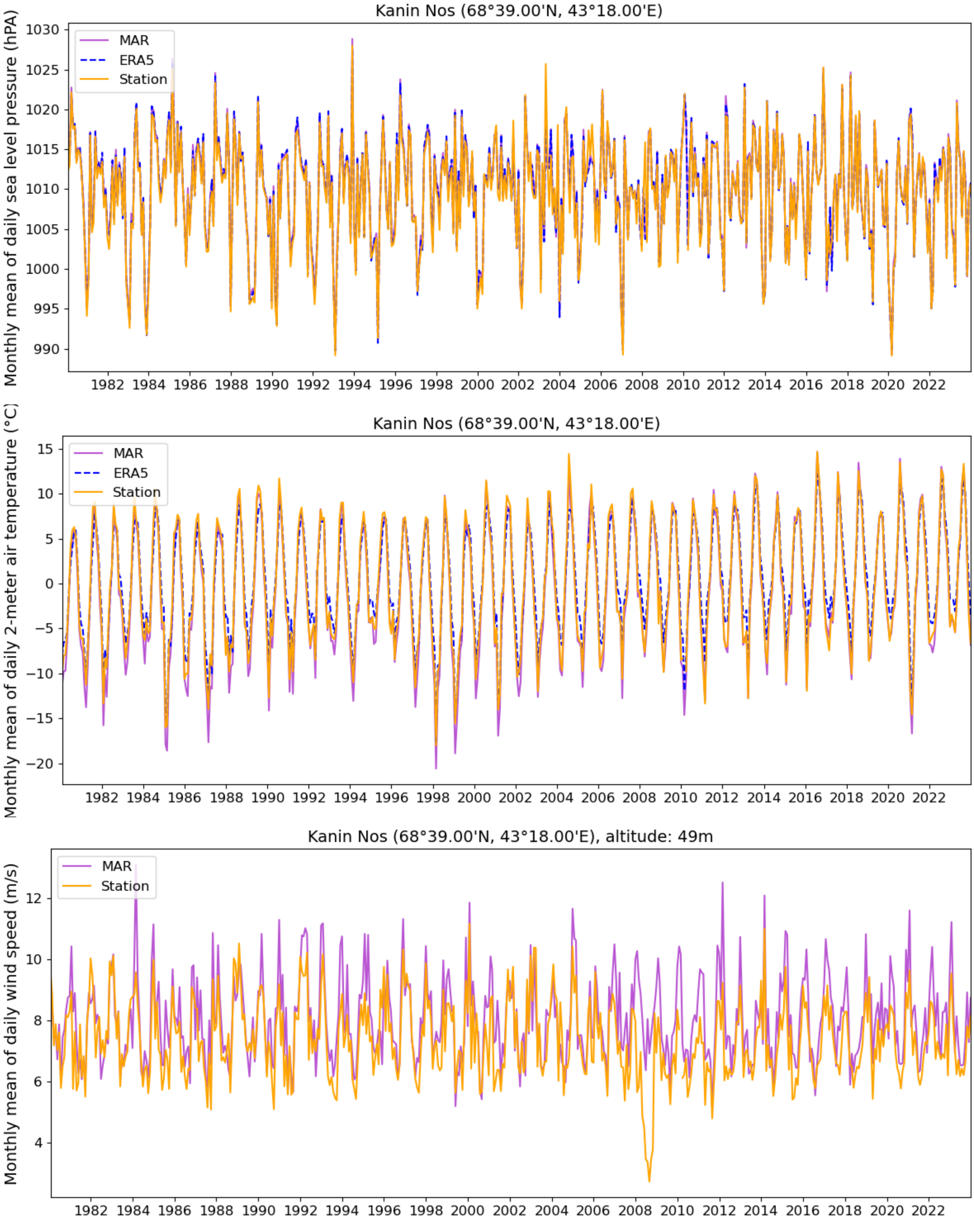

Figure 25: Validation plot: Kanin Nos

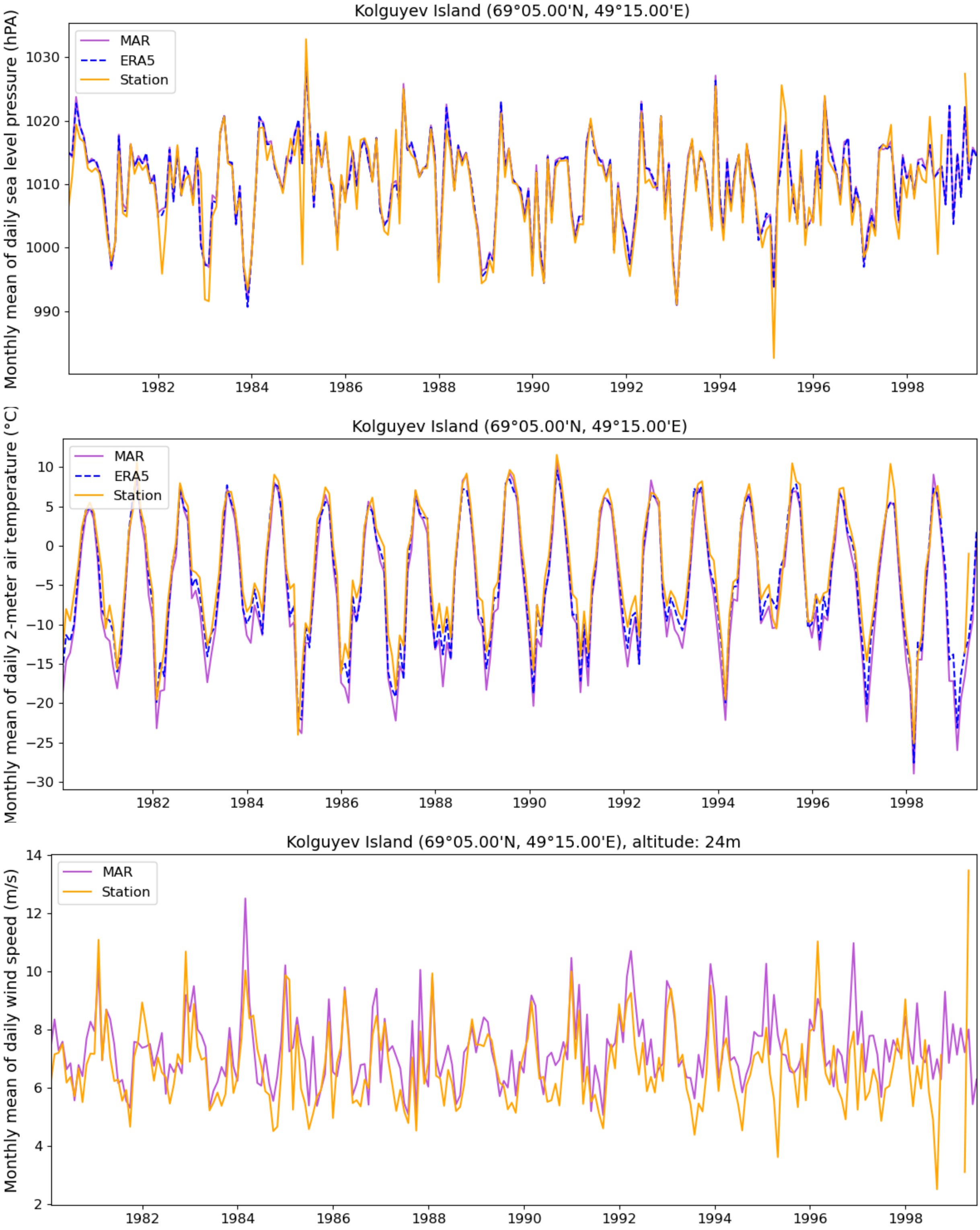

Figure 26: Validation plot: Kolguyev Island

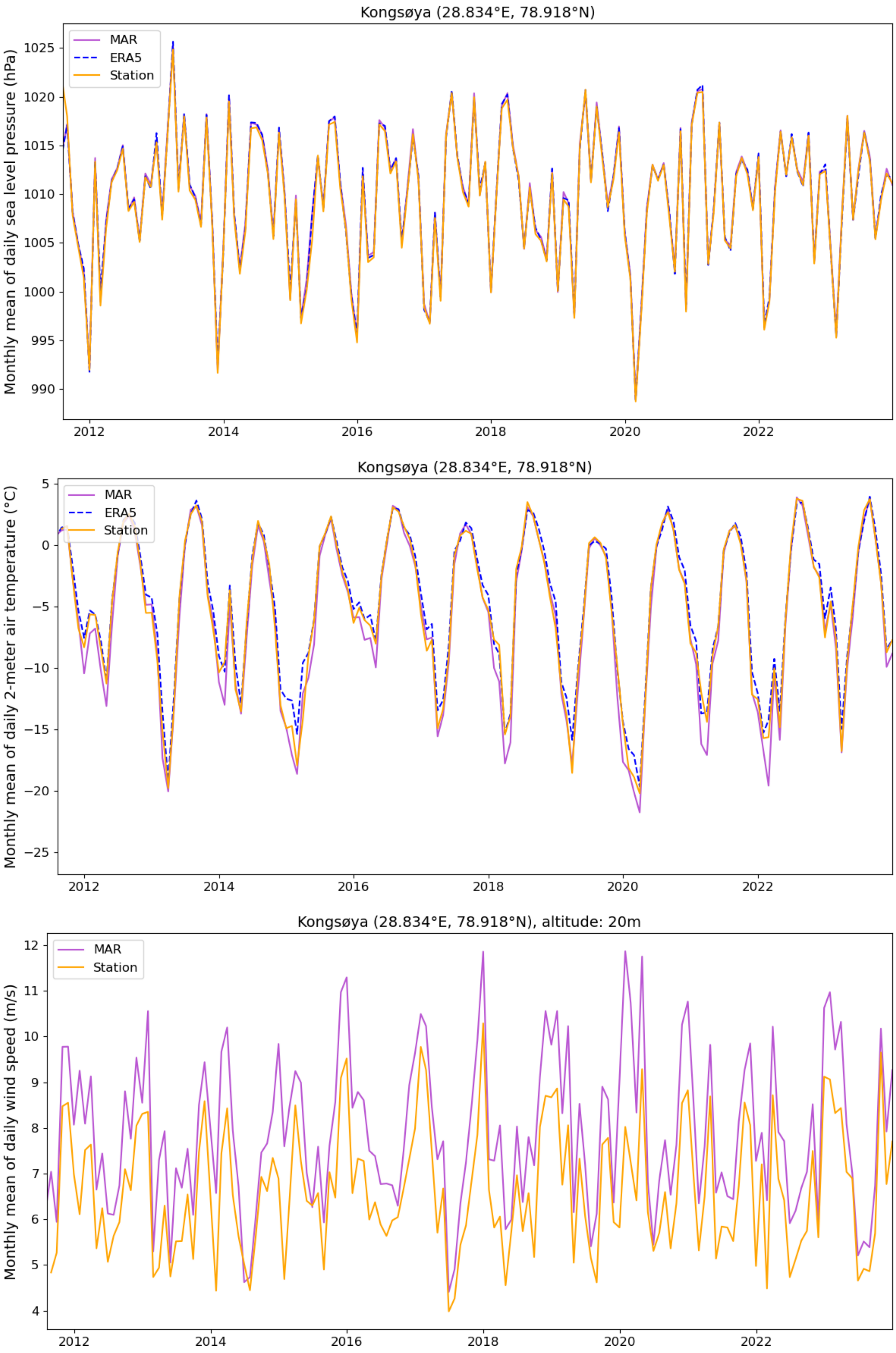

Figure 27: Validation plot: Kongsøya

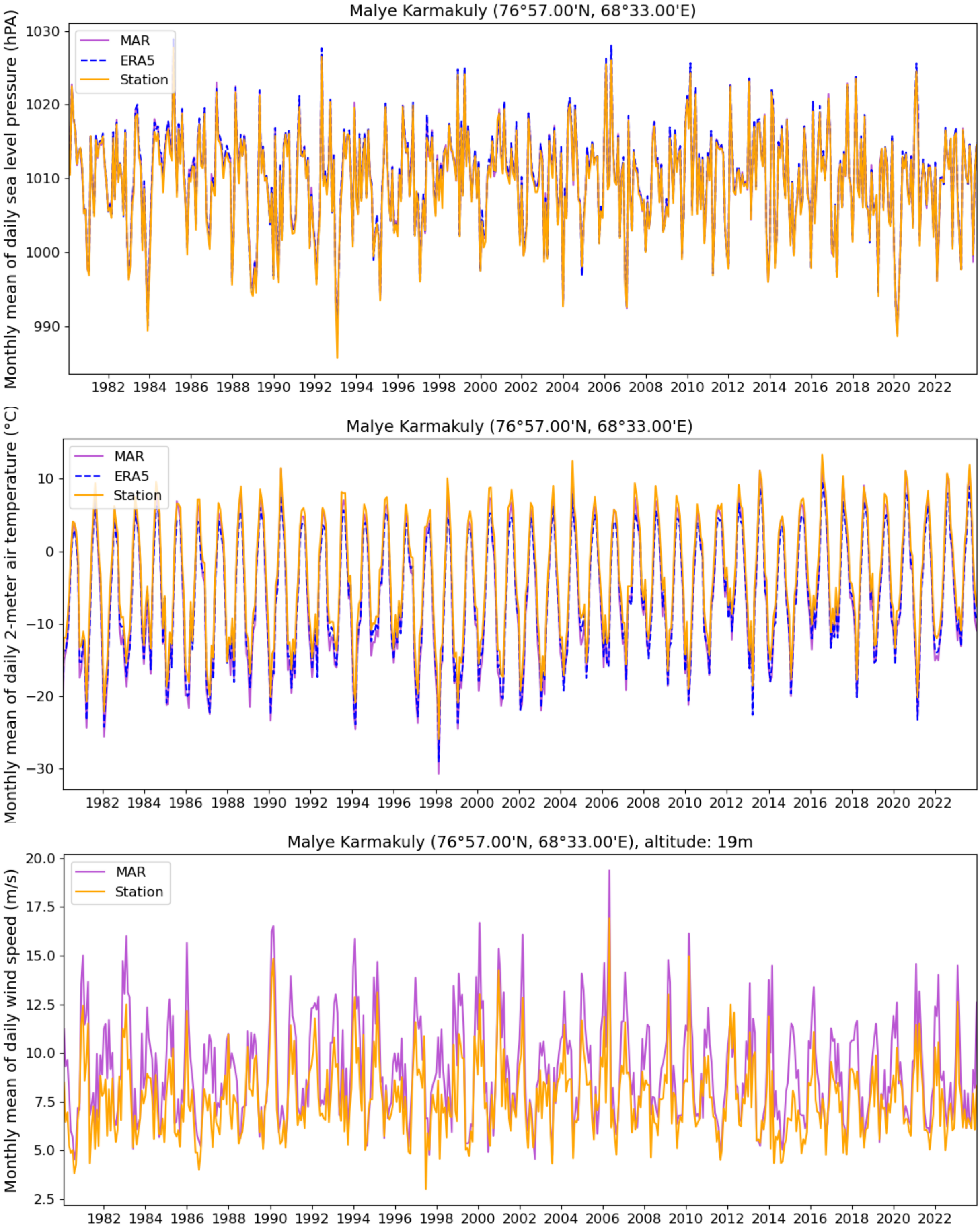

Figure 28: Validation plot: Malye Karmakuly

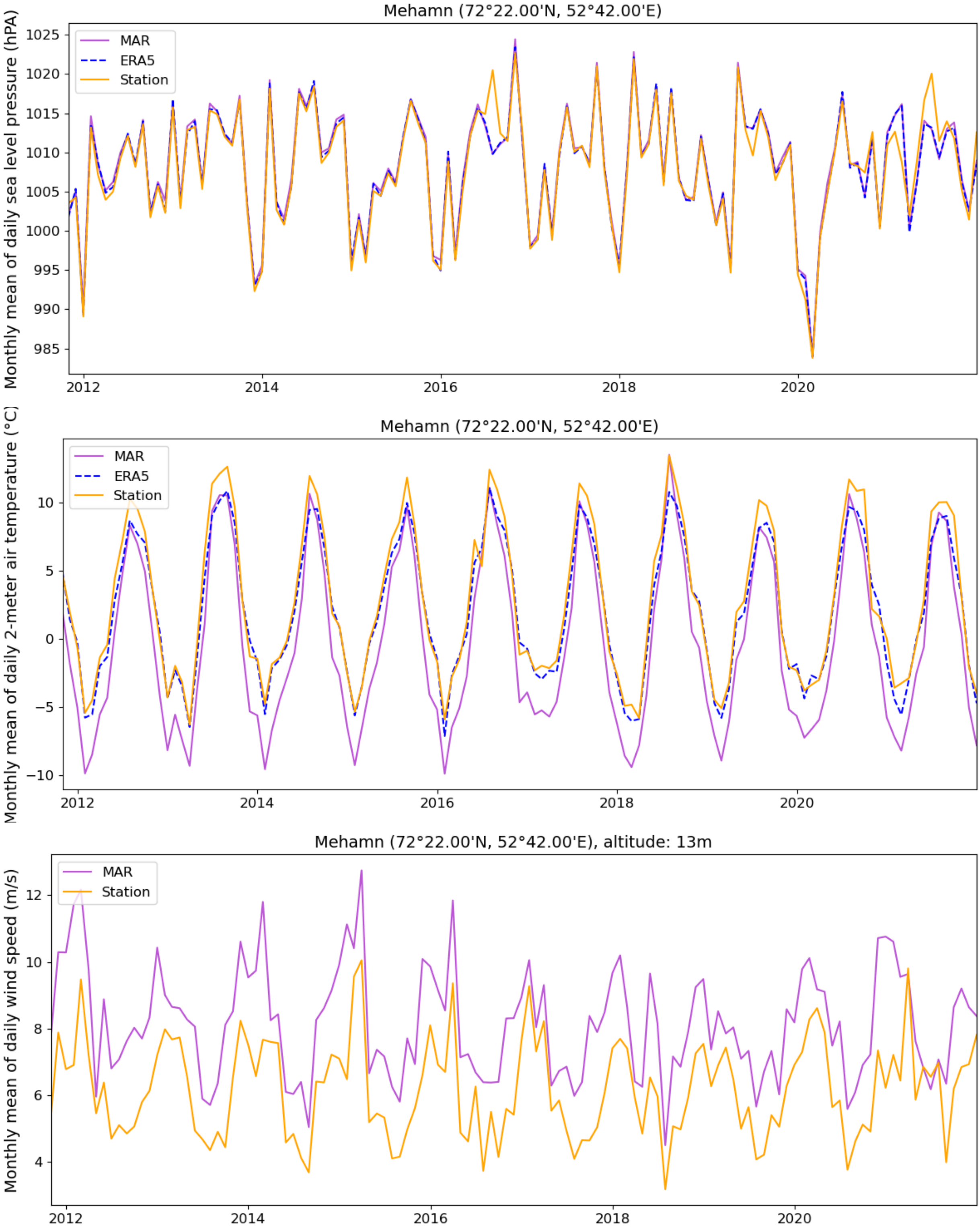

Figure 29: Validation plot: Mehamn

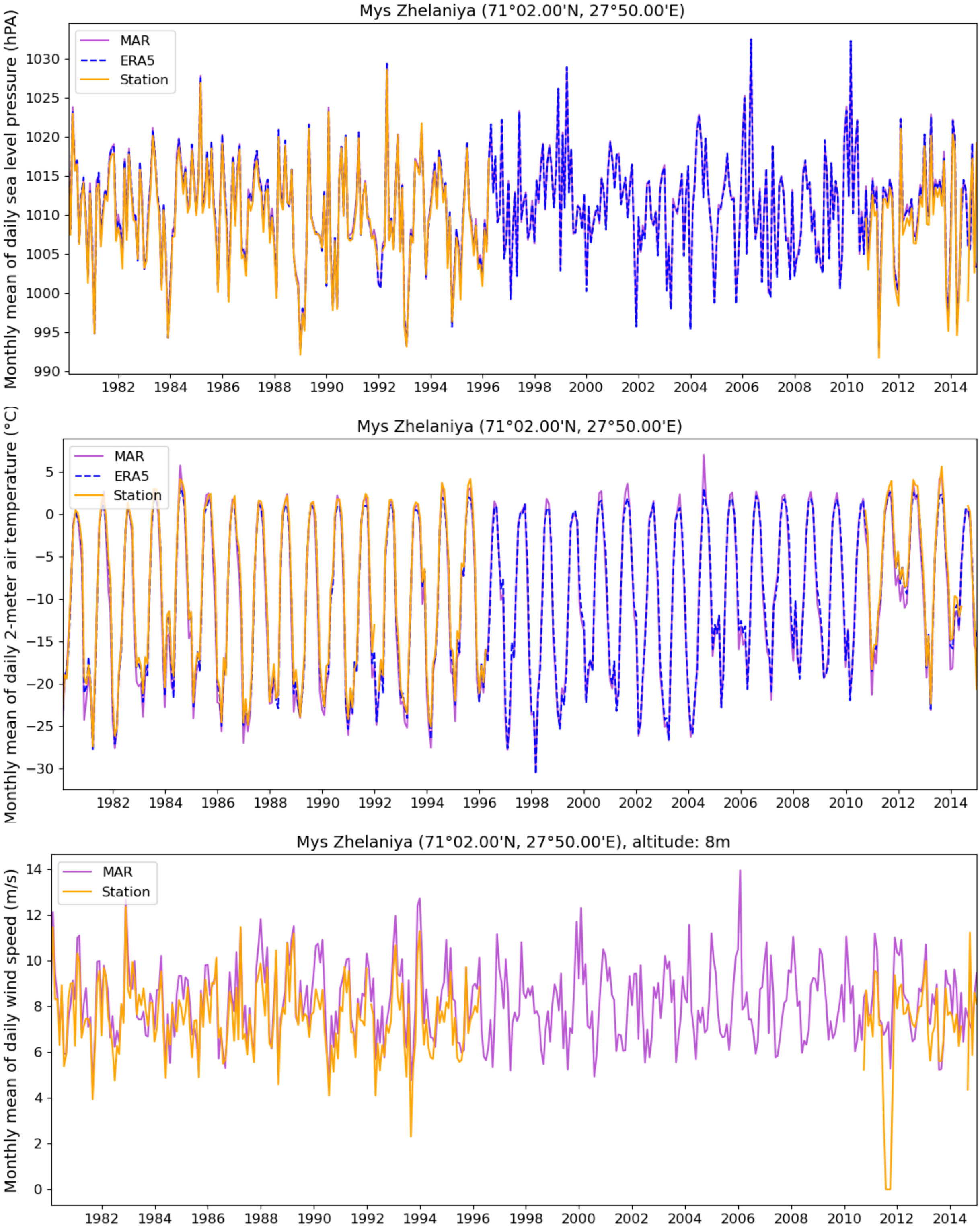

Figure 30: Validation plot: Mys Zhelaniya

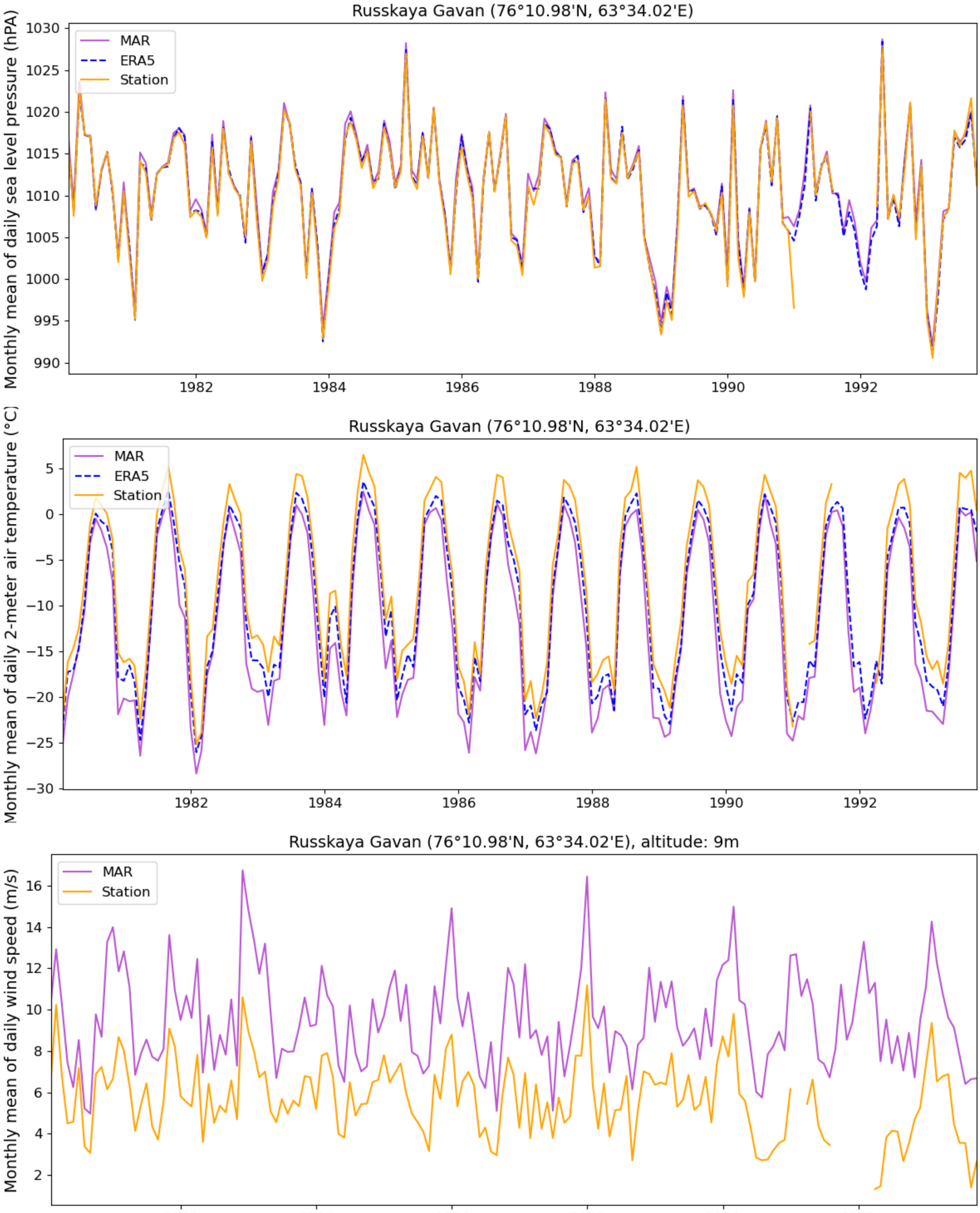

Figure 31: Validation plot: Russkaya Gavan

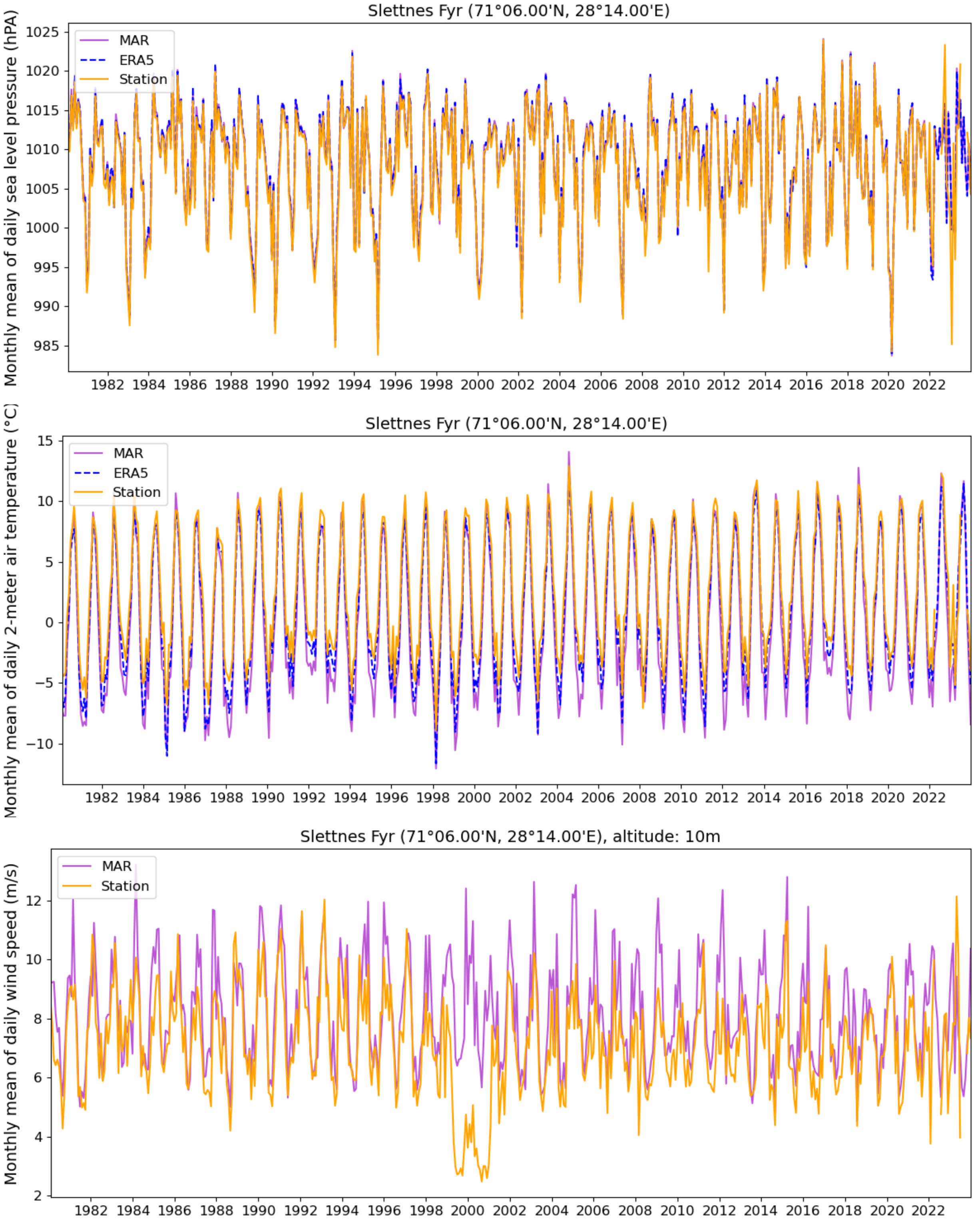

Figure 32: Validation plot: Slettnes Fyr

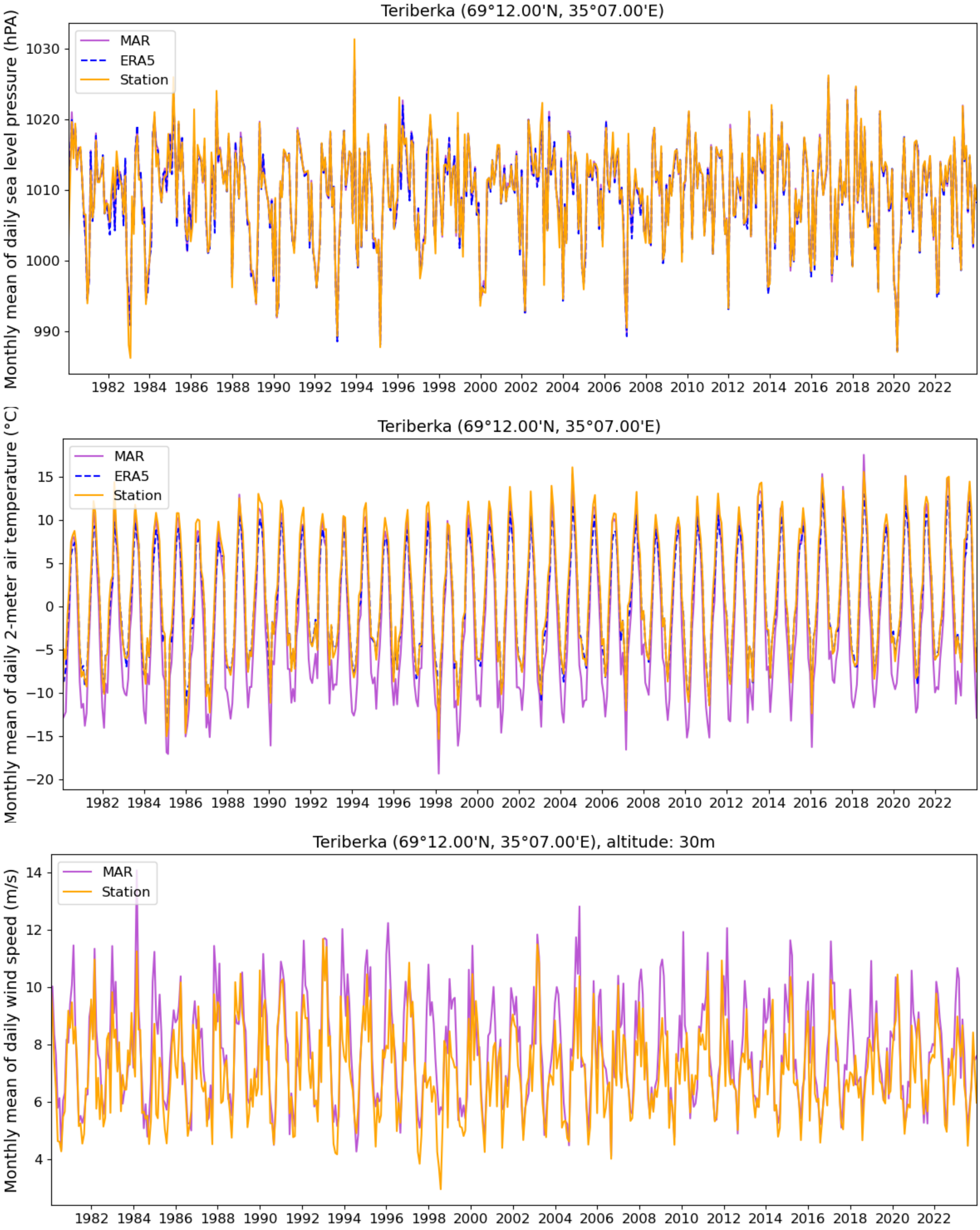

Figure 33: Validation plot: Teriberka

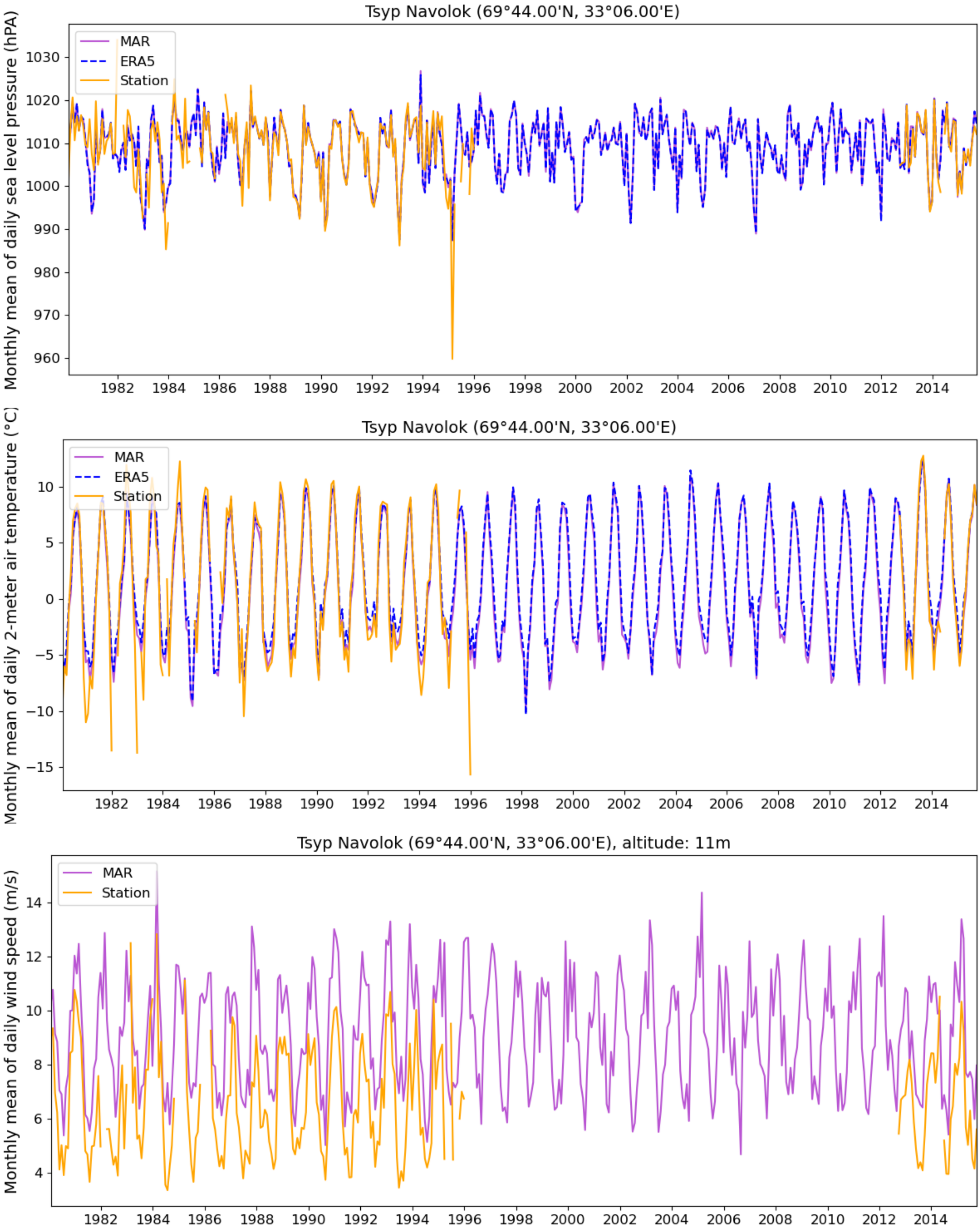

Figure 34: Validation plot: Tsyp Navolok

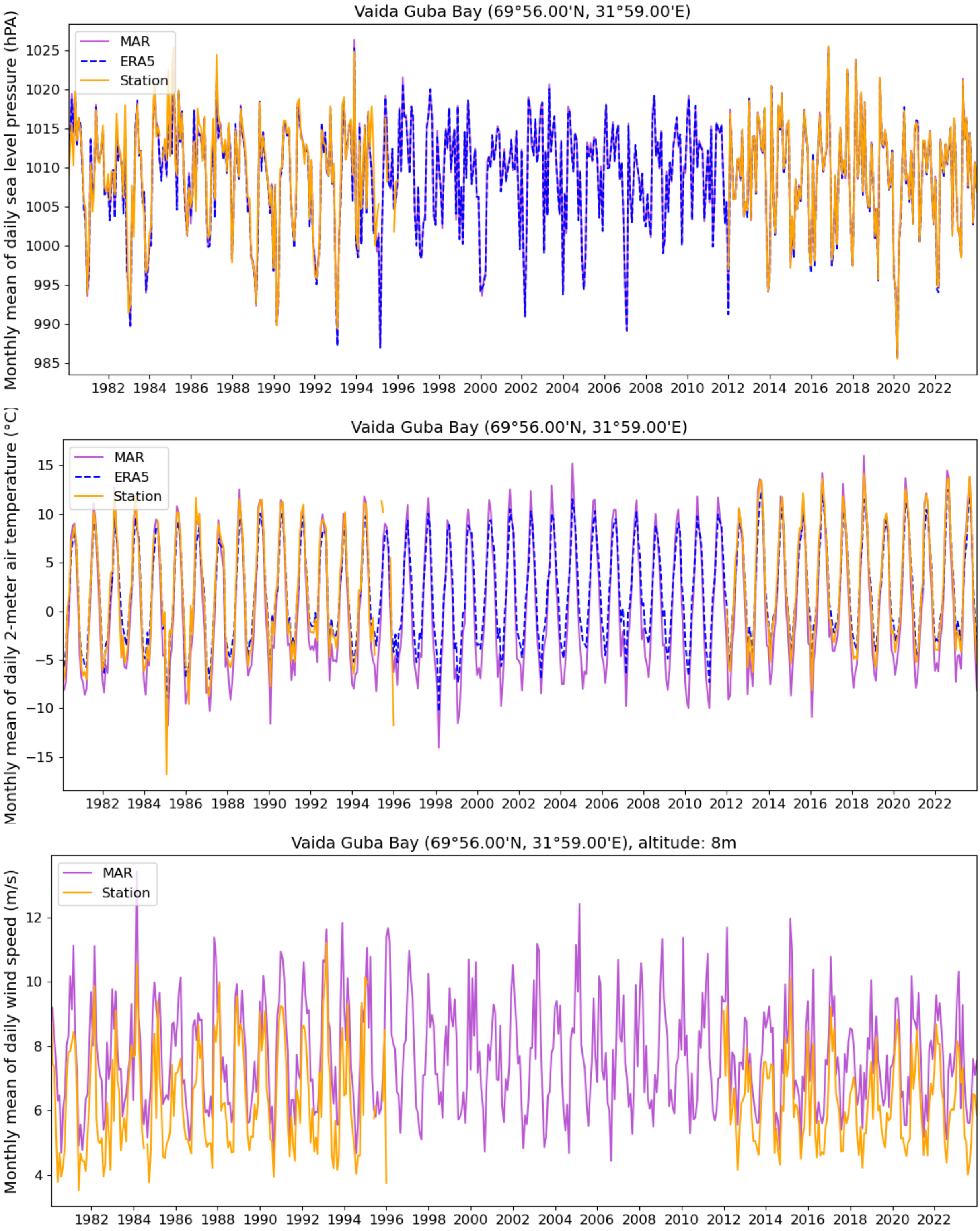

Figure 35: Validation plot: Vaida Guba Bay

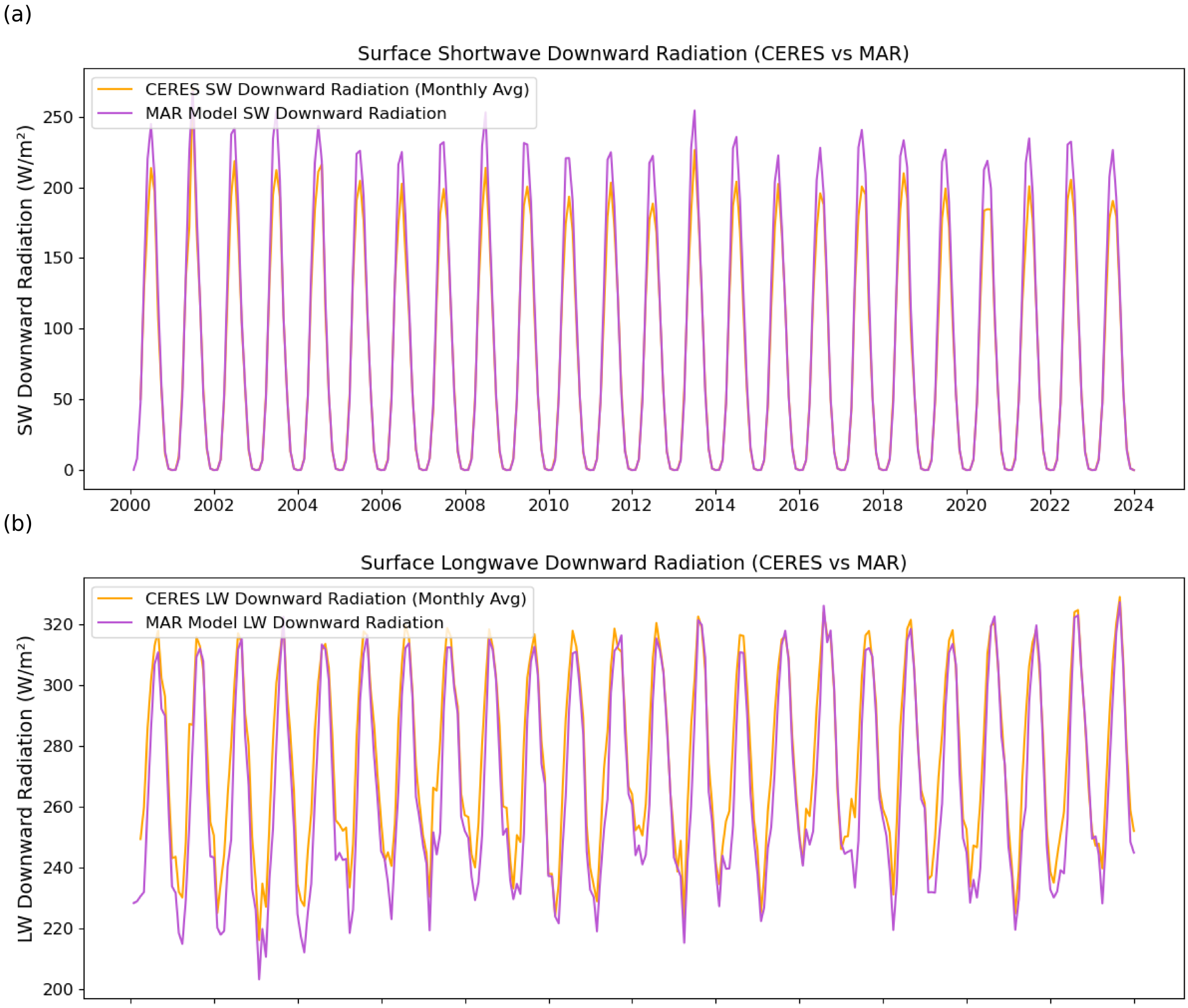

Figure 36: CERES data comparison with MAR model

A.3 JJA figures run1 and run2

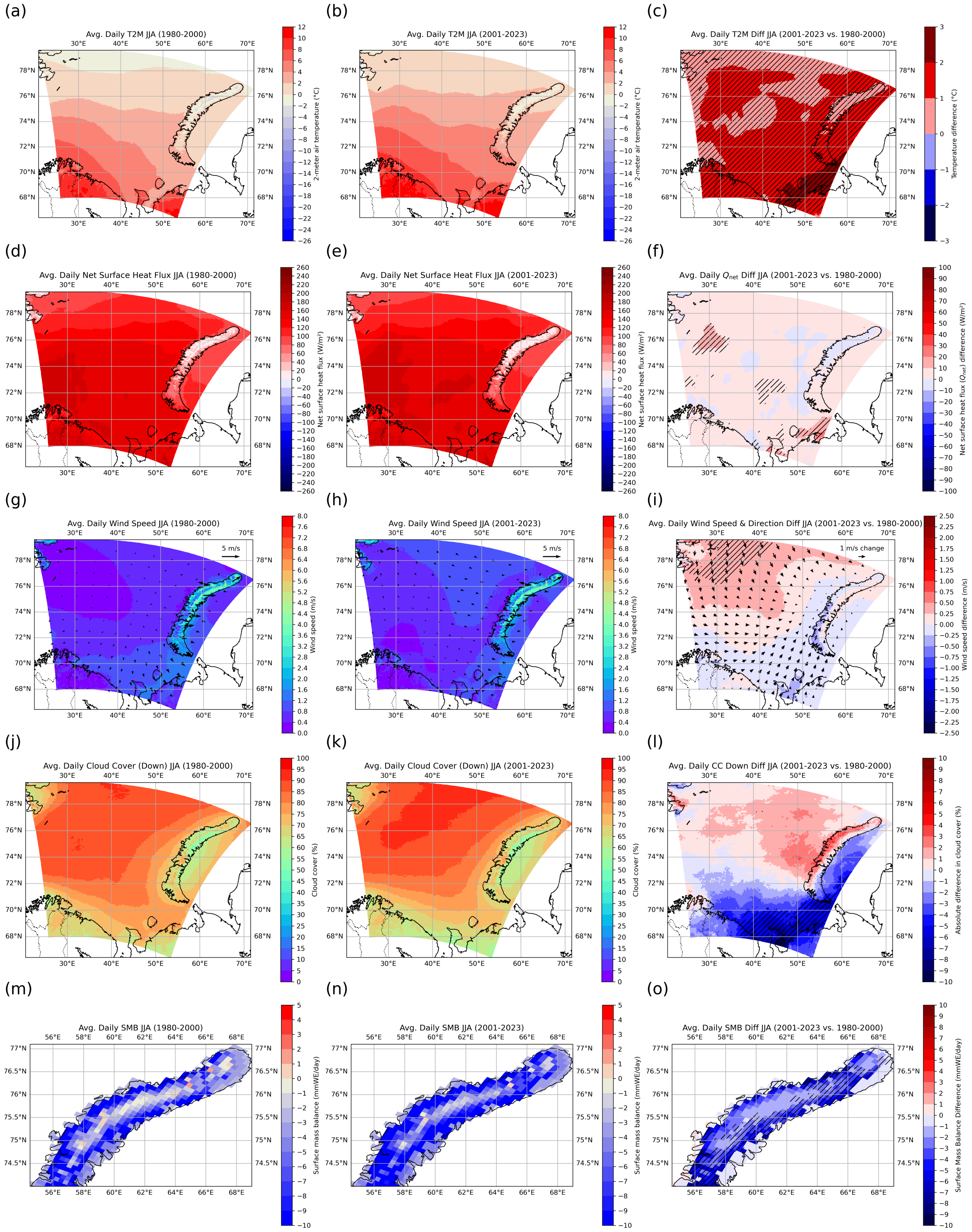
(a) Avg. Daily T2M JJA (1980-2000)

(b) Avg. Daily T2M JJA (2001-2023)

(c) Avg. Daily T2M Diff JJA (2001-2023 vs. 1980-2000)

(d) Avg. Daily Net Surface Heat Flux JJA (1980-2000)

(e) Avg. Daily Net Surface Heat Flux JJA (2001-2023)

(f) Avg. Daily Q_{net} Diff JJA (2001-2023 vs. 1980-2000)

(g) Avg. Daily Wind Speed JJA (1980-2000)

(h) Avg. Daily Wind Speed JJA (2001-2023)

(i) Avg. Daily Wind Speed & Direction Diff JJA (2001-2023 vs. 1980-2000)

(j) Avg. Daily Cloud Cover (Down) JJA (1980-2000)

(k) Avg. Daily Cloud Cover (Down) JJA (2001-2023)

(l) Avg. Daily CC Down Diff JJA (2001-2023 vs. 1980-2000)

(m) Avg. Daily SMB JJA (1980-2000)

(n) Avg. Daily SMB JJA (2001-2023)

(o) Avg. Daily SMB Diff JJA (2001-2023 vs. 1980-2000)

Figure 37: JJA run1 plots for 1980-2000 (left panels: a, d, g, j, m), 2001-2023 (middle panels: b, e, h, k, n) and 2001-2023 vs. 1980-2000 (right panels: c, f, i, l, o) for 2-meter air temperatures (a, b, c), net surface heat flux (d, e, f), wind speed (g, h, i), low cloud cover (j, k, l) and surface mass balance (m, n, o).

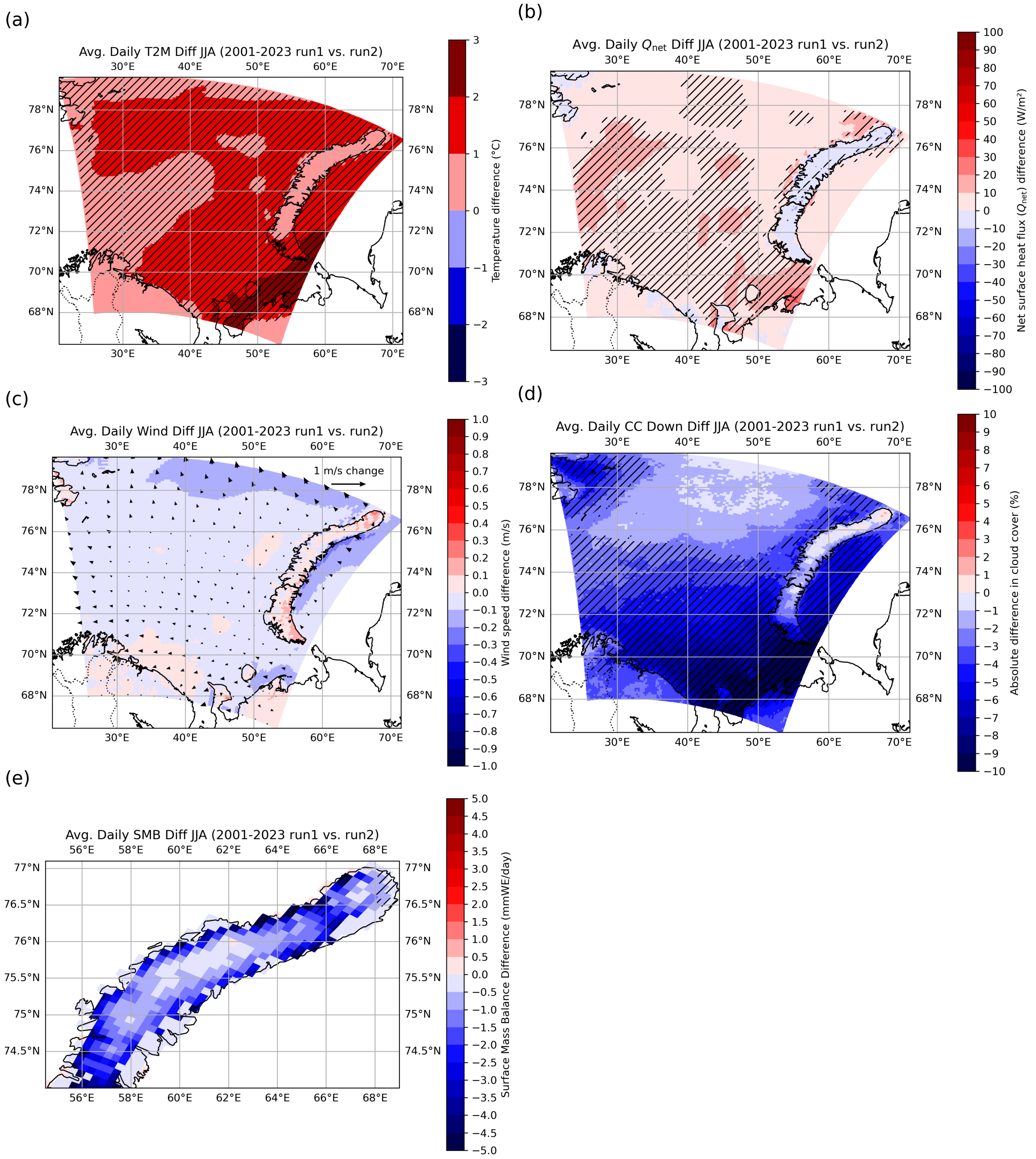

Figure 38: JJA run2 plots for 2001-2023 for 2-meter air temperatures (a), net surface heat flux (b), wind speed (c), low cloud cover (d) and surface mass balance (e).

A.4 Sea ice thickness and sea ice drift in DJF months

The dataset `GLOBAL_MULTIYEAR_PHY_001_030` from E.U. Copernicus Marine Service Information, 2023 was used to visualize SIT and sea ice drift in Figure 39. This dataset has a spatial resolution of 0.083° × 0.083° and covers the period from 1993 to 2021. To ensure consistency with our period division before and after the shift in sea ice decline, we distinguish between the periods 1993–2001 and 2002–2021. SIT has always shown strong spatial variability across the Barents Sea, with the thickest ice typically found along the northern coastline of Novaya Zemlya and in the southeastern part of the region. Before 2001, maximum SIT values in the Barents Sea reached approximately 90–100 cm. However, between 2002 and 2021, these maxima decreased, with average peak values falling below 70 cm. The greatest differences between these periods are in the Northern Barents Sea and the Kara Sea coast near Novaya Zemlya, with SIT decreases exceeding 40 cm.

In addition to changes in SIT, the DJF sea ice cover also reveals a clear drift pattern over the available period. In the northeastern Barents Sea, both the east-west (usi) and north-south (vsi) components of sea ice drift are positive, indicating a general northeastward drift. Further south along the coastline of Novaya Zemlya, the ice continues to drift northward (positive vsi values) but the predominant zonal movement shifts westward (negative usi values).

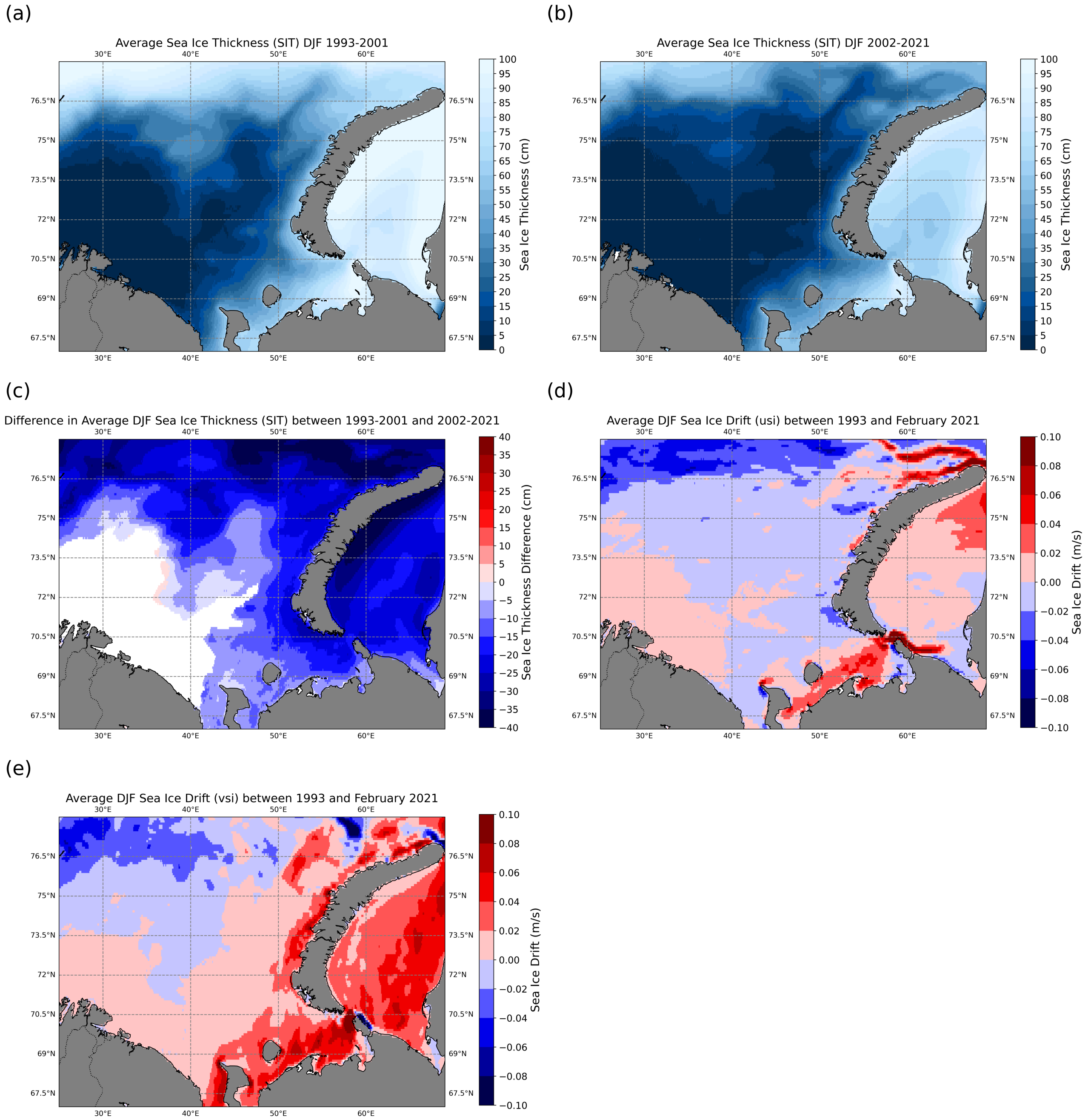

(a) Average Sea Ice Thickness (SIT) DJF 1993-2001

(b) Average Sea Ice Thickness (SIT) DJF 2002-2021

(c) Difference in Average DJF Sea Ice Thickness (SIT) between 1993-2001 and 2002-2021

(d) Average DJF Sea Ice Drift (usi) between 1993 and February 2021

(e) Average DJF Sea Ice Drift (vsi) between 1993 and February 2021

Figure 39: DJF SIT (cm) for 1993–2001 (a) and 2002–2021 (b), the difference between these two periods (c), and the average east-west (d) and north-south (e) sea ice drift (m/s) for 1993–2021.